Nina Kainbacher, BSc

A comparative density functional theory study of the intrinsic electronic structure and interfacial charge-transfer properties of pi-conjugated molecules

MASTER'S THESIS

to achieve the university degree of
Master of Science
Master's degree programme: Physics

submitted to

Graz University of Technology

Supervisor

Assoz. Prof. Dipl.-Ing. Dr. Peter Puschnig
Institute of Physics, University of Graz

Graz, August 2023

Abstract

The accurate theoretical description of organic-metal interfaces poses several challenges to density functional calculations. In three separate projects centered on electronic structure properties, we employ and compare various density functionals and dispersion correction schemes. First, we conduct a comparative study on transition metal phthalocyanine and porphine in the gas phase, which exhibit both, delocalized ligand states and strongly localized *d*-states of the central transition metal for which we examine Mn, Fe, Cu, Ni, Co and Zn. Our systematic comparison of accurate but expensive hybrid functional calculations with the cheaper GGA+U approach is aiming at the optimal effective U parameter. We find that GGA+U accurately describes non-magnetic systems but its applicability becomes more challenging for magnetic ones. This shows that a detailed study of individual transition metal complexes should always be conducted.

The second project is motivated by the on-surface synthesis of a well-ordered monolayer of the organic molecule peritetracene (peri4A) on Cu(111) from the precursor molecule 1,1'-bitetracene (bi4A). The former is of significant interest due to its potential as nanographene building block. Here, we analyze both molecules on Cu(111) in terms of their adsorption geometries and electronic structure. We find a planar adsorption geometry for peri4A, confirmed by STM images, while bi4A gets only partially planarized upon adsorption. Electronically, we observe charge transfer into the lowest unoccupied molecular orbital in both systems.

Finally, we study the effect of electric fields on the electronic structure of organic-metal interfaces exemplified for three prototypical systems. Here, charge transfer is induced by the vibrational motion of the molecule perpendicular to the substrate plane and the polarization in response to the electric field. For the former effect, we study various van der Waals functionals identifying the Tkatchenko-Scheffler and optB86b-vdW schemes as the most reliable ones. By analyzing the electric field induced charge density differences and the density of states, we show how the electric field affects charge transfer at the interface. Future angle-resolved photoemission spectroscopy experiments will put our theoretical findings to the test.

Kurzfassung

Eine genaue theoretische Beschreibung von organisch-metallischen Grenzflächen stellt die Dichtefunktionaltheorie vor mehrere Herausforderungen. In drei Projekten mit dem Fokus auf der elektronischen Struktur verwenden und vergleichen wir verschiedene Dichtefunktionale und Dispersionskorrekturen. Zunächst führen wir eine vergleichende Studie zu den Übergangsmetall-Phthalocyaninen und Porphinen in der Gasphase durch. Diese Moleküle weisen sowohl delokalisierte Ligandenzustände als auch stark lokalisierte d-Zustände im zentralen Übergangsmetall, für das wir Mn, Fe, Cu, Ni, Co und Zn heranziehen, auf. Unser systematischer Vergleich der genauen, aber rechenintensiven Hybridfunktional-Berechnungen mit dem numerisch günstigeren GGA+U-Ansatz konzentriert sich auf den optimalen effektiven U-Parameter. Unsere Analyse zeigt, dass GGA+U nicht-magnetische Systeme genau beschreibt, jedoch für magnetische Systeme problematisch ist. Dies unterstreicht, dass eine detaillierte Untersuchung einzelner Übergangsmetallkomplexe immer durchgeführt werden sollte.

Das zweite Projekt ist inspiriert von der Oberflächensynthese einer wohlgeordneten Monolage des organischen Moleküls Peritetracen (peri4A) auf Cu(111) aus dem Vorläufermolekül 1,1'-Bitetracen (bi4A). Ersteres hat großes Potential als Baustein für Nanographen. In dieser Arbeit analysieren wir beide Moleküle auf Cu(111) hinsichtlich ihrer Adsorptionsgeometrien und elektronischen Struktur. Wir finden eine planare Adsorptionsgeometrie für peri4A, bestätigt durch STM-Bilder, während bi4A bei der Adsorption nur teilweise planarisiert wird. Die elektronische Struktur ist in beiden Systemen durch einen Ladungstransfer in das unterste unbesetzte Molekülorbital gekennzeichnet.

Abschließend untersuchen wir den Einfluss elektrischer Felder auf die elektronische Struktur von organisch-metallischen Grenzflächen am Beispiel dreier prototypischer Systeme. Als Reaktion auf das externe elektrische Feld wird der Ladungstransfer einerseits durch die Schwingungsbewegung des Moleküls senkrecht zur Substratebene und andererseits durch die Polarisation der Grenzfläche induziert. Für den ersteren Effekt untersuchen wir verschiedene Van-der-Waals-Funktionale und identifizieren dabei die Tkatchenko-Scheffler und die optB86b-vdW Methode als die Zuverlässigsten. Durch die Analyse der durch das elektrische Feld induzierten Ladungsdichteunterschiede und der Zustandsdichte zeigen wir, wie das elektrische Feld den Ladungstransfer an der Grenzfläche beeinflusst. Zukünftige Experimente zur winkelaufgelösten Photoemissionsspektroskopie werden unsere theoretischen Erkenntnisse auf die Probe stellen.

Acknowledgements

I would like to express my sincere gratitude to my supervisor, Peter Puschnig, for his assistance and guidance throughout this thesis. I am also very grateful for the opportunity to work on different projects, through which I found a passion for simulating materials. Moreover, I want to thank Christian Kern and Andreas Windischbacher for their help whenever I had questions. And last but certainly not least, I am thankful to my family for their support and to my friends, especially Markus Baier, Melvin Hodžić, Barbara Messner, Paul Schnabl and Christoph Schuster, as without them, university would not have been the same.

Contents

List of Figures

List of Tables

List of Acronyms and Symbols

4A	tetracene
6P	*para*-hexaphenyl
ARPES	angle-resolved photoemission spectroscopy
bi4A	1,1'-bitetracene
BJ	Becke-Johnson
DFT	density functional theory
DOS	density of states
FFT	fast Fourier transform
GGA	generalized gradient approximation
HOMO	highest occupied molecular orbital
HSE	Heyd–Scuseria–Ernzerhof
LDOS	local density of states
LEED	low-energy electron diffraction
L(S)DA	local (spin) density approximation
LUMO	lowest unoccupied molecular orbital
MOPDOS	molecular orbital projected density of states
NTCDA	1,4,5,8-naphthalene-tetracarboxylic dianhydride
NIXSW	normal incidence x-ray standing waves
OFET	organic field effect transistor
OLED	organic light emitting diode
OPV	organic photovoltaics
PBE	Perdew-Burke-Ernzerhof
PDOS	projected density of states
peri4A	peritetracene
PTCDA	perylene-3,4,9,10-tetracarboxylic dianhydride
RMM-DIIS	residual minimization scheme, direct inversion in the iterative subspace

SCF	self-consistent field
sl	semilocal
STM	scanning tunneling microscopy
TMC	transition metal complex
TMP	transition metal porphine
TMPc	transition metal phthalocyanine
TS	Tkatchenko-Scheffler
UPS	ultraviolet photoelectron spectroscopy
VASP	Vienna Ab Initio Simulation Package
vdW	van der Waals
vdW-DF	van der Waals density functional

1 Introduction

Over the past two decades, the field of organic electronics and optoelectronics has gained a lot of attention due to their potential technological applications, such as organic light emitting diodes (OLEDs), photovoltaics (OPVs), and field effect transistors (OFETs) [1]. Unsurprisingly, also the number of experimental and theoretical studies on organic-metal interfaces, as formed by adsorption of organic or metal-organic compounds on metallic substrates, has been steadily increasing [2]. Theoretically, the focus has been put on an accurate description of the electronic structure of these organic and inorganic components, since the accuracy influences bond lengths and adsorption distances and therefore, the level alignment and charge transfer at the interface [3, 4]. However, achieving high accuracy in the description of the electronic structure is a challenging task due to the variety of physical effects that need to be captured. The choice of the level of theory often involves finding a balance between accuracy and computational cost. In this thesis, electronic structure calculations are performed for different metal-organic compounds and organic-metal interfaces using the Vienna Ab Initio Simulation Package (VASP) [5–7], a widely used density functional theory (DFT) code. The study comprises three projects, each pursued with specific research objectives. Despite the diversity in project goals, a common focus lies on the analysis of the electronic structure properties by employing and comparing various methods to provide sufficient accuracy.

The thesis comprises the following three projects: The description of transition metal complexes, a specific class of metal-organic compounds, in the gas phase with an emphasis on the difference between hybrid functional calculations and GGA+U calculations; the theoretical part of a joint experimental and theoretical study on two tetracene (4A) derivatives on the Cu(111) surface and, finally, the study of organic-metal interfaces in static electric fields. Prior to these chapters, we outline the theory underlying density functional calculations and explain the electronic structure methods used throughout this thesis.

The first project, summarized in Chapter 3, discusses the two promising transition metal complexes, namely transition metal phthalocyanine (TMPc, $\mathrm{TM(C_8H_4N_2)_4}$) and porphine (TMP, $\mathrm{TM(C_{20}H_{12}N_4)}$), since these show highly interesting electronic and magnetic properties that can be exploited in various technological fields, such as optoelectronics, spintronics and quantum computing [8–10]. The description of their electronic structure within a density functional framework is complicated by the fact that these molecules exhibit highly delocalized states extending over the entire molecule as well as strongly localized states originating from the d-states of the central transition metal atom. Usually, hybrid functional calculations are performed for an accurate characterization due to the inclusion of some exact exchange in the energy functional. However, when dealing with interfaces, these calculations are computationally too expensive. Our study therefore aims to describe the *d*-orbital energies of TMPc and TMP with the same accuracy as the two hybrid functionals, HSE06 [11] and PBEh [12–14], but by using the much cheaper GGA+U approach [15]. In particular, we are interested in obtaining the optimal U_{eff} value of Dudarev's approach [16] that gives comparable results to the hybrid calculations for the corresponding transition metal complex. A similar study has already been done for TMPc for the following transition metals, Mn, Fe, Co, Ni and Cu by Brumboiu et al. [17]. This thesis, therefore, extends the scope of analysis to include ZnPc, as well as the molecule TMP to investigate, whether there are potential parallels to TMPc. To reach this goal, we are comparing three aspects: The density of states (DOS) projected onto the *d*-orbitals, the HOMO-LUMO gaps and the magnetic moments.

The second project (Chapter 4) comprises the theoretical analysis of the two tetracene derivatives, 1,1'-bitetracene (bi4A, $C_{36}H_{22}$) and peritetracene (peri4A, $C_{36}H_{18}$), on Cu(111). In the experimental work, conducted at the University of Tübingen, the precursor molecule bi4A was deposited and, subsequently, annealed on the Cu(111) substrate to form a well-ordered monolayer of peri4A via an on-surface reaction. The latter is a potential candidate as building block for zigzag-edged nanographenes which show interesting electronic and magnetic properties [18–20] and has not been analyzed in detail before. In order to investigate the electronic structure of these organic-metal interfaces and to shed light on experimental scanning tunneling miscroscopy (STM) and ultraviolet photoelectron spectroscopy (UPS) data, we have performed DFT calculations employing the repeated slab approach [21]. We utilized the generalized gradient approximation (GGA) [22] for exchange-correlation effects and DFT-D3(zero) [23] to account for van der Waals interactions. Specifically, our results include the analysis of charge rearrangements upon adsorption, work function change, charge transfer and projections of the DOS onto the molecular orbitals (MOPDOS) [24]. To additionally confirm the peri4A monolayer formation, the (STM) image was simulated using the Tersoff-Haman approximation [25, 26].

The third project, summarized in Chapter 5, can be regarded as forming the theoretical groundwork towards electric field induced charge transfer at an organic-metal interface. Experimentally, it is planned to drive charge transfer at the system's interface with strong THz pulses and observe it via angle-resolved photoemission spectroscopy (ARPES) for the first time. This charge transfer is induced, on the one hand, by the vibration of the molecule perpendicular to the substrate plane and, on the other hand, by the electronic polarization within the system due to the applied field. Therefore, in a first step, we calculate the frequency required to induce a collective vibrational motion of the two test systems, namely *para*-hexaphenyl (6P, $C_{36}H_{26}$) on Cu(110) and 6P on Ag(110). These systems are chosen to compare the effect of the substrate since copper interacts more strongly with the adsorbate compared to silver. Furthermore, we combine this study with a comparison of different local and nonlocal van der Waals functionals to analyze their performance on the adsorption distances and the frequencies.

Subsequently, for the simulation of the THz pulses, we approximate one half cycle of the waveform by a static electric field. To analyze the influence on interfaces, electric fields with field strengths ranging from -0.3 V/Å to 0.3 V/Å are applied in a direction perpendicular to the substrate plane. To the two previously mentioned test systems, we added perylene-3,4,9,10-tetracarboxylic dianhydride (PTCDA, $C_{24}H_8O_6$) on Ag(110). This choice enables us to additionally compare between a weak acceptor molecule (6P) and a strong acceptor molecule (PTCDA). The interesting question is whether the geometric changes or the purely electronic polarization influence the charge transfer at the interface more strongly. To answer this question, we first analyze how the atoms within the molecules rearrange in response to the electric field and investigate the changes in the projected DOS for the considered field strengths. Second, we observe only the electronic polarization by applying the field but fixing the geometry at the relaxed structures obtained without electric field. In particular, we analyze the projected DOS, charge transfer and electric field induced charge density difference in response to the electric field.

2 Theory

The purpose of this section is to provide an introduction to density functional theory (DFT) and the methodologies used for metal-organic interfaces. It discusses the approximations for exchange-correlation effects used within DFT (see Section 2.3), including the generalized gradient approximation (GGA) and hybrid functionals. Moreover, the plane wave basis set and the repeated slab approach used for interface modeling are explained in Section 2.4, as well as a brief summary of the structure relaxation algorithm of damped molecular dynamics. Additionally, the van der Waals correction schemes used in this thesis are explained in Section 2.4.4. These are necessary for systems, such as interfaces, where long-range dispersion forces are present.

2.1 The quantum mechanical many-electron problem

We start from the time-independent (i.e., stationary) non-relativistic Schrödinger equation for a system with N electrons at positions $\boldsymbol{r}_i$ with spin σ_i and K nuclei at positions $\boldsymbol{R}_k$ with charge numbers Z_k and masses M_k,

$$\hat{H}|\Psi\rangle = E|\Psi\rangle. \tag{2.1}$$

Here, E is the energy of a stationary state and $\Psi(\{\boldsymbol{r}_i\sigma_i\}, \{\boldsymbol{R}_k\})$ the many-body wave function depending on all electron positions and spins $\boldsymbol{r}_i\sigma_i$ as well as on all nuclear positions $\boldsymbol{R}_k$. The Hamiltonian consists of the kinetic energy of the electrons $\hat{T}_e$, the electron-electron interaction $\hat{V}_{ee}$, the electron-nuclei interaction $\hat{V}_{en}$, the kinetic energy of the nuclei $\hat{T}_n$ and the nuclei-nuclei interaction $\hat{V}_{nn}$ it is given by

$$\begin{aligned}\hat{H} &= -\frac{1}{2}\sum_{i=1}^{N}\Delta_i + \frac{1}{2}\sum_{i\neq j}\frac{1}{|\boldsymbol{r}_i - \boldsymbol{r}_j|} - \sum_{i=1}^{N}\sum_{k=1}^{K}\frac{Z_k}{|\boldsymbol{r}_i - \boldsymbol{R}_k|} - \frac{1}{2}\sum_{k=1}^{K}\frac{1}{M_k}\Delta_k + \frac{1}{2}\sum_{k\neq l}\frac{Z_k Z_l}{|\boldsymbol{R}_k - \boldsymbol{R}_l|} \\ &= \hat{T}_e + \hat{V}_{ee} + \hat{V}_{en} + \hat{T}_n + \hat{V}_{nn}\end{aligned} \tag{2.2}$$

Throughout the thesis, we will use atomic units where $m = \hbar = 1$ and $\frac{e^2}{4\pi\varepsilon_0} = 1$.

The coupled electron-nuclear problem described by the Hamiltonian (Eq. 2.2) cannot be solved for complex systems, therefore, we use the Born-Oppenheimer approximation to separate the nuclear and electronic motion [27]. This approximation makes use of the fact that the electrons and nuclei move at different timescales which allows us to separate the Hamiltonian into an electronic and nuclear part. As a result, the Hamiltonian for the electrons consists of the following three terms:

$$\hat{H}_{elec} = -\sum_{\mathrm{i}} \frac{1}{2}\Delta_i + \sum_{i=1}^{N} v_{ext}(\boldsymbol{r}) + \frac{1}{2}\sum_{i \neq j} \frac{1}{|\boldsymbol{r}_i - \boldsymbol{r}_j|} = \hat{T} + \hat{V}_{ext} + \hat{V}_{ee}, \tag{2.3}$$

where $v_{ext}(\boldsymbol{r}) = -\sum_{k=1}^{K} \frac{Z_k}{|\boldsymbol{r}_i - \boldsymbol{R}_k|}$ is the electrostatic potential of all nuclei felt by one electron. Solving the corresponding stationary Schrödinger equation gives us energies E now also dependent on the nuclear positions as parameters.

$$\hat{H}_{elec}\Psi_q(\{\boldsymbol{r}_i\sigma_i\}, \{\boldsymbol{R}_k\}) = E_q(\{\boldsymbol{R}_k\})\Psi_q(\{\boldsymbol{r}_i, \sigma_i\}, \{\boldsymbol{R}_k\}), \tag{2.4}$$

where Ψ_q is the many-electron wave function with q as an abbreviation for the set of quantum numbers depending on the electron coordinates $\boldsymbol{r}_i\sigma_i$ and fixed nuclear position $\boldsymbol{R}_k$ now as parameters. The Hamiltonian for the nuclei with the nuclear wave function $\Psi_{nucl}(\{\boldsymbol{R}_k\})$ describes the motion of the nuclei in the potential energy surface $E_{tot}\left(\{\boldsymbol{R}_k\}\right)$ obtained by solving the electronic problem and adding inter-nuclear Coulomb repulsion.

$$\hat{H}_{nucl} = -\sum_k \frac{\Delta_k}{2M_k} + E_{elec}\left(\{\boldsymbol{R}_k\}\right) + \frac{1}{2}\sum_{k \neq l} \frac{Z_k Z_l}{|\boldsymbol{R}_k - \boldsymbol{R}_l|} = -\sum_k \frac{\Delta_k}{2M_k} + E_{tot}\left(\{\boldsymbol{R}_k\}\right) \tag{2.5}$$

The solution to the electronic part (Eq. 2.3) scales exponentially with the number of electrons N and therefore cannot be solved numerically. Another difficulty is the storage of the full many-body wave function on a numerical grid which would take up an enormous amount of memory, which is known as Van Vleck catastrophy [28]. Instead, we use density functional theory (DFT) (see Section 2.3) which makes use of the electron density, only scaling as N^3.

2.2 Many-electron wave function

This interlude section gives a description of the many-electron wave function and how to include the antisymmetric behavior of fermions. The many-electron wave function is a function of position and spin $\{\boldsymbol{r}_i\sigma_i\}$ of each electron i

$$\Psi(\boldsymbol{x}_1, \boldsymbol{x}_2, ..., \boldsymbol{x}_N) = \Psi(\{\boldsymbol{r}_1\sigma_1\}, \{\boldsymbol{r}_2\sigma_2\}, ...\{\boldsymbol{r}_N\sigma_N\}). \tag{2.6}$$

It is composed of orbitals, single particle functions, $\chi(\boldsymbol{x})$ consisting of a spatial part $\varphi(\boldsymbol{r})$ and spin parts $\alpha(\sigma)$ and $\beta(\sigma)$ for spin-up and -down .

$$\begin{aligned} \chi_\alpha(\boldsymbol{x}) &= \varphi(\boldsymbol{r})\alpha(\sigma) \\ \chi_\beta(\boldsymbol{x}) &= \varphi(\boldsymbol{r})\beta(\sigma) \end{aligned} \tag{2.7}$$

The wave function has to fulfill the Pauli exclusion principle such that it is antisymmetric with respect to particle interchange

$$\Psi(\boldsymbol{x}_1, ..., \boldsymbol{x}_i, ..., \boldsymbol{x}_j, ..., \boldsymbol{x}_N) = -\Psi(\boldsymbol{x}_1, ..., \boldsymbol{x}_j, ..., \boldsymbol{x}_i, ..., \boldsymbol{x}_N). \tag{2.8}$$

Therefore we cannot make a simple product ansatz. As the most simple ansatz, to also include the Pauli principle, we use the Slater determinant as an approximation

$$\Psi\left(\boldsymbol{x}_1, \boldsymbol{x}_2, \ldots, \boldsymbol{x}_N\right)=\frac{1}{\sqrt{N!}}\left|\begin{array}{cccc}\chi_i\left(\boldsymbol{x}_1\right) & \chi_j\left(\boldsymbol{x}_1\right) & \ldots & \chi_k\left(\boldsymbol{x}_1\right) \\ \chi_i\left(\boldsymbol{x}_2\right) & \chi_j\left(\boldsymbol{x}_2\right) & \ldots & \chi_k\left(\boldsymbol{x}_2\right) \\ \vdots & \vdots & \vdots & \vdots \\ \chi_i\left(\boldsymbol{x}_N\right) & \chi_j\left(\boldsymbol{x}_N\right) & \ldots & \chi_k\left(\boldsymbol{x}_N\right)\end{array}\right| . \tag{2.9}$$

To construct the ground state configuration of a system, we are filling up the orbitals according to Hund's first rule, that spin parallel electrons are preferred, starting with the lowest orbital. The highest occupied molecular orbital is called the HOMO and the lowest unoccupied molecular orbital is the LUMO. We are dealing with a closed shell system if there is an even number of electrons and an open shell system if the number is odd. The closed shell system, which is in most cases a spin-singlet, can be described as a single Slater determinant according to Roothaan [29] and therefore the calculations can be performed spin-unpolarized (spatial parts of spin-up and -down are identical, degenerate in energy) . For open shell systems, we have to perform spin-polarized (unrestricted) so the orbitals sharing a spatial wave function are not degenerate. In contrast, spin-unpolarized (restricted) calculations for open-shell systems, where the spin wave functions are forced to have an identical spatial part, are higher in energy but require lower computational cost.

2.3 Density functional theory

The basic idea of DFT is that the ground state properties of any system can be described as a functional of the ground state electron density $n_\sigma(\boldsymbol{r})$ [30] which is related to the many-electron wave function by the following expression

$$n_\sigma(\boldsymbol{r})=N \sum_{\sigma_2 \cdots \sigma_N} \int \mathrm{d}^3 r_2 \cdots \int \mathrm{d}^3 r_N\left|\psi\left(\boldsymbol{r} \sigma, \boldsymbol{r}_2 \sigma_2, \cdots, \boldsymbol{r}_N \sigma_N\right)\right|^2 . \tag{2.10}$$

Note that due to the normalization $\langle\psi | \psi\rangle=1$, the integration of the spin density $n_\sigma(\boldsymbol{r})$ over $\boldsymbol{r}$ and summation over the spins σ leads to the total number of electrons N. One can get the ground state energy by using the Rayleigh-Ritz minimal principle $E=\min_\Psi\left\langle\Psi\left|\hat{H}\right| \Psi\right\rangle$ and varying of all possible wave functions Ψ. This was shown by Hohenberg and Kohn [30] and later as the "constrained search formalism" by Levy [31]. For all wave functions Ψ leading to the density n we can define an energy functional

$$E[n(\boldsymbol{r})]=\min_{\Psi \rightarrow n}\langle\Psi|\hat{H}| \Psi\rangle=\min_{\Psi \rightarrow n}\left\langle\Psi\left|\hat{T}+\hat{V}_{ee}\right| \Psi\right\rangle+\int \mathrm{d}^3 r v(\boldsymbol{r}) n(\boldsymbol{r}) \geq E_0, \tag{2.11}$$

where one can introduce the universal functional $F[n(\boldsymbol{r})]$, which is independent of the external potential $v_{ext}(\boldsymbol{r})$,

$$F[n(\boldsymbol{r})]=\min_{\Psi \rightarrow n}\left\langle\Psi\left|\hat{T}+\hat{V}_{ee}\right| \Psi\right\rangle . \tag{2.12}$$

The ground state energy E_0 can therefore be determined by minimizing over all densities under the constraint $N = \int \mathrm{d}^3 r n(\boldsymbol{r})$

$$E_0 = \min_{n(\boldsymbol{r})} \left\{ F[n(\boldsymbol{r})] + \int \mathrm{d}^3 r v(\boldsymbol{r}) n(\boldsymbol{r}) \right\}. \tag{2.13}$$

This is known as the Hohenberg-Kohn minimum principle [30]. These basic theorems tell us that the ground state electron density is uniquely determined by the external potential $v_{ext}(\boldsymbol{r})$ (up to a constant) and leads to the ground state energy E_0 [30]. However, this requires that the universal functional is known. To overcome this difficulty, the original problem of interacting electrons can be mapped onto a fictitious system of non-interacting electrons ($\hat{V}_{ee} \equiv 0$) with the same electron density. This leads to single-electron Schrödinger equations with an effective potential $v_s(\boldsymbol{r})$, the so-called Kohn-Sham potential.

$$H\varphi_j(\boldsymbol{r}) = \left[-\frac{1}{2}\Delta + v_s(\boldsymbol{r}) \right] \varphi_j(\boldsymbol{r}) = \varepsilon_j \varphi_j(\boldsymbol{r}). \tag{2.14}$$

$$v_s(\boldsymbol{r}) = v_{ext}(\boldsymbol{r}) + v_H([n], \boldsymbol{r}) + v_{xc}([n], \boldsymbol{r}) = v_{ext}(\boldsymbol{r}) + \frac{\delta U[n(\boldsymbol{r})]}{\delta n(\boldsymbol{r})} + \frac{\delta E_{xc}[n(\boldsymbol{r})]}{\delta n(\boldsymbol{r})} \tag{2.15}$$

This potential $v_s(\boldsymbol{r})$ consists of the external potential $v_{ext}(\boldsymbol{r})$ due to the nuclei and two additional terms, namely the Hartree potential $v_H(\boldsymbol{r})$, which is the electrostatic potential created by the charge density $n(\boldsymbol{r})$, and the exchange-correlation potential $v_{xc}(\boldsymbol{r})$. These additional terms can also be written as the functional derivative of the Hartree energy $U[n(\boldsymbol{r})]$ and the exchange-correlation energy $E_{xc}[n(\boldsymbol{r})]$, respectively. Here, the Hartree energy is the classical electrostatic self-repulsion of the charge density

$$U[n(\boldsymbol{r})] = \frac{1}{2} \int \mathrm{d}^3 r \int \mathrm{d}^3 r' \, \frac{n(\boldsymbol{r}) n\left(\boldsymbol{r}'\right)}{|\boldsymbol{r} - \boldsymbol{r}'|}. \tag{2.16}$$

The energy functional now consists of the following:

$$E[n] = T_s[n] + U[n] + \int \mathrm{d}^3 r \, v_{ext}(\boldsymbol{r}) n(\boldsymbol{r}) + E_{xc}[n], \tag{2.17}$$

with $T_s[n]$ being the kinetic energy of the non-interacting system. The eigenvalues ε_j are the Kohn-Sham energies, and the eigenfunctions $\varphi_j(\boldsymbol{r})$ the Kohn-Sham orbitals from which the density can then be constructed as follows:

$$n(\boldsymbol{r}) = \sum_{j=1}^{N} |\varphi_j(\boldsymbol{r})|^2 \tag{2.18}$$

It should be noted that the Kohn-Sham energies are per se no physical quantities. However, can be given a physical meaning by means of Janak's theorem [32]. It states that the Kohn-Sham energies describe the derivative of the total energy E by the fractional occupation f_i of a given orbital i

$$\frac{\partial E}{\partial f_i} = \epsilon_i. \tag{2.19}$$

This is only valid for $i = N$ and $i = N+1$ in order to stay in the electronic ground state. Equations 2.14, 2.15 and 2.18 provide a scheme to calculate the electron density iteratively in a self-consistent field (SCF) cycle since the effective potential $v_s(\boldsymbol{r})$ depends on the density. Up to this point, DFT is an exact theory to obtain the electronic ground state but in practice, we have to approximate the exchange-correlation energy $E_{xc}[n]$. In Section 2.3.1, we will introduce some of the numerous available approximations, specifically the local density approximation (LDA), generalized gradient approximation (GGA) and hybrid functionals that are used in this work.

2.3.1 Approximations for the exchange-correlation energy E_{xc}

Local density approximation

The simplest way to approximate the exchange-correlation energy functional $E_{xc}[n]$ is the local density approximation (LDA) or local spin density approximation (LSDA) which has already been proposed by Kohn and Sham [33]. It is defined as

$$\begin{aligned} E_{xc}^{\mathrm{LDA}}[n] &= \int n(\boldsymbol{r}) \left[\varepsilon_x^{\mathrm{unif}}(n(\boldsymbol{r})) + \varepsilon_c^{\mathrm{unif}}(n(\boldsymbol{r}))\right] d^3r \\ E_{xc}^{\mathrm{LSDA}}\left[n_\uparrow, n_\downarrow\right] &= \int n(\boldsymbol{r}) \left[\varepsilon_x^{\mathrm{unif}}\left(n_\uparrow(\boldsymbol{r}), n_\downarrow(\boldsymbol{r})\right) + \varepsilon_c^{\mathrm{unif}}\left(n_\uparrow(\boldsymbol{r}), n_\downarrow(\boldsymbol{r})\right)\right] d^3r \end{aligned} \tag{2.20}$$

In this approximation, the exchange-correlation functional depends on the electron density $n(\boldsymbol{r})$, in the case of LDA, and on the spin densities $n_\uparrow(\boldsymbol{r})$, $n_\downarrow(\boldsymbol{r})$, in case of LSDA, of the inhomogeneous system and $\varepsilon_{xc}^{\mathrm{unif}} = \varepsilon_x^{\mathrm{unif}} + \varepsilon_c^{\mathrm{unif}}$ is the exchange-correlation energy per particle of a uniform electron gas. In the L(S)DA, it is assumed that the total exchange-correlation energy of some density distribution $n(\boldsymbol{r})$ can be described by the sum of the local contributions of the uniform electron gas with the same density $n(\boldsymbol{r})$ at $\boldsymbol{r}$. In the limit of a uniform electron gas, the L(S)DA is exact since, both, $\varepsilon_x^{\mathrm{unif}}$ and $\varepsilon_c^{\mathrm{unif}}$ are treated exactly, where the former is obtained analytically and the latter from quantum Monte-Carlo simulations. In practice, LDA works well for homogeneous systems, such as solids, but is less accurate for molecules because of their strongly varying electron density.

Generalized gradient approximation

Compared to the local (spin) density approximation, the generalized gradient approximation (GGA), like the PBE-GGA by Perdew, Burke, and Ernzerhof [22], not only depends on the density $n(\boldsymbol{r})$ at $\boldsymbol{r}$ but also on its gradient $\nabla n(\boldsymbol{r})$.

$$\mathrm{E}_{xc}^{\mathrm{GGA}}\left(n_\uparrow(\boldsymbol{r}), n_\downarrow(\boldsymbol{r})\right) = \int f\left(n_\uparrow(\boldsymbol{r}), n_\downarrow(\boldsymbol{r}), \nabla n_\uparrow(\boldsymbol{r}), \nabla n_\downarrow(\boldsymbol{r})\right) d^3r \tag{2.21}$$

The GGA improves on the underestimation of the bond lengths in molecules and the lattice parameters of solids in L(S)DA but it sometimes underbinds, therefore, overestimates these quantities. In conclusion, even though, GGA is commonly used for solids, it is still not accurate for molecules since it does not include van der Waals interactions. Furthermore, it underestimates the gap between the highest occupied molecular orbital (HOMO) and lowest unoccupied molecular orbital (LUMO) and the orbital energies can be inaccurate due to self-interaction errors.

GGA+U

LSDA and GGA fail at describing the ground state properties of correlated materials, where the d and f electrons are strongly localized, like in the case of Mott-insulators. For example, they give too small correlation gaps for the $3d$-transition metal oxides CoO and FeO [34, 35]. This stems from the inaccurate description of the strong Coulomb repulsion between the localized $3d$ electrons leading to orbital degeneracy [16]. The spin degeneracy is accounted for in the homogeneous electron gas by Hund's rule entering the single Slater-determinant description of the wave functions. To also account for orbital degeneracy of the d and f bands in correlated materials, the Hubbard U parameter is used to describe both degeneracies [15]. Introducing a simplified (screened) Hartree-Fock term $E_{\mathrm{HF}}(\hat{n})$ for the strong intra-atomic interaction, as an on-site replacement of the semilocal functional. Therefore, the double-counting term $E_{\mathrm{dc}}(\hat{n})$ has to be subtracted. Here, $\hat{n}$ is the on-site occupancy matrix of the d and f electrons [15]

$$E_{xc}^{\mathrm{LSDA/GGA}+U}(n,\hat{n}) = E_{xc}^{\mathrm{LSDA/GGA}}(n) + E_{\mathrm{HF}}(\hat{n}) - E_{\mathrm{dc}}(\hat{n}). \tag{2.22}$$

In the study of the transition metal complexes we use Dudarev's approach with an effective $U_{\mathrm{eff}} = U - J$ which is a simplified (rotationally invariant) approach [16].

Hybrid functionals

Hybrid functionals use a combination of exact Hartree-Fock exchange and a semilocal approximation (sl), like the GGA or LDA correlation functionals. For example, the PBE0 (PBEh) hybrid functional by Perdew et al. [12–14] is defined as

$$E_{xc}^{\mathrm{PBE0}} = E_{xc}^{\mathrm{PBE}} + \frac{1}{4}\left(E_x - E_x^{\mathrm{PBE}}\right) = \frac{3}{4}E_x^{\mathrm{PBE}} + \frac{1}{4}E_x + E_c^{\mathrm{PBE}}, \tag{2.23}$$

with E_x^{PBE} and E_c^{PBE} being the PBE-GGA functional as the semilocal approximation mentioned above. It improves the accuracy for molecules since it reduces the self-interaction error introduced by approximating the exchange functional. However, it is computationally more expensive and therefore rarely used for large systems.
In addition to *global* hybrids, there are also so-called *range-separated* hybrid functionals, like the HSE functional of Heyd, Scuseria, and Ernzerhof [11, 36], that allow for an improvement in the computational cost. These split the full $1/r$ Coulomb potential into a short range (SR) and long range (LR) part defined by the screening parameter ω

$$\frac{1}{r} = \underbrace{\frac{1-\mathrm{erf}(\omega r)}{r}}_{\mathrm{SR}} + \underbrace{\frac{\mathrm{erf}(\omega r)}{r}}_{\mathrm{LR}}. \tag{2.24}$$

The exchange-correlation energy is then given by

$$E_{xc}^{\text{HSE}} = \frac{1}{4}E_x^{\text{HF,SR}}(\omega) + \frac{3}{4}E_x^{\text{PBE,SR}}(\omega) + E_x^{\text{PBE,LR}}(\omega) + E_c^{\text{PBE}}. \tag{2.25}$$

When $\omega = 0$, we get the PBE0 functional (Eq. 2.23) and when $\omega \to \infty$, the usual PBE functional [22]. Note that in the HSE functional, the exact Hartree-Fock exchange is only included in the short range. Additionally to that, there are also *range-separated* hybrid functionals that use exact exchange in the long range. What functional is best to use depends on the system and the properties of interest.

2.4 Methodologies

2.4.1 Plane wave basis set

The Kohn-Sham orbitals $\varphi_j(\boldsymbol{r})$ can be expanded in a linear combination of known basis functions $\phi_i(\boldsymbol{r})$.

$$\varphi_j(\boldsymbol{r}) = \sum_i c_i^{(j)} \phi_i(\boldsymbol{r}) \tag{2.26}$$

In DFT this is done for solving the Kohn-Sham equations 2.14. Since in this work we are mainly interested in a lattice-periodic Kohn-Sham potential, the Kohn-Sham orbitals are in fact Bloch waves, a plane wave times a lattice periodic function $u_{\boldsymbol{k}}(\boldsymbol{r})$.

$$\varphi_{\boldsymbol{k}}(\boldsymbol{r}) = e^{i\boldsymbol{k}\cdot\boldsymbol{r}} u_{\boldsymbol{k}}(\boldsymbol{r}) \quad \text{with} \quad u_{\boldsymbol{k}}(\boldsymbol{r}+\boldsymbol{R}) = u_{\boldsymbol{k}}(\boldsymbol{r}). \tag{2.27}$$

Here, $\boldsymbol{k}$ is a wave vector in the first Brillouin zone due to $e^{i(\boldsymbol{k}+\boldsymbol{G})\cdot\boldsymbol{R}} = e^{i\boldsymbol{k}\cdot\boldsymbol{R}}$ with $\boldsymbol{R}$ and $\boldsymbol{G}$ being the lattice vector and reciprocal lattice vector, respectively. We can choose $e^{i\boldsymbol{G}\cdot\boldsymbol{r}}$ as basis functions $\phi_i(\boldsymbol{r})$

$$\phi_{\boldsymbol{G}}(\boldsymbol{r}) = \frac{1}{\sqrt{\Omega}} e^{i\boldsymbol{G}\boldsymbol{r}}, \tag{2.28}$$

where Ω is the crystal volume. For this plane wave basis, the expansion according to Equation 2.26 results in a Fourier expansion

$$\varphi_{\boldsymbol{k}}(\boldsymbol{r}) = e^{i\boldsymbol{k}\boldsymbol{r}} \sum_{\boldsymbol{G}} c_{\boldsymbol{G}}(\boldsymbol{k}) \phi_{\boldsymbol{G}}(\boldsymbol{r}) = \sum_{\boldsymbol{G}} c_{\boldsymbol{G}}(\boldsymbol{k}) \phi_{\boldsymbol{k}+\boldsymbol{G}}(\boldsymbol{r}) = \frac{1}{\sqrt{\Omega}} \sum_{\boldsymbol{G}} c_{\boldsymbol{G}}(\boldsymbol{k}) e^{i(\boldsymbol{k}+\boldsymbol{G})\boldsymbol{r}}, \tag{2.29}$$

with the expansion coefficients $c_{\boldsymbol{G}}(\boldsymbol{k})$ for a specific Bloch wave at a given wave vector $\boldsymbol{k}$. Consequently, also the electron density $n(\boldsymbol{r})$ (Equation 2.18) and the Kohn-Sham potential $v_s(\boldsymbol{r})$ (Equation 2.15) can be expanded in a Fourier series.

When inserting this plane wave ansatz into the Kohn-Sham equations 2.14, now with orbitals and energies dependent on $\boldsymbol{k}$, we obtain a matrix equation, the so-called secular equation,

$$\sum_{\boldsymbol{G}'} H_{\boldsymbol{G}\boldsymbol{G}'}(\boldsymbol{k}) c_{\boldsymbol{G}'}(\boldsymbol{k}) = \varepsilon_{\boldsymbol{k}} \sum_{\boldsymbol{G}'} S_{\boldsymbol{G}\boldsymbol{G}'} c_{\boldsymbol{G}'}(\boldsymbol{k}). \tag{2.30}$$

The $H_{\boldsymbol{GG'}}$ and the $S_{\boldsymbol{GG'}}$ are the Hamiltonian and overlap matrix, respectively. Since the plane waves are orthonormal to each other, the overlap matrix is simply the identity matrix hence

$$\sum_{\boldsymbol{G'}} H_{\boldsymbol{GG'}}(\boldsymbol{k}) c_{\boldsymbol{G'}}(\boldsymbol{k}) = \varepsilon_{\boldsymbol{k}} c_{\boldsymbol{G}}(\boldsymbol{k}). \tag{2.31}$$

The sum over $\boldsymbol{G'}$ must be cut off at a specific cut-off wave number G_{cut} because, in practice, we cannot sum over infinitely many reciprocal lattice vectors, thus we can write:

$$\sum_{\boldsymbol{G'}}^{|\boldsymbol{G'}| \leq G_{\text{cut}}} H_{\boldsymbol{GG'}}(\boldsymbol{k}) c_{\boldsymbol{G'}}(\boldsymbol{k}) = \varepsilon_{\boldsymbol{k}} c_{\boldsymbol{G}}(\boldsymbol{k}). \tag{2.32}$$

Here, we can define the plane wave cut-off by the cut-off energy $E_{\text{cut}} = \frac{G_{\text{cut}}^2}{2}$ which is the kinetic energy associated with the cut-off wave vector.

One advantage of the plane wave basis set is that by adding more plane waves the accuracy can be improved in a systematic way. Additionally, plane waves are easy to transform into Fourier space by fast Fourier transform (FFT) which speeds up the calculations. The drawback of plane waves is that they describe the rapidly varying electron density close to the core very poorly. It would need more basis functions to describe the electron density in this region correctly which would increase the computational cost. The solution to this problem is pseudopotentials [37, 38] to account for valence-core interactions. The resulting pseudo wave functions ideally do not have any nodes close to the core, consequently, fewer basis functions are needed in total which reduces the computational cost. There are various methods available, such as norm-conserving pseudo-potentials [39] and ultra-soft pseudo-potentials [40].

In the context of a plane wave basis, the projector augmented waves (PAW) method [41, 42] is nowadays the most widely used. This approach uses pseudo wavefunctions to describe the rapid oscillations close to the nuclei and plane waves in the regions between them. Therefore, the real-space is divided into spheres centered around the atoms and an interstitial region for the bonds. This brings together the pseudopotential approach and the augmented wave methods. The plane wave code VASP [5–7], which is used for all calculations performed in this thesis, utilizes these PAW potentials.

2.4.2 Interfaces

For the calculations, we are restricted to periodic boundary conditions due to the plane wave basis functions (Section 2.4.1) used in VASP. This is not a drawback because in alternative cluster calculations with open boundary conditions, there is the major disadvantage of dangling bonds at the boundary when modeling extended systems. Simulating molecule-substrate interfaces can be conveniently done with applied periodic boundary conditions using the repeated slab approach [21].

Here, the unit cell, that is repeated in all three dimensions, is set up by simulating the substrate by a finite number of atomic layers and introducing a vacuum gap of around 20 Å in z-direction between the slabs to decouple them quantum mechanically.

Additionally, the slabs need to be decoupled electrostatically because there cannot be a net dipole moment within the unit cell. Charge rearrangements or polar molecules create a dipole moment in the system leading to an electric field and hence artificial polarization of the slab [3]. This field is large for small vacuum gaps and small for large vacuum gaps. So one possibility to avoid the artificial polarization would be to increase the size of the vacuum gap. However, this would increase the computational cost and slow down the convergence. The most common method to decouple the slabs electrostatically is to insert a dipole of the same magnitude but in opposite direction into the vacuum region [21, 43]. The calculation of the dipole moment is done within the SCF-cycle self-consistently and can automatically be included in the VASP calculation by using the INCAR settings `LDIPOL = .TRUE.` and `IDIPOL = 3` for setting the dipole direction to z. The approach is illustrated in Figure 2.1 for the 1,1'-bitetracene/Cu(111) system with six layers of copper and one molecule in the unit cell.

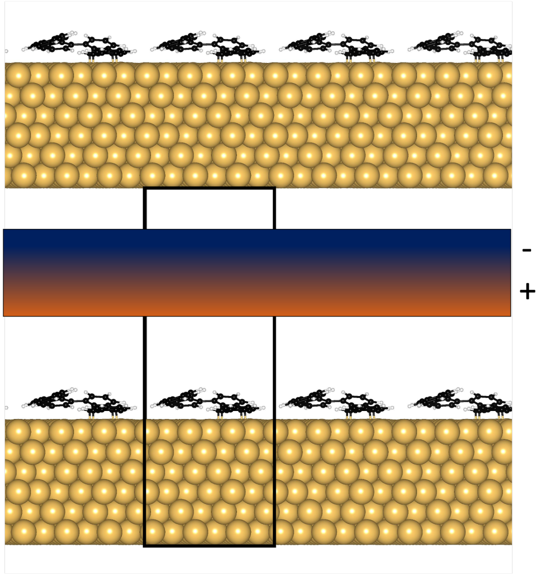

Figure 2.1: Illustration of the repeated slab approach for molecule-substrate interfaces.

2.4.3 Geometry Optimization

Damped molecular dynamics with a combination of Davidson [44] and RMM-DIIS minimization algorithm [45] is used for all geometry relaxations in this thesis by setting `IBRION = 3` and `ALGO = Fast`. For this, a simple velocity Verlet algorithm is used to integrate the damped second order equation of motion for the atomic nuclei which can be schematically written in the form

$$\ddot{\mathbf{x}} = -2\alpha\mathbf{F} - \mu\dot{\mathbf{x}}. \tag{2.33}$$

In VASP, one has to set the two parameters `SMASS` and `POTIM` which define the damping factor μ and constant α, respectively. $\mu = 0$ equals to no damping and $\mu = 2$ maximum damping which then reduces to a simple steepest descent algorithm. For the calculations in this thesis, the damping factor μ was set to `SMASS = 0.4` and α to `POTIM = 0.10`. Additionally, one can choose the maximum number of relaxation steps `NSW` and the convergence threshold `EDIFFG` for the Hellmann-Feynman forces acting on the atoms. This was set to `EDIFFG = -0.01` (eV/Å) in all calculations. So for each relaxation step the energy and forces are calculated and if all forces are below 0.01 eV/Å, the geometry relaxation is stopped.

2.4.4 Van der Waals corrections

Local or semilocal DFT functionals do not account for nonlocal and long-range van der Waals forces, also known as dispersion forces. These arise whenever there are charge density fluctuations leading to polarizations in the system as experienced for organic layers on surfaces [46]. To account for these forces there are two main approaches: *a-posteriori* dispersion corrections that are added to the energy and nonlocal vdW density functionals.

A-posteriori dispersion corrections E_{disp} are added to the exchange-correlation energy functional during the SCF cycle

$$E_{xc} = E_{xc}^{\text{SL/hybrid}} + E_{\text{disp}}. \tag{2.34}$$

These dispersion corrections E_{disp} are, in the simplest description, of the form

$$E_{\text{disp}} = -\frac{1}{2}\sum_{i \neq j} f_{\text{damp},6}(R_{ij})\frac{C_{6,ij}}{R_{ij}^6}. \tag{2.35}$$

Here, R_{ij} is the distance between atoms i and j and the geometry-dependency goes into the equation in means of the dispersion coefficients $C_{6,ij}$, also called effective interaction parameter, specified to the two atoms. Additionally, the damping function $f_{\text{damp},6}$ prevents double counting of the short range interactions. Depending on the dispersion correction scheme, the dispersion coefficients and the damping function do vary.

The most common family of *a-posteriori* dispersion methods are the DFT-Dx methods of Grimme et al. [47]. In this thesis, we will only make use of one of them, the DFT-D3 method [23], which includes geometry-dependent dispersion coefficients, in contrast to earlier outdated versions (DFT-D [48] and DFT-D2 [47]) not taking the chemical environment into account by relying on fixed coefficients. There are two different damping variants to this method to prevent double counting of the short range interactions. The first variant is a zero-damping DFT-D3(zero) (by setting `IVDW=11` in the VASP INCAR file) and the second variant is Becke-Johnson damping [49] DFT-D3(BJ) (by setting `IVDW=12` in the VASP INCAR file).

Alternatively, there are the Tkatchenko-Scheffler (TS) methods where the dispersion coefficients and damping function are charge-density dependent. The interaction parameters are rescaled using either Hirshfeld partitioning [50] (setting `IVDW=2` in the VASP INCAR file) or iterative Hirshfeld partitioning [51, 52] (setting `IVDW=21` in the VASP INCAR file).The Hirshfeld partitioning scheme can sometimes lead to wrongly assigned charges, for example in systems with strong charge transfer, because it partitions the charge according to the densities of free, neutral atoms [53]. By using an iterative Hirshfeld partitioning, this can be improved [52, 54].

A completely different approach to account for the vdW forces are nonlocal vdW density functionals (vdW-DF) of Dion et al. [55]. Here, the correlation energy is split into a semilocal correlation part and a nonlocal correlation part.

$$E_{xc}[n] = E_x^{PBE}[n] + E_c^{LDA}[n] + E_c^{nl}[n], \tag{2.36}$$

where $E_c^{nl}[n]$ is written as a nonlocal integral,

$$E_c^{nl}[n] = \frac{1}{2}\int d^3r d^3r' n(\boldsymbol{r})\phi(\boldsymbol{r},\boldsymbol{r}')n(\boldsymbol{r}') \tag{2.37}$$

where the pre-computed interaction kernel $\phi(\boldsymbol{r},\boldsymbol{r}')$ is a general function depending on the distance $r = |\boldsymbol{r}-\boldsymbol{r}'|$ and on the density n [55]. The interaction kernel ϕ varies for the different functionals depending on how the nonlocal correlations are added. In VASP one has to set the following parameters in the INCAR file

```
GGA = RE
AGGAC = 0.0
LUSE_VDW = .TRUE.
LASPH = .TRUE.
```

A modified version of the vdW-DF is the optB86b-vdW of Klimeš et al. [56] which is an extension of the B86b exchange-correlation functional, a type of GGA combined with the nonlocal correlation part. This gives more accurate lattice constants of solids compared to the original vdW-DF.

```
GGA = MK
PARAM1 = 0.1234
PARAM2 = 1.0
AGGAC = 0.0
LUSE_VDW = .TRUE.
LASPH = .TRUE.
```

3 Comparison of hybrid functional calculations to GGA+U

3.1 Motivation

For many years, transition metal complexes (TMCs) have been the subject of intense experimental and theoretical study [57–60]. Recently, they have regained a lot of attention due to the exploitation of their magnetic properties for optoelectronics, spintronics and quantum computing [8–10]. In this chapter, we focus on two important representatives of complexes between transition metal (TM) and organic molecules, namely TM-phthalocyanine (TMPc) and TM-porphine (TMP) [61]. In particular, we study the properties of these molecules for TM = Mn, Fe, Co, Ni, Cu and Zn which cover a range of magnetic spin moments from S = 3/2, 1, 1/2, 0, 1/2 and 0, respectively.

The metal-free parent compounds, phthalocyanine (H_2Pc) and porphine (H_2P) have a simple and stable molecular structure. H_2Pc ($H_2(C_8H_4N_2)_4$) consists of four isoindole ((C_8H_7N) (a benzene ring (C_6H_6) fused with pyrrole (C_4H_5N)) ligands connected by a ring of nitrogen atoms (Fig. 3.1a). Upon formation of the transition metal complex, the two hydrogen atoms in the center are then replaced by the TM (Fig. 3.1b). In Figure 3.2a and Figure 3.2b, we show porphine ($C_{20}H_{14}N_4$) consisting of four pyrrole groups linked with methine (CH) bridges and TMP, respectively. It is important to note that the metal ion in the center is in a $[\mathrm{TM}]^{2+}$ state and the d-orbitals of the TM transform under the D_{4h} symmetry as b_{2g} (d_{xy}), e_g ($d_{xz}, d_{yz} = d_\pi$), a_{1g} (d_{z^2}) and b_{1g} ($d_{x^2-y^2}$) [62]. These orbitals hybridize to some extent with the $2p$-states of the carbon and nitrogen atoms depending on their energy and symmetry. The highest occupied molecular orbital (HOMO) and lowest unoccupied molecular orbital (LUMO) are composed of delocalized a_{1u} and $2e_g$ π-orbitals, respectively, and, in some cases, hybridize with the d-states [59, 63, 64].

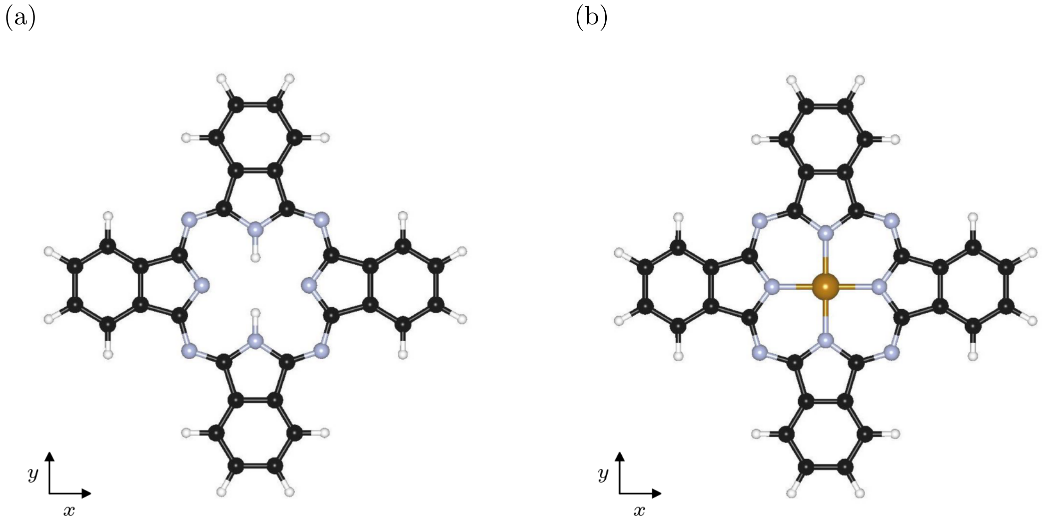

Figure 3.1: Chemical structure of (a) phthalocyanine (H_2Pc, $(C_8H_4N_2)_4H_2)$) and (b) transition metal phthalocyanine (TMPc). The C atoms are depicted in black, the H atoms in white, the N atoms in light blue and the metal in bronze.

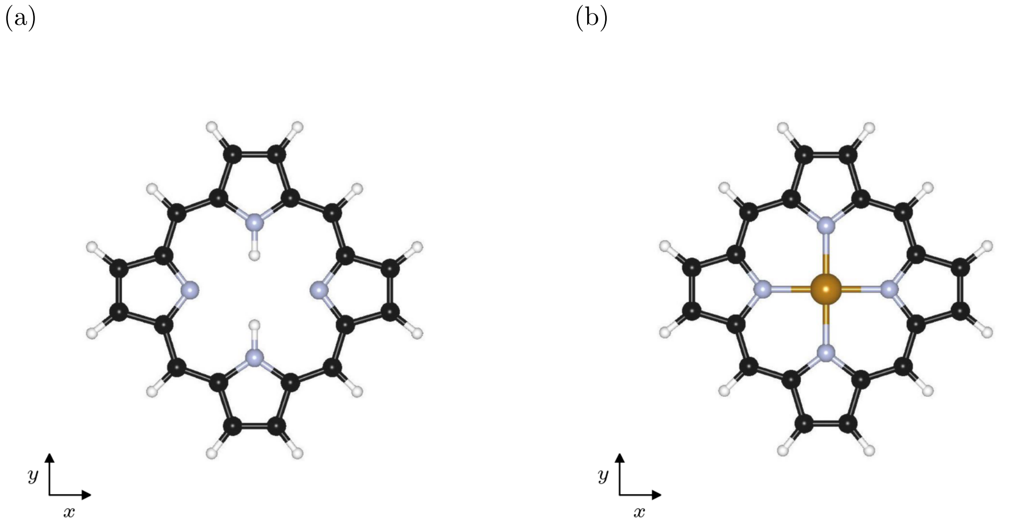

Figure 3.2: Chemical structure of (a) porphine (H_2P, $C_{20}H_{14}N_4$) and (b) transition metal porphine (TMP). The C atoms are depicted in black, the H atoms in white, the N atoms in light blue and the metal in bronze.

Computationally, the description of TMPcs and TMPs is challenging because the hybridization between the d-states of the TM and π-states of the organic macrocycle sensitively depends on their relative energy level alignment, which in turn, is prone to errors in density functional calculations. While hybrid functionals are known to be superior to semilocal functionals, the former are also computationally more expensive. This is particularly true for interfaces between TMPcs and TMPs with surfaces. Here, the deployment of cheaper methods, giving the same accuracy in the description of the d-orbitals, is of high interest. In this study, we compare the HSE06 [11] and PBEh [12–14] calculations of isolated TMPcs to the computationally much cheaper GGA+U approach [15, 16]. In particular, our aim is to determine the optimal U_{eff} value of Dudarev's approach [16] with the lowest deviation to the hybrid calculations in regards to the energies of the d-states. For this purpose, firstly, the HOMO-LUMO gaps, secondly, the ordering and occupation of the d levels and, thirdly, the magnetic moments are studied. Finally, we extend the analysis to the TMPs.

To sufficiently isolate the molecules from their periodic replica, a supercell with dimensions 25 Å×25 Å×12 Å was set up containing one molecule. This ensured that there was a horizontal distance of around 10 Å between the TMPcs and 14 Å between the TMPs and 12 Å distance in the vertical direction such that the wave functions of the individual molecules do not overlap. Before analyzing the electronic structure of the molecules, the geometries were optimized with the respective functional using damped molecular dynamics until the forces were below 0.01 eV/Å, as explained in Section 2.4.3. For the hybrid functional calculations, the optimized structure from the PBE-GGA [22] calculation was taken. Since TMCs have open d and possibly f shells, it is necessary to perform spin-polarized calculations by setting `ISPIN = 2` and `MAGMOM`, the initial magnetic moment per atom, in the VASP INCAR file. If the system did not converge to the correct magnetic moment in the performed GGA+U calculations, the calculations were initialized using an already converged CHGCAR and WAVECAR file from the standard PBE-GGA calculation or another GGA+U calculation of this system. In all calculations, a Γ-centered $1 \times 1 \times 1$ k-grid, first-order Methfessel-Paxton smearing of 0.15 eV [65] and 400 eV cut-off were used. For the GGA+U calculations, the U value was varied from 1 eV to 6 eV and the J value was kept at 0 eV resulting in U_{eff} in the range between 1 eV and 6 eV.

3.2 Transition Metal Phthalocyanine

In this section, we compare results obtained with the hybrid functional HSE06 [11] and PBEh [12–14] with the GGA+U [15, 16] calculations for TMPc in terms of the orbital ordering, the HOMO-LUMO gaps and magnetic moments. The PDOS is calculated by projecting the Kohn-Sham eigenstates of the full system $\psi_{n,\boldsymbol{k}}$ onto atomic orbitals ϕ_i, as follows

$$\rho_{\phi_i}(E) = \frac{1}{N_k} \sum_{n,\boldsymbol{k}} \left|\langle \phi_i \mid \psi_{n,\boldsymbol{k}} \rangle\right|^2 \delta\left(E - \epsilon_{n,\boldsymbol{k}}\right). \tag{3.1}$$

For the purpose of this study, we consider projections onto the d-orbitals of the transition metal, specifically onto the d_{xy} (blue), d_π (cyan), d_{z^2} (orange) and $d_{x^2-y^2}$ (green) orbitals. Note that the d_{xz} and d_{yz} orbitals are hybridized and here, their contributions are summed and denoted as d_π. The total DOS is indicated by the grey areas in all following figures.

First, we analyze the differences in the HSE06 [11] and PBEh [12–14] calculations. As an example, the total DOS and PDOS of FePc and NiPc are plotted in Figure 3.3, left and right panel, respectively. We observe that the orbital ordering is not affected by the choice of the hybrid functional but the HOMO-LUMO gap calculated with PBEh is by 0.6 eV larger compared to HSE06 for both, FePc and NiPc (see Fig. 3.5).

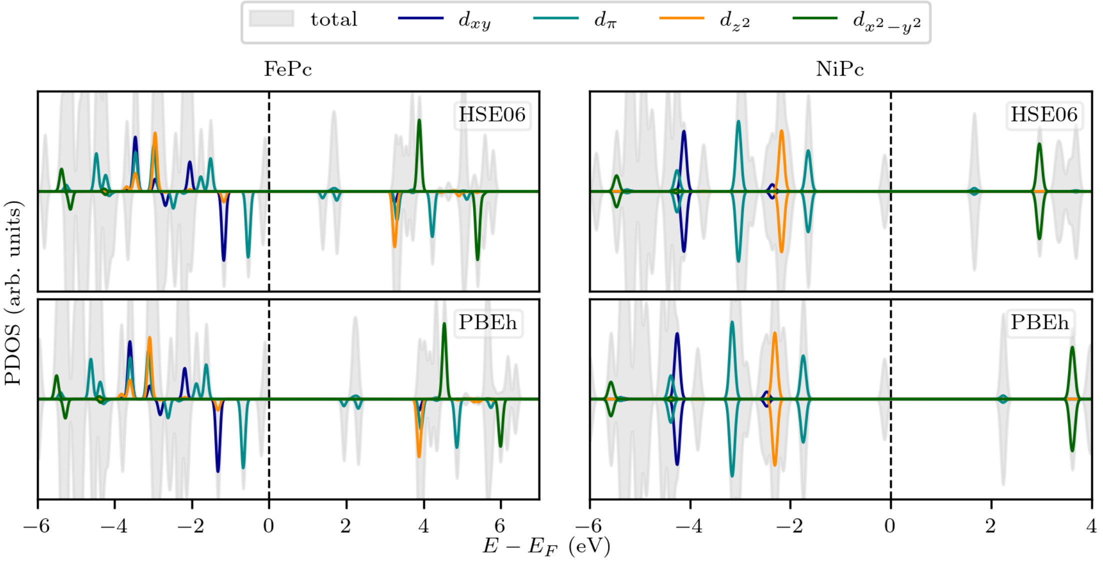

Figure 3.3: PDOS of FePc (left) and NiPc (right) calculated with HSE06 [11] and PBEh [12–14].

To analyze the influence of the U_{eff} value onto the orbital ordering and occupation of the d-states of the considered TMPcs, we compare the GGA+U to the HSE06 calculations. The plots of the PDOS in Figures 3.6-3.8 follow the same color scheme for the orbitals as in Figure 3.3. The electron filling scheme for TMPc according to Reference [64] is depicted in Figure 3.4.

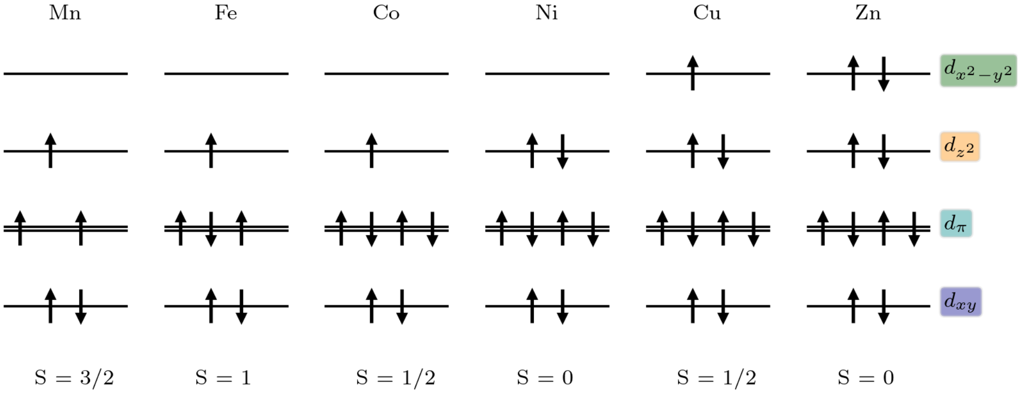

Figure 3.4: Electron filling scheme for TMPc according to Reference [64].

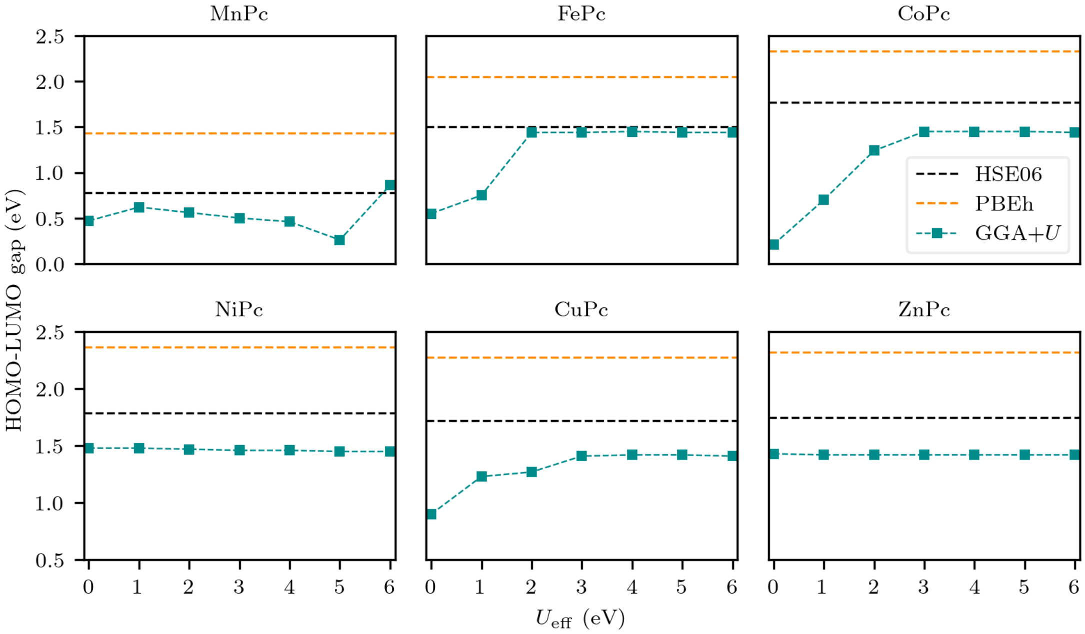

Figure 3.5: HOMO-LUMO gaps of TMPc as a function of U_{eff}. $U_{\text{eff}} = 0$ is the standard GGA-PBE calculation [22] and the HSE06 [11] and PBEh [12–14] calculations are indicated by the dashed lines.

We start the discussion with MnPc displayed in the left column of Figure 3.6. According to Reference [64], the filling of the orbitals for MnPc would be the following: The d_{xy} level is completely filled, the hybridized d_π-states are occupied by two spin-up electrons and the d_{z^2}-state by one spin-up electron (intermediate spin state), leading to a total spin moment of S = 3/2 (see Fig. 3.4). In the HSE06 calculation (Fig. 3.6, topmost left panel) also the d_{xy}-down state is unoccupied, however, still resulting in S = 3/2 due to contributions of other spin-down states being partially filled. These additional peaks of the d-states come from hybridization with the ligand states. By comparing the HSE06 to the GGA+U calculations, we observe that the occupied states shift to lower energies with increasing U_eff value, whereas, the unoccupied states do not show a collective shift in energy. For example, the $d_{x^2-y^2}$-up state slightly shifts to lower energies, in contrast to the d_{z^2}-down state, which shifts to higher energies. The HOMO is defined by one d_π-down state for $U_\text{eff} < 6$ eV as it sits at the Fermi level. However, the contribution decreases with increasing U_eff and the $d_{x^2-y^2}$-up state, which is unoccupied in the hybrid calculation, shifts towards lower energies until it is localized at the HOMO for $U_\text{eff} = 6$ eV. For this reason, the HOMO-LUMO gap is always defined by the metal d-states and changes by varying U_eff (see Fig. 3.5). $U_\text{eff} = 5$ eV is the most eligible choice considering the orbital energies but is inaccurate with respect to the orbital ordering because of the $d_{x^2-y^2}$-states.

For FePc, the d_{xy} level is completely filled, the hybridized d_π-states have one unoccupied spin-down state and the d_{z^2}-state is occupied by one spin-up electron (intermediate spin state), leading to a total spin moment of S = 1 (see Fig. 3.4) [64]. This occupation of the orbitals is fully captured by the hybrid functional (Fig. 3.6, topmost right panel). Due to the hybridization with the ligand states, multiple additional peaks of the d-states appear. The most similar results to HSE06 are achieved with $U_\text{eff} = 1$ eV since higher U_eff values lead to a position-'switching' of the d_{xy}-down state (now occupied) and one of the d_π-down states (now unoccupied). This governs the large deviation between the HSE06 and GGA+U calculations with $U_\text{eff} > 1$ eV, even though the energies of the other orbitals are better captured by $U_\text{eff} = 4$ eV. The HOMO-LUMO gap stays the same for $U_\text{eff} > 1$ eV since it is only defined by ligand states that are not affected by the choice of U_eff (Fig. 3.5).

For CoPc, the d_{xy} and d_π levels are completely filled and only the d_{z^2} is partially filled by one spin-up electron (low spin state), leading to a total spin moment of S = 1/2 (see Fig. 3.4) [64], which is well captured by the hybrid functional (Fig. 3.7, topmost left panel). The GGA+U calculation that shows the least deviations to HSE06 is the one with $U_\text{eff} = 6$ eV as the occupied (unoccupied) states shift to lower (higher) energies with increasing U_eff. This also explains the increase of the HOMO-LUMO gap (Fig. 3.5) up to $U_\text{eff} = 2$ eV since the d_{z^2}-down state is localized on the LUMO.

For NiPc, the low spin state is the ground state with fully occupied d_{xy}, d_π and d_{z^2}-states, leading to a non-magnetic solution (see Fig. 3.4) [64]. Figure 3.7 (right panel) shows that with increasing U_eff the deviations between the hybrid and GGA+U calculation get smaller, therefore $U_\text{eff} = 6$ is the most suitable. By increasing U_eff further, the result could probably be improved. The overall orbital ordering is well captured by all calculations and the HOMO-LUMO gap does not change since it is only localized on ligand states (Fig. 3.5).

For CuPc, the d_{xy}, d_{π} and d_{z^2} are completely filled and only the $d_{x^2-y^2}$-up state is occupied (low spin state), leading to a total spin moment of S = 1/2 (see Fig. 3.4) [64]. As for CoPc and NiPc, the deviations between the hybrid and GGA+U calculation get smaller with increasing U_{eff} as the position of the occupied (unoccupied) orbitals shift to lower (higher) energies (Fig. 3.8, left panel). This also leads to the HOMO-LUMO gap being unaffected by the metal d-states for $U_{\text{eff}} > 2$ eV.

Finally, ZnPc has a total spin moment of S = 0 (low spin state) and all metal d-orbitals are fully occupied (see Fig. 3.4) [64]. Here, the description of the orbital energies also gets closer to the HSE06 with increasing U_{eff} (Fig 3.8, right panel), and the HOMO-LUMO gap is only defined by ligand states for all calculations (Fig. 3.5). The occupation of the orbitals is correct, as well, however, the orbital ordering is different, with $d_{x^2-y^2}$ at the lowest energy and d_{z^2} at the second lowest.

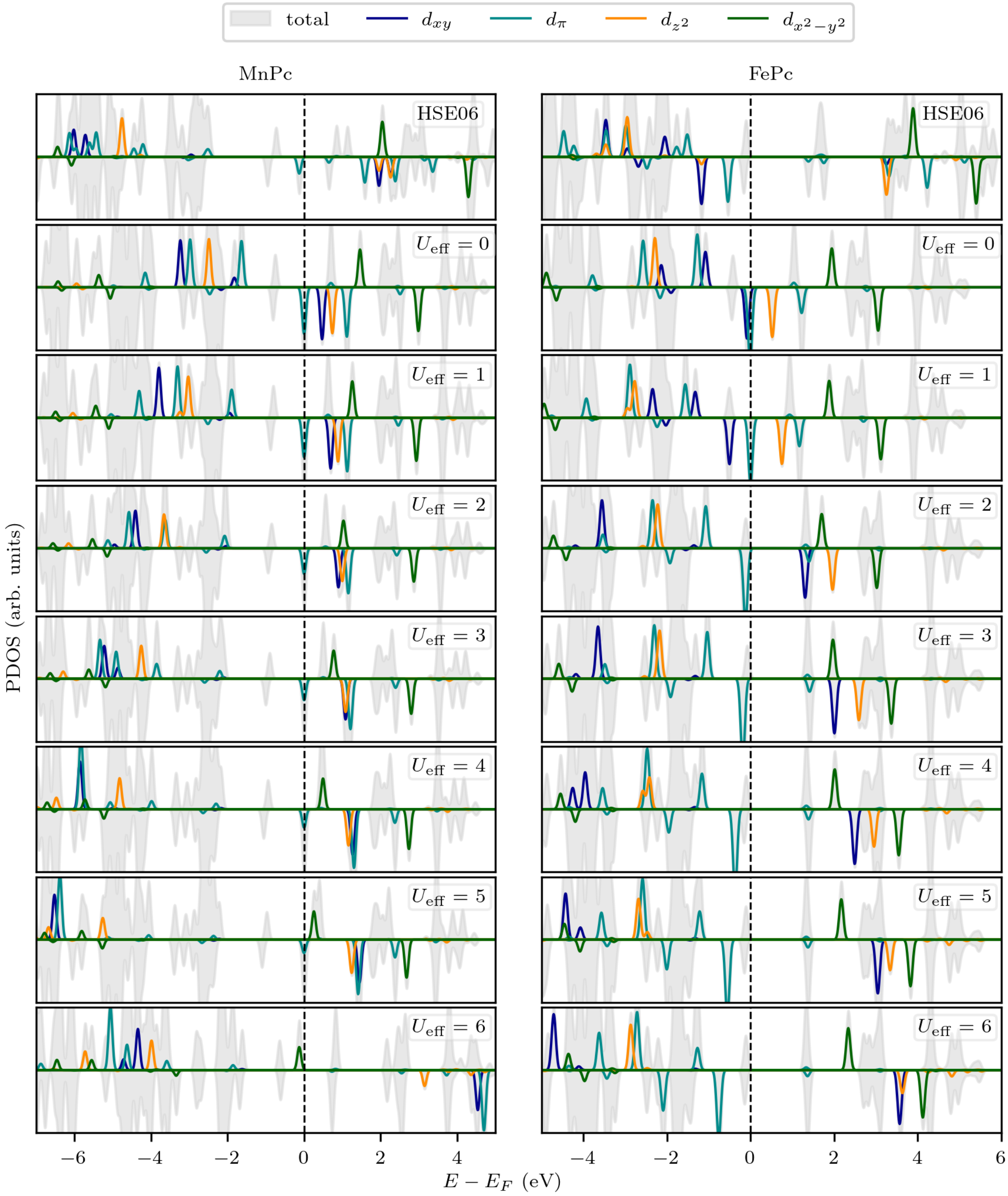

Figure 3.6: PDOS of MnPc (left) and FePc (right) calculated with HSE06 [11] (top) and GGA+U [15, 16]. U_{eff} was varied from 1 eV to 6 eV and $U_{\text{eff}} = 0$ is the standard GGA-PBE calculation [22].

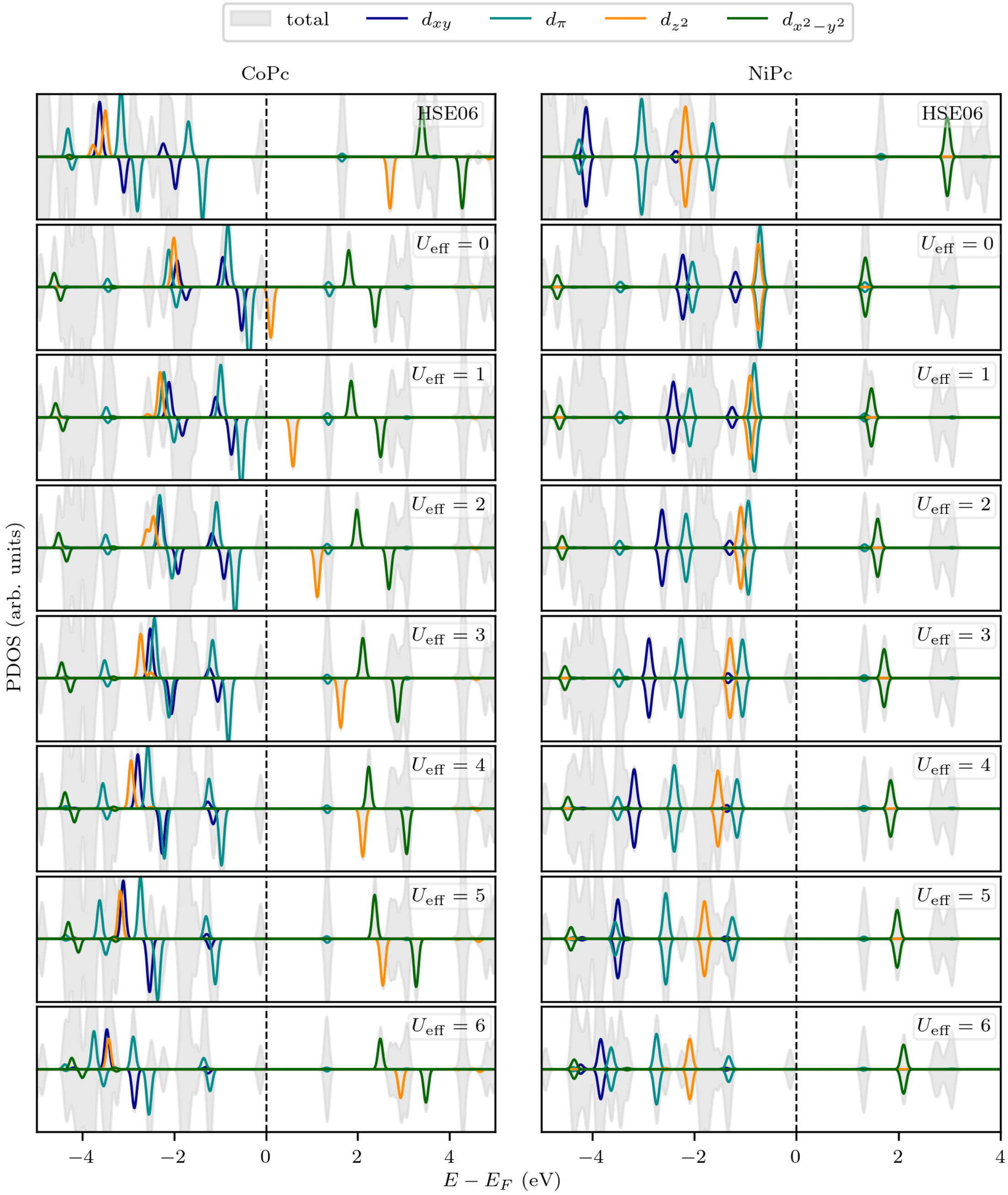

Figure 3.7: PDOS of CoPc (left) and NiPc (right) calculated with HSE06 [11] (top) and GGA+U [15, 16]. U_{eff} was varied from 1 eV to 6 eV and $U_{\text{eff}} = 0$ is the standard GGA-PBE calculation [22].

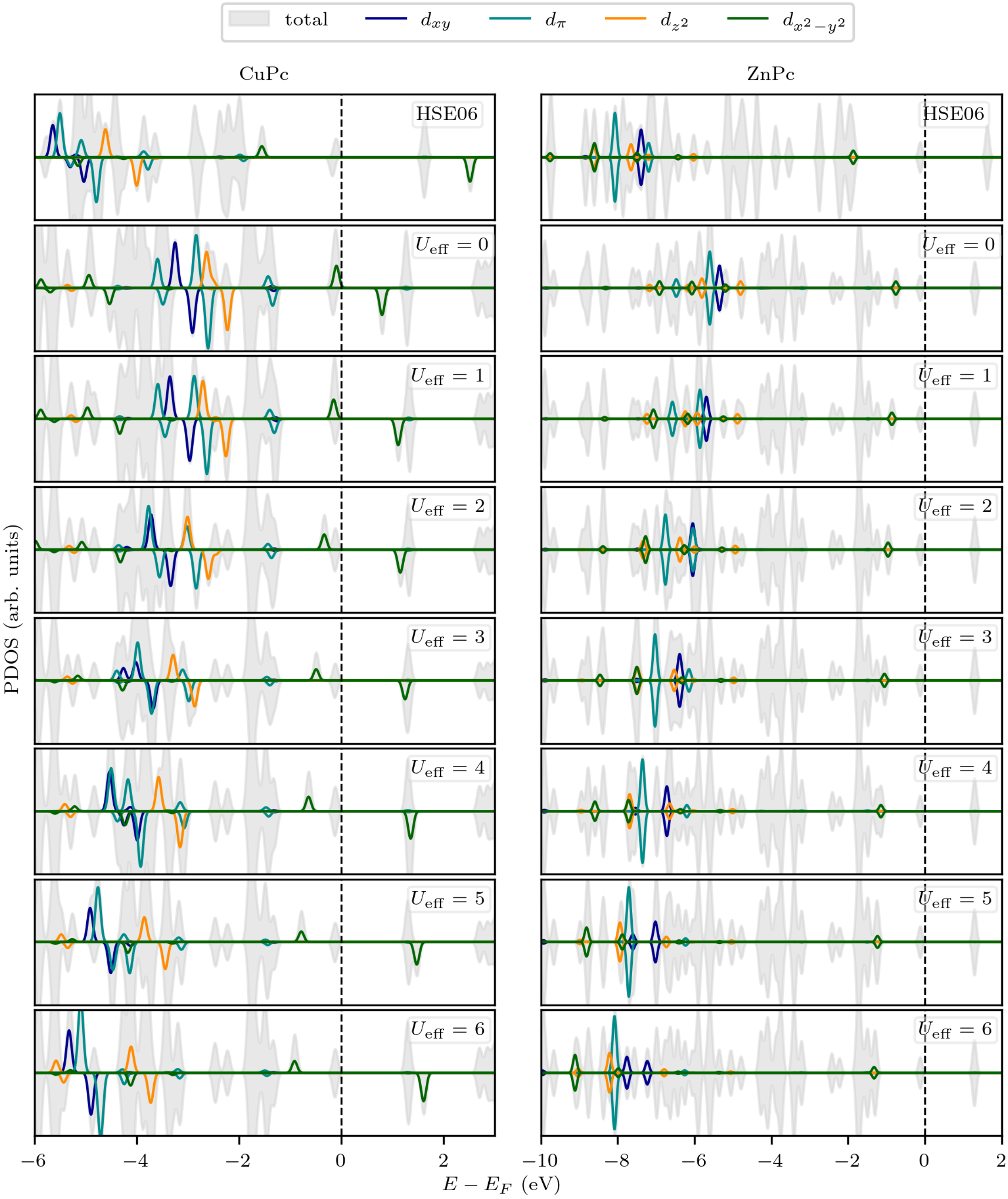

Figure 3.8: PDOS of CuPc (left) and ZnPc (right) calculated with HSE06 [11] (top) and GGA+U [15, 16]. U_eff was varied from 1 eV to 6 eV and $U_\mathrm{eff}=0$ is the standard GGA-PBE calculation [22].

We define the mean absolute deviations $\Delta E(U_{\text{eff}})$ between the orbital energies of the transition metal d-states of the GGA+U and HSE06 calculations as

$$\Delta E(U_{\text{eff}}) = \frac{1}{N} \sum_{\sigma} \sum_{i} |E^{\text{HSE06}}_{\sigma,d_i}(U_{\text{eff}}) - E^{\text{GGA}+U}_{\sigma,d_i}(U_{\text{eff}})|, \tag{3.2}$$

where N is the total number of the orbitals d_i in the spin-down and spin-up channel. Each $E_{\sigma,d_i}(U_{\text{eff}})$ is determined at which the respective PDOS has its maximum.

The mean absolute deviations $\Delta E(U_{\text{eff}})$ get continuously smaller with increasing U_{eff} up to 6 eV for systems with total spin moments of S = 1/2 and S = 0, as shown in Figure 3.9. This statement is only partially true for MnPc with S = 3/2, where at 6 eV the position of the metal d-states shift back to higher energies. Finally, for FePc, the situation is different because no U_{eff} value leads to a satisfying agreement with HSE06 when considering the orbital position and ordering. This could stem from the delocalization of the metal d-states and a consequent large hybridization with the ligand states.

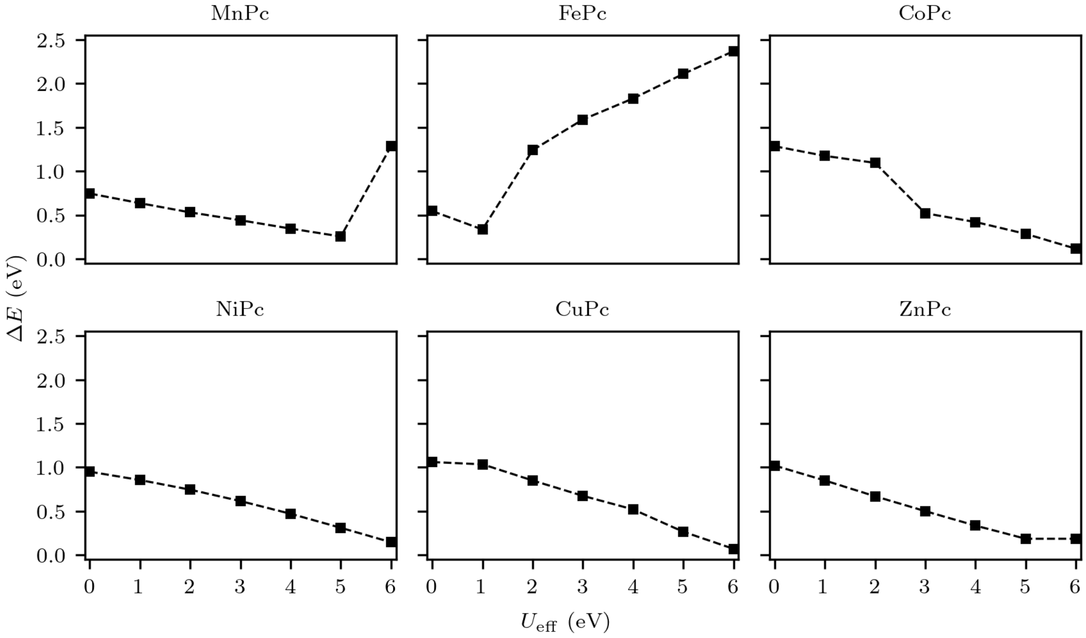

Figure 3.9: Mean absolute deviations ΔE between the orbital energies of the GGA+U [15, 16] and HSE06 [11] calculations for TMPc according to Equation 3.2.

Last, the following Figure 3.10 shows the deviations in the total magnetic moments μ of the entire unit cell and the magnetic moment that is localized on the transition metal μ(TM) between the GGA+U and HSE06 calculations ($\Delta\mu = \mu^{\text{GGA}+U} - \mu^{\text{HSE06}}$) as a function of U_{eff}. For MnPc, the total magnetic moment first stays constant with U_{eff} until it changes at $U_{\text{eff}} = 6$ eV to 5 μ_{B} (high spin state) since, here, the $d_{x^2-y^2}$-up state is occupied and localized at the HOMO (Fig. 3.6). The magnetic moment on

Mn increases continuously with increasing U_{eff} as less contributions are localized on the neighboring N atoms. The GGA+U calculation with $U_{\text{eff}} = 2$ eV is the most similar to the HSE06 calculation, regarding the magnetic moments. For FePc, $\mu^{\text{GGA}+U}$(Fe) has a larger contribution to the total magnetic moment in contrast to μ^{HSE06}(Fe) in the HSE06 calculation. At $U_{\text{eff}} = 3$ eV, there is a change in the magnetic moments which probably stems from the sensitivity of the system to the initialization of the magnetic moment. The other TMPcs only show small deviations between the GGA+U and HSE06. For CoPc and CuPc, there is a small increase in the magnetic moments with U_{eff}, here, $\mu^{\text{GGA}+U}$(Cu) is 0.15-0.02 μ_B smaller compared to the 0.66 μ_B of the HSE06 calculation. For the non-magnetic systems, NiPc and ZnPc, the magnetic moments stay constant at 0 μ_B.

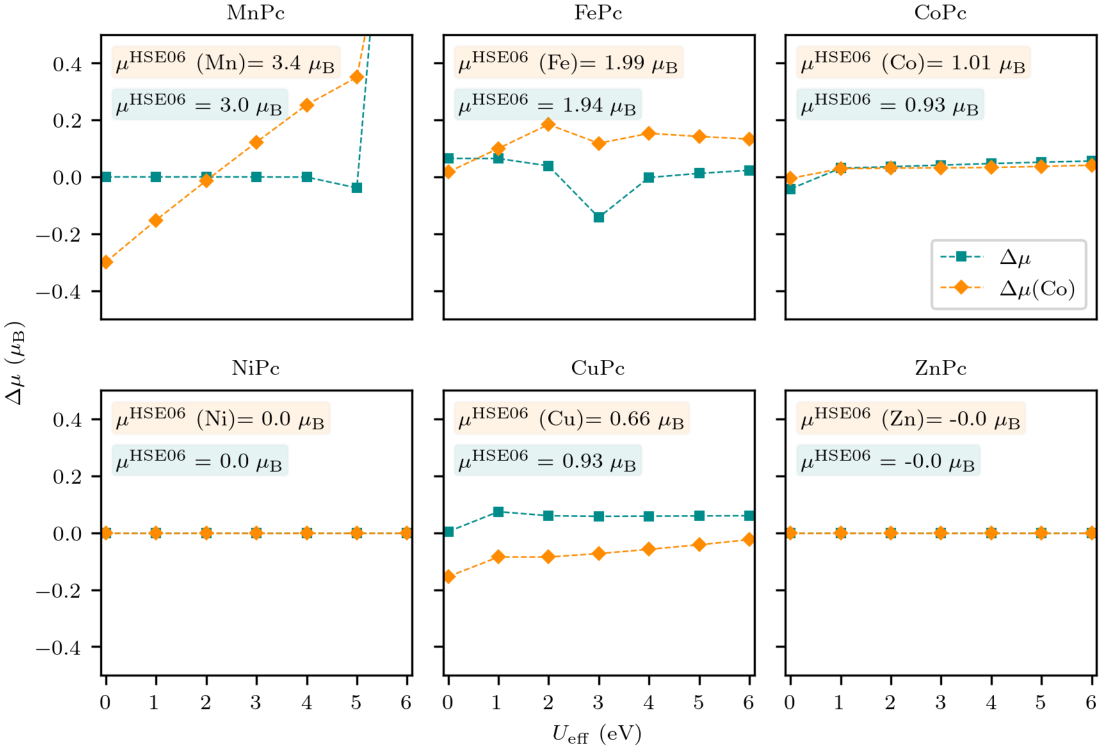

Figure 3.10: Deviations in the magnetic moments $\Delta\mu$ of TMPc between GGA+U and HSE06 as a function of U_{eff}.

3.3 Porphine

In this section, we focus on TMP and as done in Section 3.2 for TMPc, compare results obtained with the hybrid functional HSE06 [11] and PBEh [12–14] to the GGA+U [15, 16] calculations in terms of the orbital ordering, the HOMO-LUMO gaps and magnetic moments. Again, we project the DOS (Eq. 3.1) onto the d-orbitals of the transition metal, in particular, onto the d_{xy} (blue), d_π (cyan), d_{z^2} (orange) and $d_{x^2-y^2}$ (green) orbitals. The total DOS is indicated by the grey areas in all following figures.

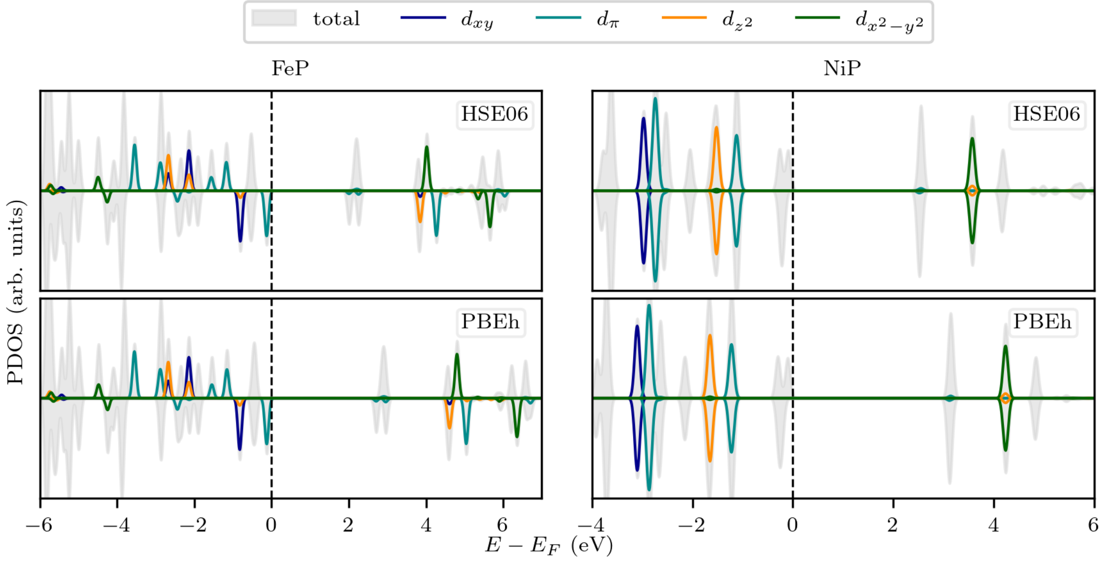

Figure 3.11: PDOS of FeP (left) and NiP (right) calculated with HSE06 [11] and PBEh [12–14].

First, we discuss the differences in the HSE06 [11] and PBEh [12–14] calculations by analyzing the total DOS and PDOS of the FeP and NiP which are plotted, as an example, in Figure 3.11, left and right panel, respectively. As observed for TMPc, the orbital ordering is not affected by the choice of the hybrid functional. The HOMO-LUMO gap calculated with PBEh is by 0.6-0.7 eV larger compared to HSE06 for all TMPs (see Fig. 3.12) since the unoccupied states are located at higher energies.

To analyze the influence of the U_{eff} value onto the orbital ordering and occupation of the d-states of the considered TMPs, we compare the GGA+U to the HSE06 calculations. The plots of the PDOS in Figures 3.13-3.15 follow the orbital color scheme as used in Figure 3.11. In general, TMP follows the same electron filling scheme as TMPc (see Fig. 3.4). There are some deviations which are noted in the analysis of the PDOS below.

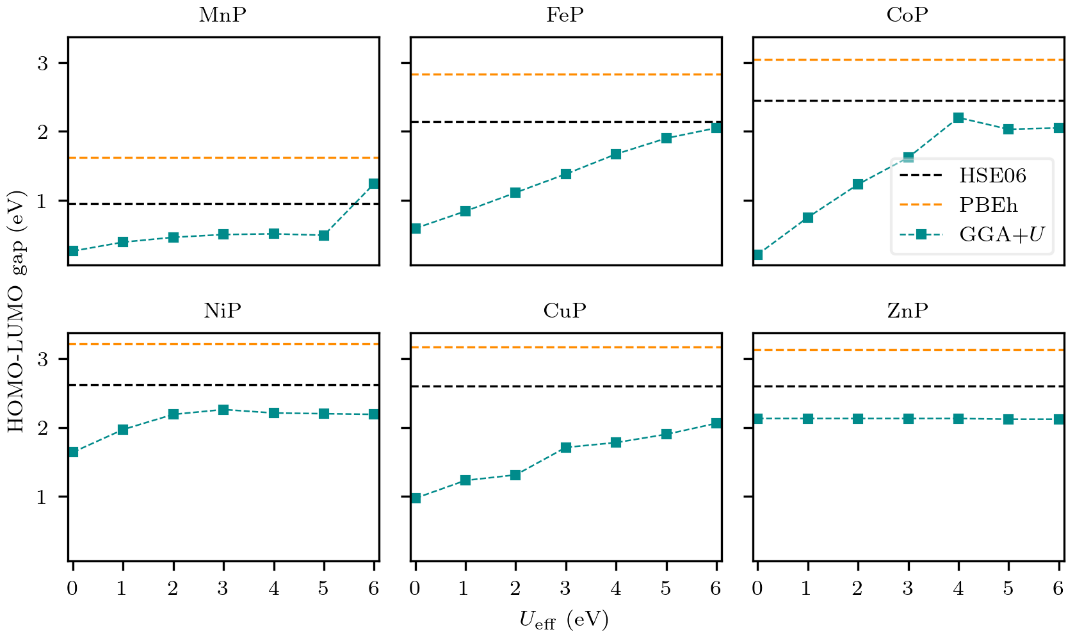

Figure 3.12: HOMO-LUMO gaps of TMP as a function of U_{eff}. $U_{\text{eff}} = 0$ is the standard GGA-PBE calculation [22] and the HSE06 [11] and PBEh [12–14] calculations are indicated by the dashed lines.

As for TMPc, we start the analysis with MnP displayed in the left column of Figure 3.13. Here, also the intermediate spin state with a total spin moment of S = 3/2 is the ground state and the d_{xy}-down state is unoccupied in the HSE06 calculation (Fig. 3.13, topmost left panel). Hybridization with the ligand states leads to additional peaks of the metal d-states. By comparing the HSE06 to the GGA+U calculations, we observe a similar behavior to MnPc, where for $U_{\text{eff}} < 6$, the occupied states shift to lower energies with increasing U_{eff}. The HOMO and LUMO are defined by d_{π}-down states for $U_{\text{eff}} < 6$ eV but the contribution to the LUMO decreases with increasing U_{eff}. For $U_{\text{eff}} = 6$ eV, the orbital energies and occupation are different since the d_{z^2}-down state is occupied and contributes to the HOMO. The HOMO-LUMO gap stays the same for $U_{\text{eff}} < 6$ eV since the d_{π}-down states do not shift in energy. It then changes for $U_{\text{eff}} = 6$ eV, where the LUMO is only defined by ligand states at around 1 eV above the Fermi energy (Fig. 3.12). The most suitable choice is $U_{\text{eff}} = 5$ eV regarding the energies of the orbitals. However, when considering the orbital ordering of the metal d-states, the calculation with $U_{\text{eff}} = 4$ eV is closer to the HSE06 calculation.

For FeP, the intermediate spin state is the ground state with a total spin moment of S = 1. This was also reported in Reference [66], where the total energy of the different spin states was calculated with the hybrid functional B3LYP/6-31G* [67–69]. The occupation of the orbitals is fully captured in all calculations (Fig. 3.13, right panel). The most similar results to HSE06 are achieved with $U_{\text{eff}} = 4$ eV, however, the deviations of all GGA+U calculations are small for FeP compared to the other TMPs (Fig. 3.16).

The HOMO-LUMO gap increases up to $U_{\mathrm{eff}} = 4$ eV, as the unoccupied d_π-down state shifts to higher energies, and for larger U_{eff}, it is only defined by ligand states (Fig. 3.12).

For CoP, the ground state is the intermediate spin state, as for CoPc, and it has a total spin moment of S = 1/2. In the hybrid functional calculation, shown in Figure 3.14, topmost left panel, the d_{z^2}-down state is occupied and instead, the d_π-down state is unoccupied, in contrast to the orbital occupation in CoPc (Fig. 3.7, left panel). The GGA+U calculations follow the same occupation scheme. As the occupied and unoccupied states shift to lower and higher energies with increasing U_{eff}, respectively, $U_{\mathrm{eff}} = 5$ eV has the least deviation to HSE06. Therefore, also the HOMO-LUMO gap increases until it is only defined by ligand states at $U_{\mathrm{eff}} = 5$ eV (Fig. 3.12).

As NiPc, NiP is non-magnetic and Figure 3.14 (right panel) shows that $U_{\mathrm{eff}} = 6$ eV gives the most similar result to the HSE06 calculation. For $U_{\mathrm{eff}} = 1$ eV and 2 eV the energies of the d_{z^2}-up and -down states are slightly shifted relative to each other presumably due to hybridization with ligand states. The HOMO-LUMO gap is defined by the d-orbitals for small U_{eff} values but for $U_{\mathrm{eff}} \geq 4$ eV the HOMO and LUMO are localized on ligand states (Fig. 3.12).

CuP has a total spin moment of S = 1/2, as CuPc, with $d_{x^2-y^2}$-down being unoccupied. The least deviations are achieved with $U_{\mathrm{eff}} = 5$ eV (Fig. 3.16), even though $U_{\mathrm{eff}} = 6$ eV would also be a suitable choice (Fig. 3.15, left panel). However, here, the maximum of the d_{xy}-down state is at lower energies hence the larger mean absolute deviation ΔE. The HOMO-LUMO gap increases with increasing U_{eff} as the $d_{x^2-y^2}$-down state shifts to higher energies.

Finally, ZnP is non-magnetic in the ground state. Here, all metal d-orbitals are fully occupied which is captured by all calculations. The description of the orbital energies also gets closer to the HSE06 with increasing U_{eff} (Fig 3.15, right panel), and the HOMO-LUMO gap is only defined by ligand states (Fig. 3.12). With increasing U_{eff}, the d_{z^2} state shows a second peak, more than 1.5 eV below the first peak which is not present in the hybrid calculation. Therefore, the deviations are the smallest for $U_{\mathrm{eff}} = 5$ eV where the intensity of the second peak is not as high.

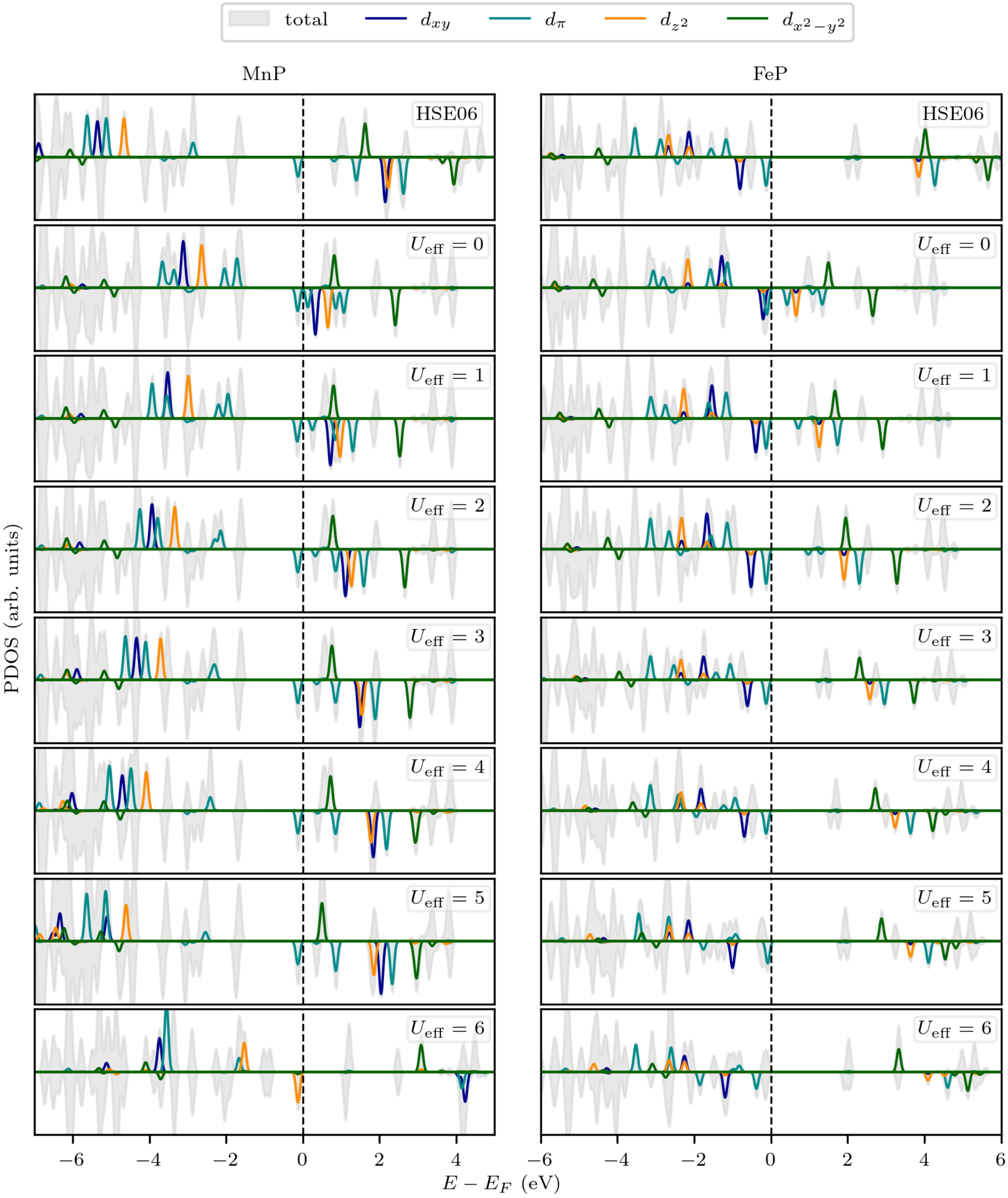

Figure 3.13: PDOS of MnP (left) and FeP (right) calculated with HSE06 [11] (top) and GGA+U [15, 16]. U_eff was varied from 1 eV to 6 eV and $U_\text{eff} = 0$ is the standard GGA-PBE calculation [22].

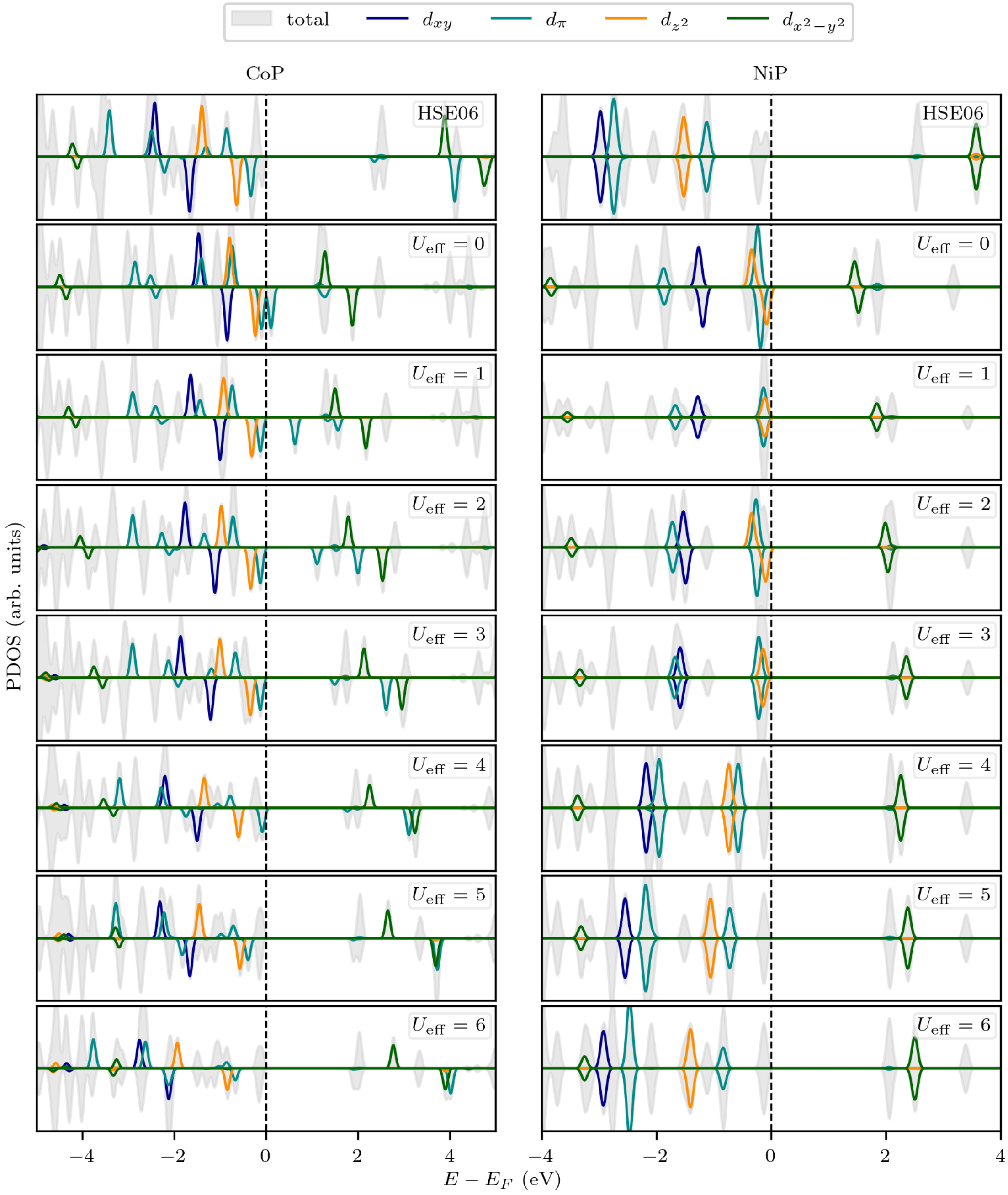

Figure 3.14: PDOS of CoP (left) and NiP (right) calculated with HSE06 [11] (top) and GGA+U [15, 16]. U_{eff} was varied from 1 eV to 6 eV and $U_{\text{eff}} = 0$ is the standard GGA-PBE calculation [22].

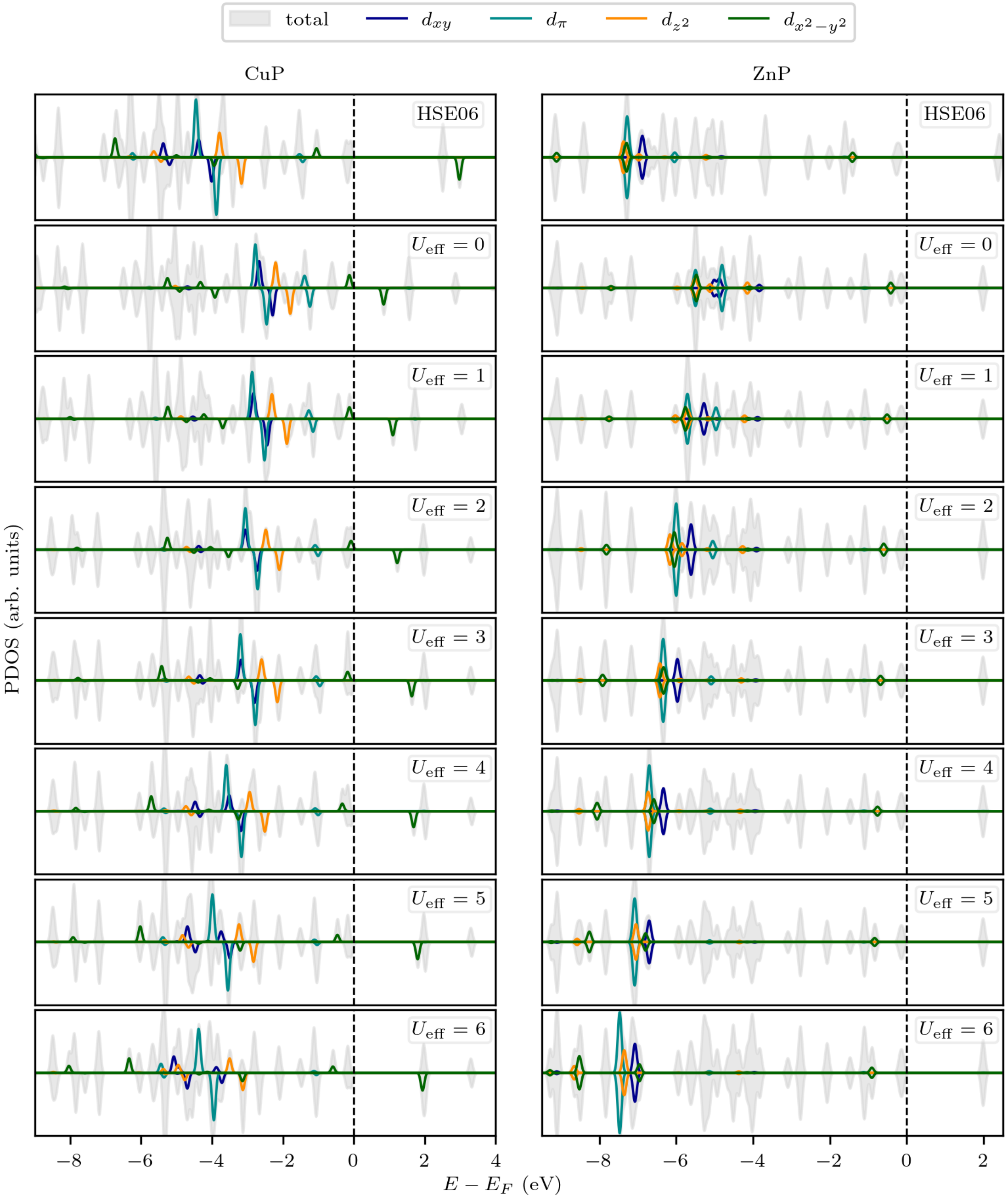

Figure 3.15: PDOS of CuP (left) and ZnP (right) calculated with HSE06 [11] (top) and GGA+U [15, 16]. U_eff was varied from 1 eV to 6 eV and $U_\mathrm{eff} = 0$ is the standard GGA-PBE calculation [22].

As for TMPc, the mean absolute deviations ΔE get continuously smaller with increasing U_eff for systems with total spin moments of S = 0 and S = 1/2, as shown in Figure 3.16. Here, the description of the metal d-states of NiP could probably be improved by increasing U_{eff} further. For CoP, CuP and ZnP, $U_{\text{eff}} = 5$ eV is the optimal choice regarding the energies of the orbitals. For FeP, due to the strong delocalization of the metal d-orbitals, there are multiple peaks corresponding to a d_i-state, therefore, increasing the U_{eff} value does not have the same influence on the orbitals as for the other TMPs. However, the deviations are very small. For MnP, the description of the metal d-states follows the same trend as for CoP, CuP, up to $U_{\text{eff}} = 5$ eV but at 6 eV the energies of the orbitals change drastically which makes the description worse than with the standard GGA-PBE functional.

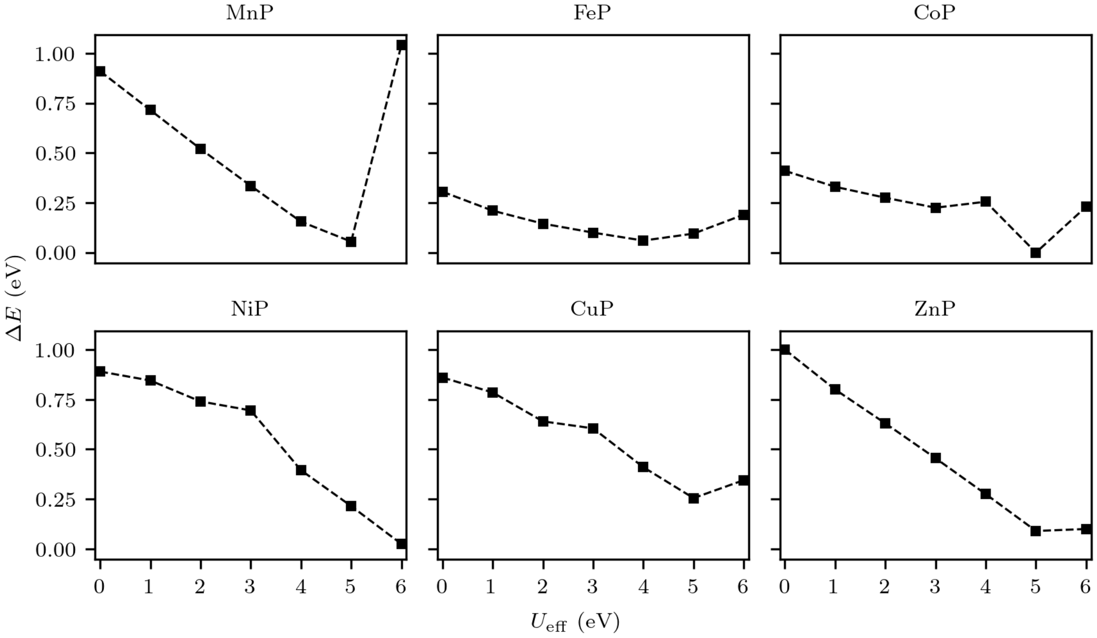

Figure 3.16: Mean absolute deviations ΔE between the orbital energies of the GGA+U [15, 16] and HSE06 [11] calculations for TMP according to Equation 3.2.

Last, the deviations in the magnetic moments, μ and μ(TM), for TMP as a function of U_{eff} are calculated as for TMPc (Section 3.2) and plotted in Figure 3.17. For MnP, the total magnetic moment stays constant throughout all calculations, only $\mu^{\text{GGA}+U}$(Mn), first, increases continuously up to $U_{\text{eff}} = 5$ eV as less contribution is localized on the N and C atoms. At $U_{\text{eff}} = 6$ eV, $\mu^{\text{GGA}+U}$(Mn) decreases drastically since the C atoms contribute more to the total magnetic moment. This radical change also shows in the projected DOS (Fig. 3.13, lower left panel) as discussed above. For FeP, $\mu^{\text{GGA}+U}$(Fe) is slightly larger compared to μ^{HSE06}(Fe) throughout all GGA+U calculations. The jump at $U_{\text{eff}} = 5$ eV may also come from the sensitivity to the initial magnetic moment, as observed for FePc (Fig. 3.10). For CoP, $\mu^{\text{GGA}+U}$ is by 0.12-0.21 μ_{B} smaller than μ^{HSE06} but $\mu^{\text{GGA}+U}$(Co) slightly larger, therefore, more contribution lies on the transition metal in the GGA+U calculations. For NiP, the HSE06 calculation results in a small non-zero magnetic moment of -0.11 μ_{B} and the GGA+U calculations give a total magnetic moment closer to zero. However, the magnetic moment on the transition metal is very similar and close to zero in all calculations. In contrast to CoP, CuP $\mu^{\mathrm{GGA}+U}$ is by 0.11-0.24 μ_B larger than the 0.89 μ_B of the HSE06 calculation and $\mu^{\mathrm{GGA}+U}$(Co) by 0.12 μ_B to 0.02 μ_B smaller. Hence, for $U_\mathrm{eff} \leq 2$ eV, the GGA+U calculations give a total magnetic moment slightly smaller than 1 μ_B and for $U_\mathrm{eff} > 2$ eV, larger than 1 μ_B. For ZnP, on the one hand, the magnetic moment on the transition metal is exactly zero for all calculations. On the other hand, all GGA+U calculations give a non-magnetic solution, whereas, the HSE06 calculation results in a total magnetic moment of -0.06 μ_B due to contributions on the C and N atoms.

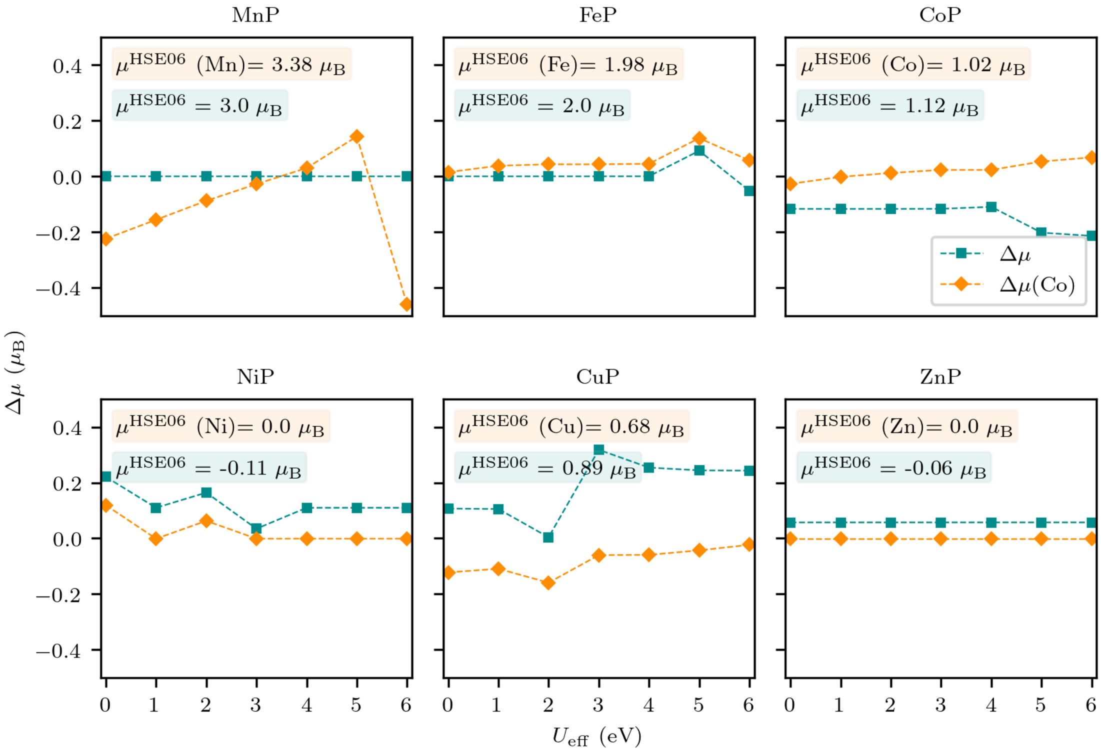

Figure 3.17: Deviations in the magnetic moments $\Delta\mu$ of TMP between GGA+U and HSE06 as a function of U_eff.

In conclusion, it is important to notice that spin-polarized calculations are very sensitive to the initial magnetic moment, especially when the system is magnetic. It would require extensive testing of various initial magnetic moments for each TMC which would exceed the scope of this chapter. When comparing the non-magnetic TMPcs to the TMPs (TM = Zn, Ni), an U_eff value of 6 eV or even 7 eV, as found for NiPc by Brumboiu et al. [17], is a suitable choice since the energies of the orbitals improve with increasing U_eff and the magnetic moments stayed constant throughout all GGA+U calculations. For MnPc and MnP, an U_eff value below 6 eV should be chosen. Here, the orbital description is best captured with $U_\mathrm{eff} = 5$ eV but the magnetic moments with $U_\mathrm{eff} = 2$ eV and $U_{\mathrm{eff}} = 3$ eV for MnPc and MnP, respectively. For FePc and FeP, an U_{eff} value of 1 eV and 4 eV, respectively, should be chosen since both, the magnetic moments and the orbital energies, show the least deviations. The TMPcs and TMPs with a total spin moment of S = 1/2, are adequately described with an U_{eff} value of 6 eV and 5 eV, respectively. However, notice that the magnetic moments of these TMPs deviate from the HSE06 calculation. In summary, it is not beneficial to adopt suitable U_{eff} value of one type of TMC another. It is advisable to compare obtained results to experimental data, as, for example, was done for the vibrational spectra of TMPc in the study by Brumboiu et al. [17].

4 Peritetracene and bitetracene on Cu(111)

4.1 Motivation

In organic electronics, nanographenes with zigzag edges have gained increasing attention due to their interesting electronic and also magnetic properties [18, 19]. Peritetracene (peri4A, $C_{36}H_{18}$), a molecule consisting of two tetracene (4A) rows fused together (see Figure 4.1 (c)), has been discussed as a building block of these nanographenes [20]. Recently, it has been demonstrated that peri4A can be synthesized on a surface by using 1,1'-bitetracene (bi4A, $C_{36}H_{22}$) as a precursor molecule. Experimentally, bi4A, depicted in Figure 4.1 (a) and (b), with a tetrahedral angle of around 70° in the gas phase, is deposited on the Cu(111) surface and after a subsequent heat treatment of 250 °C for 30 minutes, islands of well-ordered monolayers of flat-lying peri4A are formed between regions of unordered peri4A. These resulting monolayers were synthesized and investigated at the University of Tübingen by scanning tunneling microscopy (STM), ultraviolet photoelectron spectroscopy (UPS) and low-energy electron diffraction (LEED) [70]. From the STM it has been observed that peri4A lies flat on the surface.

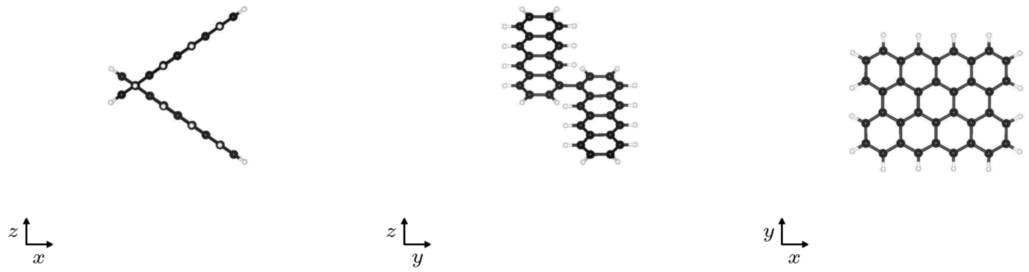

Figure 4.1: Bi4A ($C_{36}H_{22}$) and peri4A ($C_{36}H_{18}$) in the gas phase. (a) and (b) show bi4A in two different side views. (c) shows peri4A in the top view.

In this work, both molecules are analyzed by DFT using the VASP 5.4.4 code. As the exchange correlation functional, the GGA-PBE [22] with the DFT-D3(zero) method of Grimme [23] for empirical dispersion corrections was chosen. The repeated slab approach was used to simulate the interface, as explained in Chapter 2.4.2. Thus, for the peri4A/Cu(111) and bi4A/Cu(111) system a supercell with one molecule on 6 layers of copper was set up. The structure was optimized using damped molecular dynamics, as explained in Section 2.4.3, until the forces were below 0.01 eV/Å. After the geometry optimization of peri4A/Cu(111), the STM images were simulated to confirm the experimental STM using the Tersoff-Haman approximation [25, 26] in constant current mode, explained in the following section 4.2. Further investigations are aiming at the observation of the charge rearrangements upon interface formation in Section 4.4.

4.2 Structure optimization of peri4A on Cu(111)

We start the analysis with peri4A/Cu(111) since the molecule is already flat in the gas phase and we expected a similar adsorption behavior to tetracene [71]. In a first step, a supercell, that is repeated in all three dimensions, needs to be set up. The substrate was simulated by 6 layers of Cu using the experimental lattice parameter of 3.61 Å for bulk Cu. To ensure a sufficiently large vacuum gap, the height of the supercell was chosen to be 36.4 Å which results in a thickness of the vacuum layer of approximately 22 Å. For the overlayer structure, we set up four slightly different commensurate surface unit cells, similar to the surface unit cell obtained from the LEED experiment, all of which containing one molecule. These are defined by the epitaxial matrix P which transforms the primitive unit cell vectors of the Cu(111) surface unit cell $\boldsymbol{a}_1$, $\boldsymbol{a}_2$ into the surface unit cell vectors $\boldsymbol{b}_1$, $\boldsymbol{b}_2$, according to $\boldsymbol{b} = P\boldsymbol{a}$.

$$\begin{pmatrix} \boldsymbol{b}_1 \\ \boldsymbol{b}_2 \end{pmatrix} = \begin{pmatrix} \alpha & \beta \\ \gamma & \delta \end{pmatrix} \begin{pmatrix} \boldsymbol{a}_1 \\ \boldsymbol{a}_2 \end{pmatrix} \tag{4.1}$$

Here, $\boldsymbol{a}_1$ and $\boldsymbol{a}_2$ are the primitive unit cell vectors of Cu and $\boldsymbol{b}_1$ and $\boldsymbol{b}_2$ are the surface unit cell vectors of the system, both expressed in Cartesian coordinates.

Table 4.1 Epitaxial matrix P, length of surface unit cell vectors $b_1 = |\boldsymbol{b}_1|$, $b_2 = |\boldsymbol{b}_2|$, enclosing angle α and the surface area A for the four overlayer structures for peri4A/Cu(111) considered in this work.

	P	b_1 (Å)	b_2 (Å)	α (°)	A (Å^2)
(a)	$\begin{pmatrix} 7 & -1 \\ -3 & 6 \end{pmatrix}$	16.7	13.3	97.6	213.7
(b)	$\begin{pmatrix} 6 & -1 \\ -3 & 5 \end{pmatrix}$	14.2	11.1	105.5	145.1
(c)	$\begin{pmatrix} 6 & -2 \\ -2 & 5 \end{pmatrix}$	13.5	11.1	102.5	140.6
(d)	$\begin{pmatrix} 6 & -1 \\ -4 & 5 \end{pmatrix}$	14.2	11.7	118.1	137.3

For each of the four surface unit cells considered in this work, a geometry relaxation was performed until the forces were below 0.01 eV/Å, as explained in Section 2.4.3, using four different adsorption sites as initial geometry. These are the top, bridge, hollow-fcc and hollow-hcp site (see Fig. 4.2). The zigzag direction of peri4A orients along the $[\bar{1}10]$ direction for surface unit cells (a) and (b). For surface unit cell (c), it is rotated by around 14° and for surface unit cell (d) by around 1° with respect to the $[\bar{1}10]$ direction. For the calculations a Monkhorst-Pack $2 \times 2 \times 1$ k-grid [72], a first-order Methfessel-Paxton smearing of 0.15 eV [65] and 400 eV plane wave cut-off was used.

The adsorption configuration with the lowest total free energy and consequently largest adsorption energy is the most favorable. The adsorption energy is the energy gained by the system when combining the two subsystems, molecule and substrate. For the calculation, there are two approaches: For the first approach, the adsorption energy E_{ads} is calculated by taking the energy of the total system and subtracting the sum of the energies of the separate subsystems E_{mol} and E_{sub} in the gas phase. For the second approach, the separate subsystems are taken in the fixed adsorption geometries instead and noted with tilde $\tilde{E}_{\mathrm{ads}}$. We take the negative due to the convention to speak of the ”largest” instead of the ”lowest” adsorption energy.

$$E_{\mathrm{ads}} = -(E_{\mathrm{total}} - (E_{\mathrm{mol}} + E_{\mathrm{sub}})), \qquad \tilde{E}_{\mathrm{ads}} = -(E_{\mathrm{total}} - (\tilde{E}_{\mathrm{mol}} + \tilde{E}_{\mathrm{sub}})) \tag{4.2}$$

The calculated values for E_{ads} and $\tilde{E}_{\mathrm{ads}}$ are listed in Table 4.2.

Table 4.2 Adsorption energies E_{ads} and $\tilde{E}_{\mathrm{ads}}$ (eV) (Eq. 4.2) for the four adsorption sites of peri4A/Cu(111).

Surface unit cell	(a)		(b)		(c)		(d)	
	E_{ads}	$\tilde{E}_{\mathrm{ads}}$	E_{ads}	$\tilde{E}_{\mathrm{ads}}$	E_{ads}	$\tilde{E}_{\mathrm{ads}}$	E_{ads}	$\tilde{E}_{\mathrm{ads}}$
hollow-hcp	5.23	5.64	5.06	5.37	4.71	5.15	5.19	5.13
hollow-fcc	5.12	5.51	4.98	5.30	4.66	4.95	4.69	4.47
bridge	4.93	5.28	4.92	5.23	4.67	4.90	4.58	4.53
top	4.31	4.41	4.17	4.35	4.65	4.92	4.06	3.80

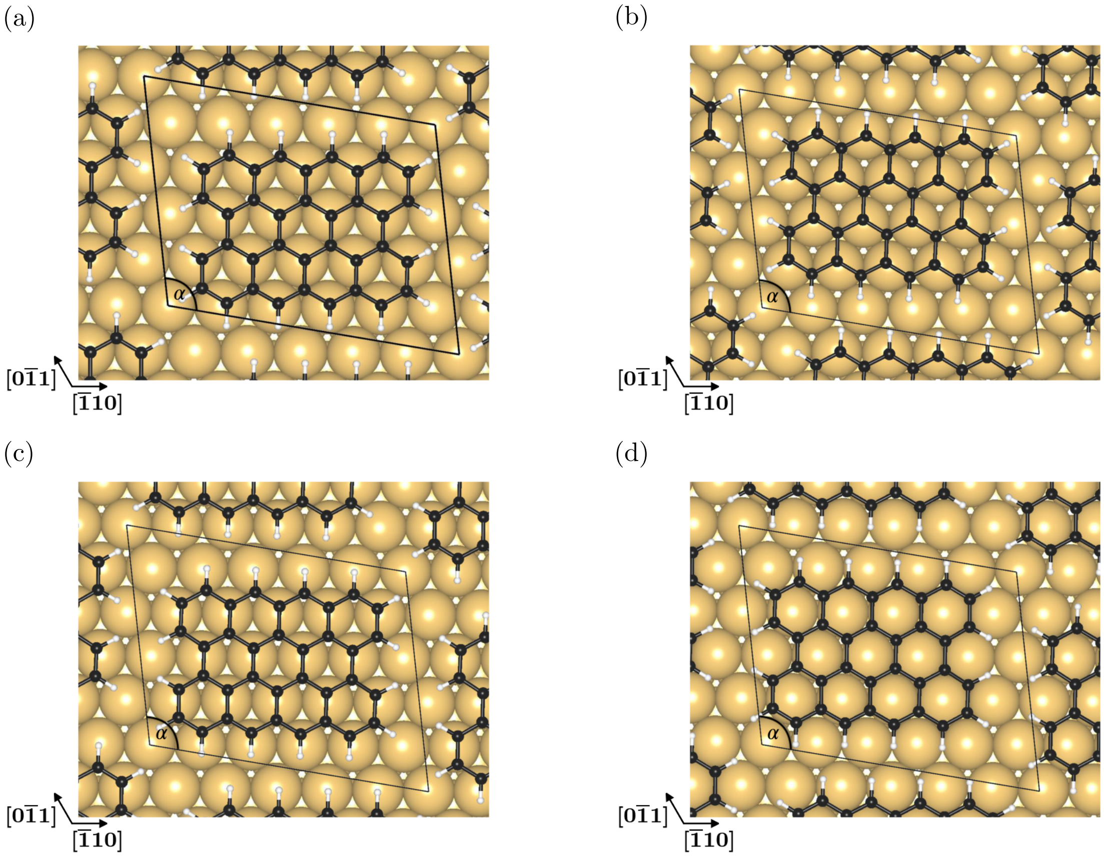

Figure 4.2: Peri4A/Cu(111) in the different adsorption sites. (a) hollow-hcp site, (b) hollow-fcc site, (c) bridge site, (d) top site.

In Figures 4.3 and 4.4 we show peri4A on the hollow-hcp site for the four overlayer structures considered in this thesis in top and side view.

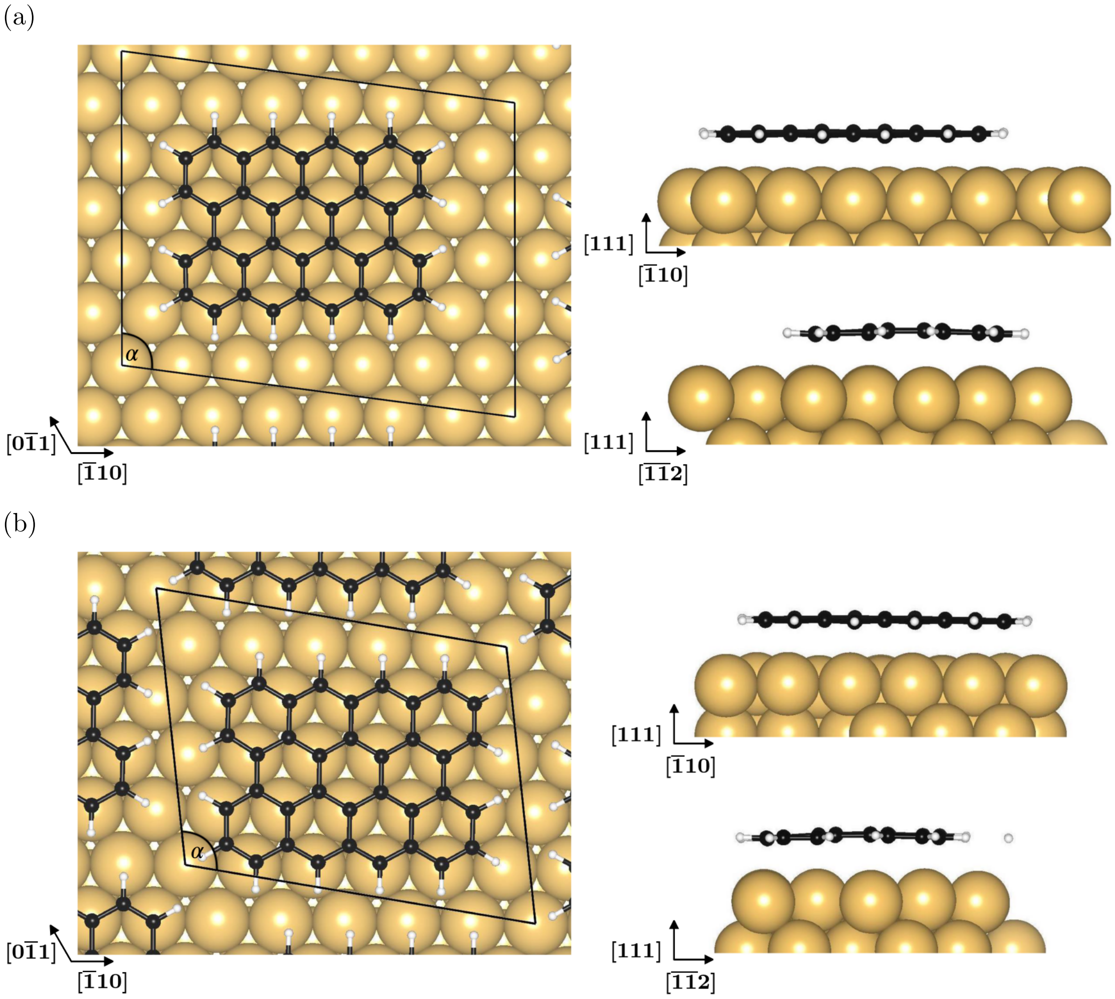

Figure 4.3: Peri4A on Cu(111) in surface unit cells (a) and (b) in top and side view.

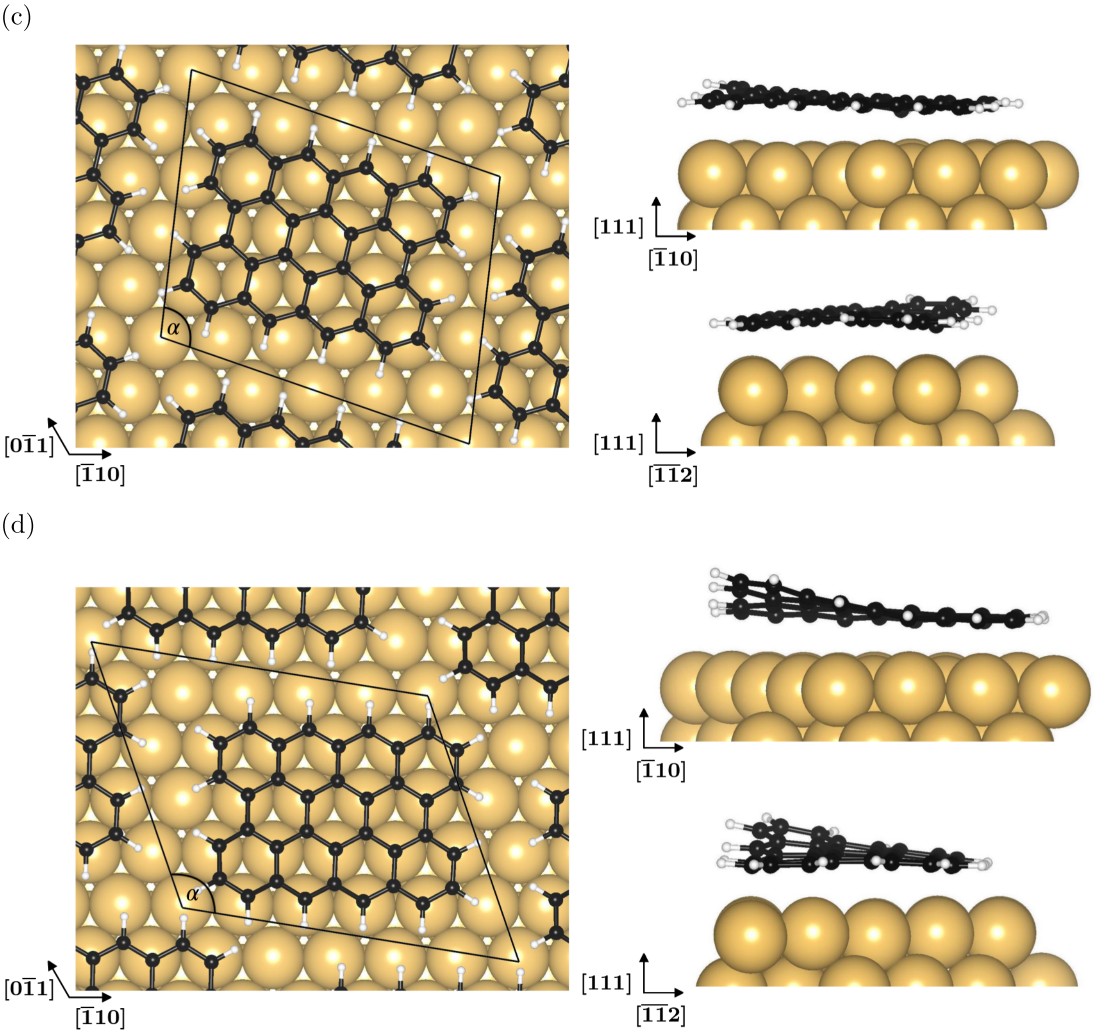

Figure 4.4: Peri4A on Cu(111) in surface unit cells (c) and (d) in top and side view.

The average adsorption distance d_{A}, defined by the average distance of the atom types A in the molecule to the topmost Cu-layer with its standard deviation, and the maximum bending of peri4A, which is determined by the difference between the maximum adsorption distance and the minimum adsorption distance, are listed in Table 4.3 for the considered surface unit cells.

As shown in Table 4.2, for all supercells, the hollow-hcp site is the most favorable among the four configurations. Here, additional calculations were performed where the orientation of the molecule on the hollow-hcp site is slightly changed in order to determine whether the system is in its minimum. The values for the adsorption energies in Table 4.2 only include these already optimized results.

Table 4.3 Average adsorption distance d_A of the atom types A in peri4A to the topmost Cu(111)-substrate layer with its standard deviation and maximum bending, $\Delta d = d_\mathrm{max} - d_\mathrm{min}$, of the C atoms in the considered surface unit cells.

Surface unit cell	(a)	(b)	(c)	(d)
d_C (Å)	2.66 ± 0.06	2.73 ± 0.06	2.84 ± 0.19	2.82 ± 0.36
d_H (Å)	2.64 ± 0.05	2.69 ± 0.05	2.81 ± 0.28	2.89 ± 0.57
Δd (Å)	0.20	0.22	0.83	1.46

To confirm the agreement with the experiment, we simulate the STM images using the Tersoff-Haman approximation [25, 26] and an applied voltage V of -1.0 eV. In this approximation the wave-function of the tip's apex atom is assumed to be of s-wave character with radius R and the tunnelling current I is given by

$$\begin{aligned} I =& 32\pi^3\hbar^{-1}e^2V\phi^2D_t\left(E_F\right)R^2\kappa^{-4}e^{2\kappa R} \\ &\times \sum_v \left|\psi_v\left(\boldsymbol{r}_0\right)\right|^2\delta\left(E_v - E_F\right), \end{aligned} \tag{4.3}$$

where V is the applied voltage, ϕ the work function, D_t the density of states per unit volume of the probe tip, κ the minimum inverse decay length for the wave function in vacuum, $\boldsymbol{r}_0$ the position of the center of the tip and $\sum_v \left|\psi_v\left(\boldsymbol{r}_0\right)\right|^2\delta\left(E_v - E_F\right)$ is the local density of states (LDOS) at the Fermi energy E_F and position $\boldsymbol{r}_0$.

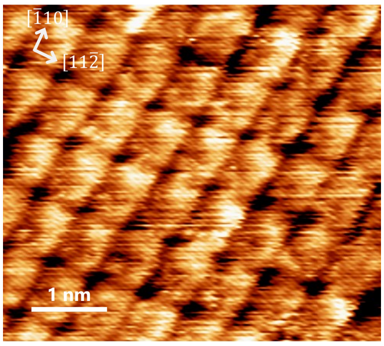

Figure 4.5: Experimental STM of peri4A/Cu(111) ($U = -0.2$ V, $I = 1$ nA). Adapted with permission from Klein et al. [70].

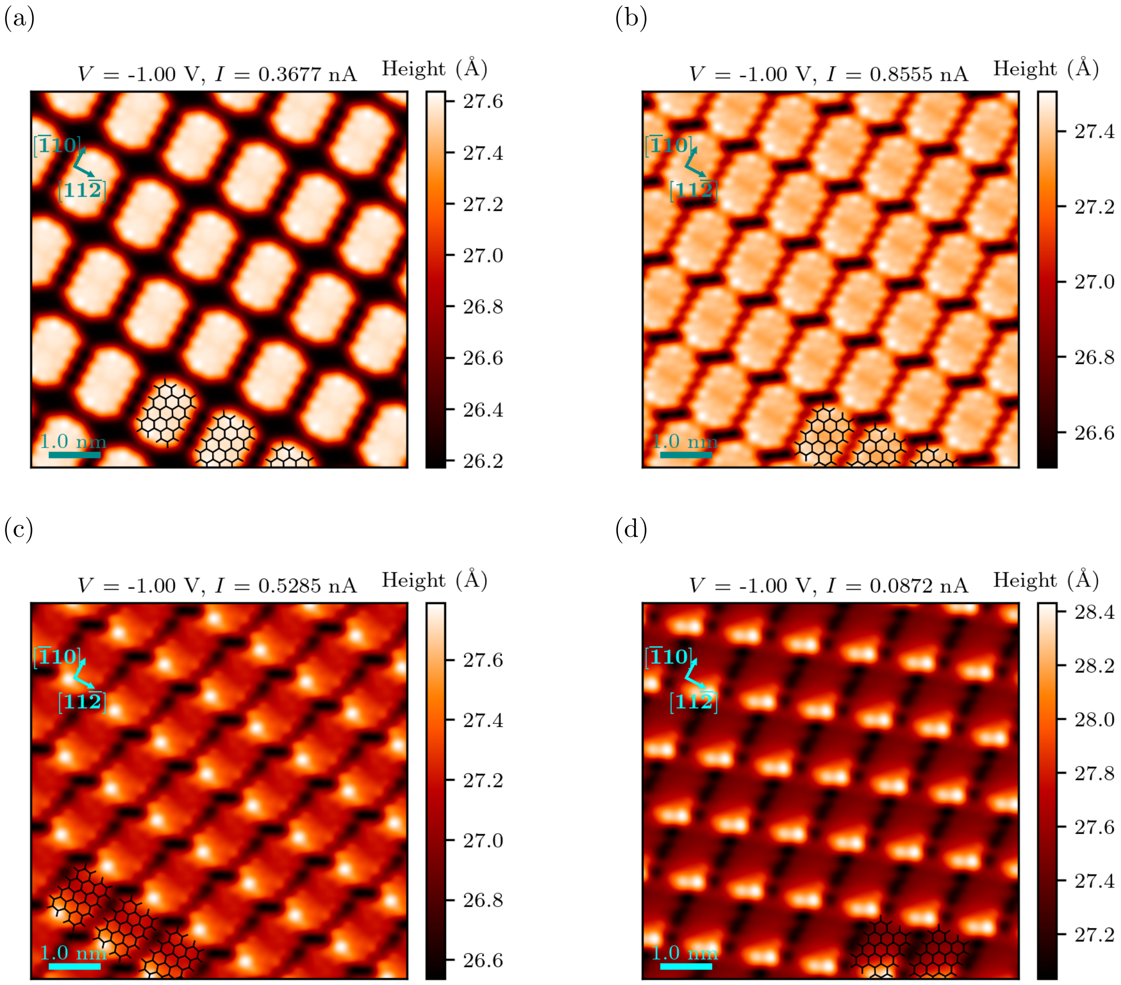

Figure 4.6: STM simulations of peri4A/Cu(111) for the four different surface unit cells defined in Table 4.1.

By comparing the simulated STM images for the different unit cells in Figure 4.6 with the experimental STM image ($U = -0.2$ V, $I = 1$ nA) [70] in Figure 4.5, we see that surface unit cell (b) fits best to the experimental image. The surface unit cell (a) is not suitable because of its large area which does not allow the molecules to interact with each other. Surface unit cells (c) and (d) bring the molecules too close together, which results in a repulsion of the hydrogen atoms and consequent out-of-plane distortions of the molecule which are absent in the experimental STM. This result is corroborated by simulations of the LEED with surface unit cell (b) (Fig. 4.7(b) and (c)). The experimental LEED, shown in Figure 4.7(a), for comparison, was taken after the heat treatment of bi4A [70]. These results confirm that a well-ordered monolayer of flat-lying peri4A is formed after the heat treatment.

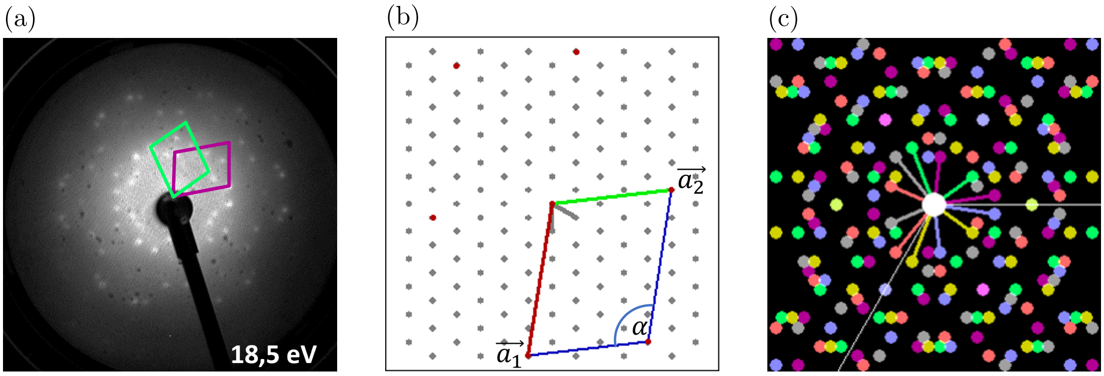

Figure 4.7: (a) Experimental LEED image of peri4A on Cu (111) at a beam energy of 18.5 eV. (b) Simulated lattice with surface unit cell (b) (see Tab. 4.1). (c) Corresponding simulated LEED pattern. Reprinted Figures with permission from Klein et al. [70]. Here, a_1 and a_2 are the surface unit cell vectors noted with $\mathbf{b}_1$ and $\mathbf{b}_2$ in this thesis.

4.3 Structure optimization of bi4A on Cu(111)

For studying the adsorption of the precursor molecule bi4A on Cu(111), for simplicity, the commensurate $\left(\begin{smallmatrix}7 & -1\\ -3 & 6\end{smallmatrix}\right)$ surface unit cell was chosen. The height of the supercell was 36.4 Å to ensure a large vacuum gap of 21 Å. This cell was large enough to enclose one molecule and was therefore appropriate for our purpose. Note, however, that no LEED data for this molecule was available to reconfirm this choice. As for peri4A, geometry relaxations for the four adsorption sites on the Cu(111) surface were performed using a Monkhorst-Pack $2 \times 2 \times 1$ k-grid [72], a first-order Methfessel-Paxton smearing of 0.15 eV [65] and 400 eV plane wave cut-off, as for peri4A/Cu(111). By comparing the adsorption energies of bi4A on the adsorption sites of Cu(111), we find that the optimal adsorption site is the hollow-hcp site, as well. The adsorption energies E_{ads} and $\tilde{E}_{ads}$, according to Equation 4.2, are listed in Table 4.4.

Table 4.4 Adsorption energies E_{ads} and $\tilde{E}_{\mathrm{ads}}$ (Equation 4.2) for the four adsorption sites of bi4A/Cu(111).

Adsorption site	E_{ads} (eV)	$\tilde{E}_{ads}$ (eV)
hollow-hcp	4.29	5.45
hollow-fcc	4.25	5.40
bridge	3.93	4.98
top	3.31	4.13

As shown in Figure 4.1 (left panel), bi4A has a tetrahedral angle of around 70° in the gas phase. Upon adsorption, the molecule is partially planarized due to vdW-interactions with the Cu(111) substrate but the repulsion of the hydrogen atoms hinders the molecule from adsorbing in a completely flat configuration (Fig. 4.8). The adsorption distances of the C atoms d_{C} and the H atoms d_{H} with their standard deviation, defined by the average distance of the atoms to the topmost Cu-layer, are 2.95±0.54 Å and 2.98±0.67 Å, respectively. The maximum bending, defined as $\Delta d = d_{\mathrm{max}} - d_{\mathrm{min}}$, of the C atoms is 1.81 Å.

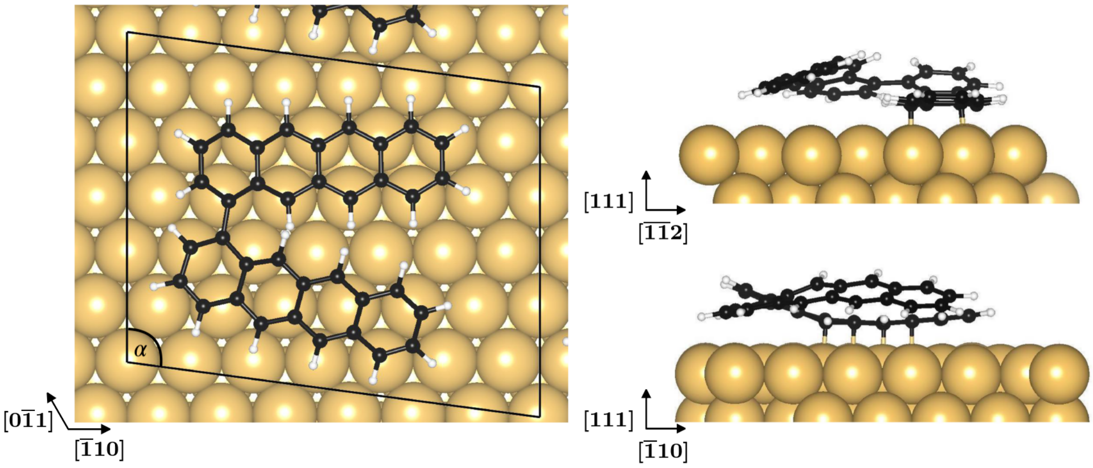

Figure 4.8: Bi4A on Cu(111) in surface unit cells (a) in top and side view.

4.4 Electronic structure of peri4A and bi4A on Cu(111)

The subsequent analysis of the electronic structure has been done by using a denser k-grid of $3 \times 3 \times 1$ for both systems and the $\left(\begin{smallmatrix} 6 & -1 \\ -3 & 5 \end{smallmatrix}\right)$ surface unit cell, denoted with (b), for peri4A/Cu(111). To understand what happens upon interface formation, we can calculate the charge rearrangement. We define the charge density difference $\Delta\rho$ as the difference between the charge density of the full system ρ and the sum of the charge densities of the two subsystems, molecule ρ_{mol} and substrate ρ_{sub}.

$$\Delta\rho = \rho - (\rho_{\mathrm{mol}} + \rho_{\mathrm{sub}}) \tag{4.4}$$

Note that the geometry of both, the molecule and the substrate, has been frozen in the relaxed state of the full system for evaluating ρ_{mol} and ρ_{sub}, respectively. In addition to the three-dimensional quantity $\Delta\rho(x, y, z)$, we also consider the plane-averaged charge density difference by averaging over the xy-plane parallel to the substrate surface. In particular, this allows solving the Poisson equation ($\frac{d^2\Delta V}{dz^2} = \Delta\rho(z)$) to obtain the change in the electrostatic potential ΔV across the interface in z-direction, which determines the bond dipole $\Delta\phi_{\mathrm{bond}}$ between the substrate and the molecule.

The bond dipole can be further separated into two contributions, namely the work function reduction due to Pauli pushback [73] and the work function increase (decrease) due to electron transfer into the molecule (metal) [4]. Depending on which contribution prevails, the work function of the system will be decreased (Pauli pushback dominates), further decreased (charge transfer into the metal) or increased (charge transfer into the molecule dominates). The Pauli pushback occurs since the molecular orbitals overlap with the metal wave functions which pushes the electrons back into the two subsystems due to the Pauli repulsion principle [74]. This pushback effect is larger for the metal substrate since the electrons are more polarizable compared to the electrons of the molecule [4]. The surface dipole reduction, consequently, shifts the electrostatic potential and therefore reduces the work function of the system [4]. Additionally, the metal surface screens the charge from the molecule and therefore reduces the HOMO-LUMO gap [75]. This effect is not captured by DFT with conventional GGA or hybrid functionals but by many body perturbation theory [76]. The GW approximation [77, 78] takes the polarizability of the surface through the screened Coulomb-interaction into account, so the more polarizable the substrate, the smaller the HOMO-LUMO gap of the molecule [76]. Charge transfer into the molecule happens when the LUMO lies below the Fermi energy of the metal, which then induces a dipole. This dipole consequently shifts up the vacuum level, counteracting the pushback effect [79].

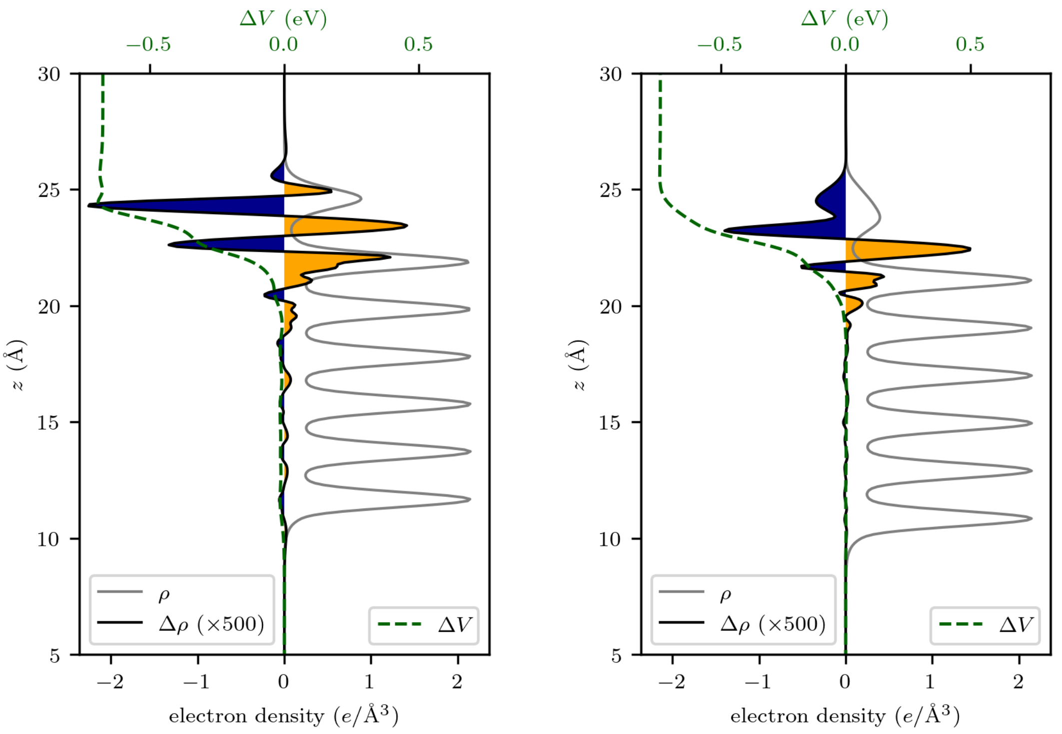

Figure 4.9: Charge rearrangement of peri4A (left) and bi4A (right) on 6 layers Cu(111). The black line denotes the plane-averaged charge density $\Delta\rho\,(\times 500)$, the grey line the charge density ρ of the full system, the dotted green line the change in the electrostatic potential ΔV and the colored areas indicate electron depletion (darkblue) and accumulation (orange).

When comparing the two systems, peri4A/Cu(111) and bi4A/Cu(111), we see that the Pauli pushback dominates over the charge transfer in both systems. However, the bond dipole for bi4A/Cu(111) is slightly larger (Tab. 4.5) so we can assume that there is less charge transfer into the LUMO of the molecule. To visualize the charge density of the LUMO, we calculate the three-dimensional band decomposed charge density with VASP for the molecular orbitals of the isolated molecule in the adsorption geometry by using its converged WAVECAR file. In the INCAR file, `LPARD=.TRUE.` and `LSEPB=.TRUE.` has to be set to calculate the partial decomposed charge density for each band, specified by `IBAND`, separately. The charge density of the LUMO of bi4A in the adsorption geometry without substrate (Fig. 4.10) shows that charge mostly lies on the flat part of the molecule. Thereby, less charge can be transferred into bi4A in contrast to peri4A with a flat adsorption configuration. This also reflects in the charge rearrangements $\Delta\phi$ (Fig 4.9, left panel) which clearly show a polarization within peri4A. The charge rearrangements in bi4A/Cu(111) (Fig. 4.9, right panel) show more charge accumulation at the molecule-substrate interface since, due to the larger surface unit cell and hence less coverage, the charge is pushed back not only into the bulk but also to the regions where the molecule does not cover the substrate. Another reason for the stronger bond dipole can be the smaller adsorption distance of the flat-lying arm of bi4A leading to a larger Pauli pushback. The molecule has a minimum adsorption distance d_{min} of 2.2 Å and maximum adsorption distance d_{max} of 4.0 Å compared to peri4A with $d_{min} = 2.6$ Å and $d_{max} = 2.8$ Å. The bond dipole $\Delta\phi_{\text{bond}}$ is the step of the electrostatic potential ΔV across the molecule.

To quantify the transferred charge, a Bader charge analysis can be performed [80–83]. This analysis takes the converged density from the VASP CHGCAR file and assigns the charge to the individual atoms by defining a two-dimensional surface around the individual atoms where the charge density is a minimum perpendicular to the surface [80]. This is done for the full system and the isolated molecule in the adsorption geometry and by subtracting the charge on the isolated molecule from the charge on the molecule in the full system, we obtain the transferred charge into the molecule. Since the calculations converge quickly, it is a convenient way to roughly quantify the charge transfer. For peri4A/Cu(111), a charge transfer of 1.05 e and for bi4A/Cu(111), 0.78 e was calculated which is reflected in the work function reduction (Tab. 4.5) being larger for bi4A where there is less charge transfer.

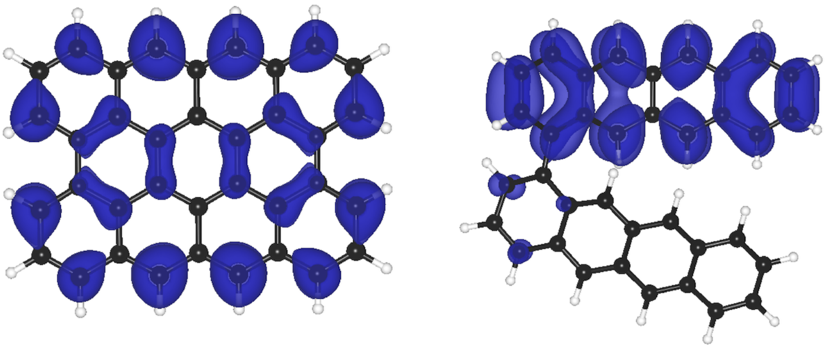

Figure 4.10: Band decomposed charge density of the LUMO of peri4A (left) and bi4A (right) in the adsorption geometry without substrate.

In Table 4.5, the work function of the metal ϕ_0, the system ϕ and the different contributions to the work function change $\Delta\phi$ are listed. These changes arise from the dipoles at the interface. The surface dipole is mainly reduced due to the bonding between molecule and substrate $\Delta\phi_{\text{bond}}$. But there are contributions also arising from rearrangements of the metal atoms $\Delta\phi_{\text{surf}}$ which turn out to be marginal in the present case. Additionally, the molecular dipole $\Delta\phi_{\text{bend}}$ is also comparably small and comes from the geometrical changes in the molecule upon adsorption. Important to notice is that bi4A has a stronger molecular dipole because of the bent arm of the molecule. The difference in ϕ_0 is solely due to numerics.

Table 4.5 Work functions and contributions to the work function change of peri4A and bi4A on Cu(111). ϕ_0: Work function of Cu(111), determined at the bottom of the system, ϕ: Work function of the system, $\Delta\phi_{\mathrm{bond}}$: Bond dipole, the change in the work function due to the charge rearrangement upon adsorption, $\Delta\phi_{\mathrm{bend}}$: Molecular dipole, potential difference below and above the molecule in the adsorption geometry without substrate, $\Delta\phi_{\mathrm{surf}}$: Surface dipole change, the potential difference below and above the copper layers in the final geometry.

	peri4A/Cu(111)	bi4A/Cu(111)
ϕ_0 (eV)	4.75	4.76
ϕ (eV)	4.03	3.94
$\Delta\phi = \phi - \phi_0$ (eV)	-0.72	-0.82
$\Delta\phi_{\mathrm{bond}}$ (eV)	-0.67	-0.74
$\Delta\phi_{\mathrm{bend}}$ (eV)	-0.03	-0.04
$\Delta\phi_{\mathrm{surf}}$ (eV)	-0.01	-0.01

Finally, we also analyze the density of states (DOS), in particular, we can calculate the projected DOS (PDOS) and molecular orbital projected DOS (MOPDOS) [24] to further investigate changes in the electronic structure of the molecule due to the interaction with the substrate. For this, the Kohn-Sham eigenstates of the full system $\psi_{n,\boldsymbol{k}}$ are either projected onto atomic orbitals or molecular orbitals ϕ_i, respectively [24].

$$\rho_{\phi_i}(E) = \frac{1}{N_k} \sum_{n,\boldsymbol{k}} \left|\langle \phi_i \mid \psi_{n,\boldsymbol{k}} \rangle\right|^2 \delta\left(E - \epsilon_{n,\boldsymbol{k}}\right) \tag{4.5}$$

The following graphs in Figure 4.11 and Figure 4.12 show the MOPDOS for the HOMO-1 up to the LUMO+1 and the PDOS of all atomic orbitals of the carbon atoms (C-*tot*) and only the p_z orbitals (C-p_z) from the GGA-PBE and the HSE06 calculations, respectively. In the considered energy range, the main contribution to the PDOS of C-*tot* are the C-p_z orbitals hence they (almost) completely overlap. The molecular orbitals are broadened due to the hybridization with the metal wave functions and the LUMO gets partially filled in both systems. The theoretical results for the PDOS and MOPDOS, obtained with the GGA-PBE functional, (Fig. 4.11) show the LUMO and HOMO peak of peri4A at higher energies compared to the experimental UPS data (upper panel) and the theoretical results for bi4A also mismatch the experimental data (lower panel). These mismatches stem from the shortcomings of the GGA-PBE functional mentioned in Chapter 2, Section 2.3.1. Therefore, the calculations were repeated with the HSE06 functional which is known to give more accurate results for molecules (Fig. 4.12). We observe that the position of the LUMO and HOMO peak of peri4A are now at lower energies, matching the peak in the UPS data (upper panel). The LUMO, HOMO and HOMO-1 peak of bi4A also appear at lower energies. For both systems, the unoccupied orbitals slightly shift to higher energies in the HSE calculations leading to a larger gap between the occupied and unoccupied orbitals compared to the gap in the GGA calculations.

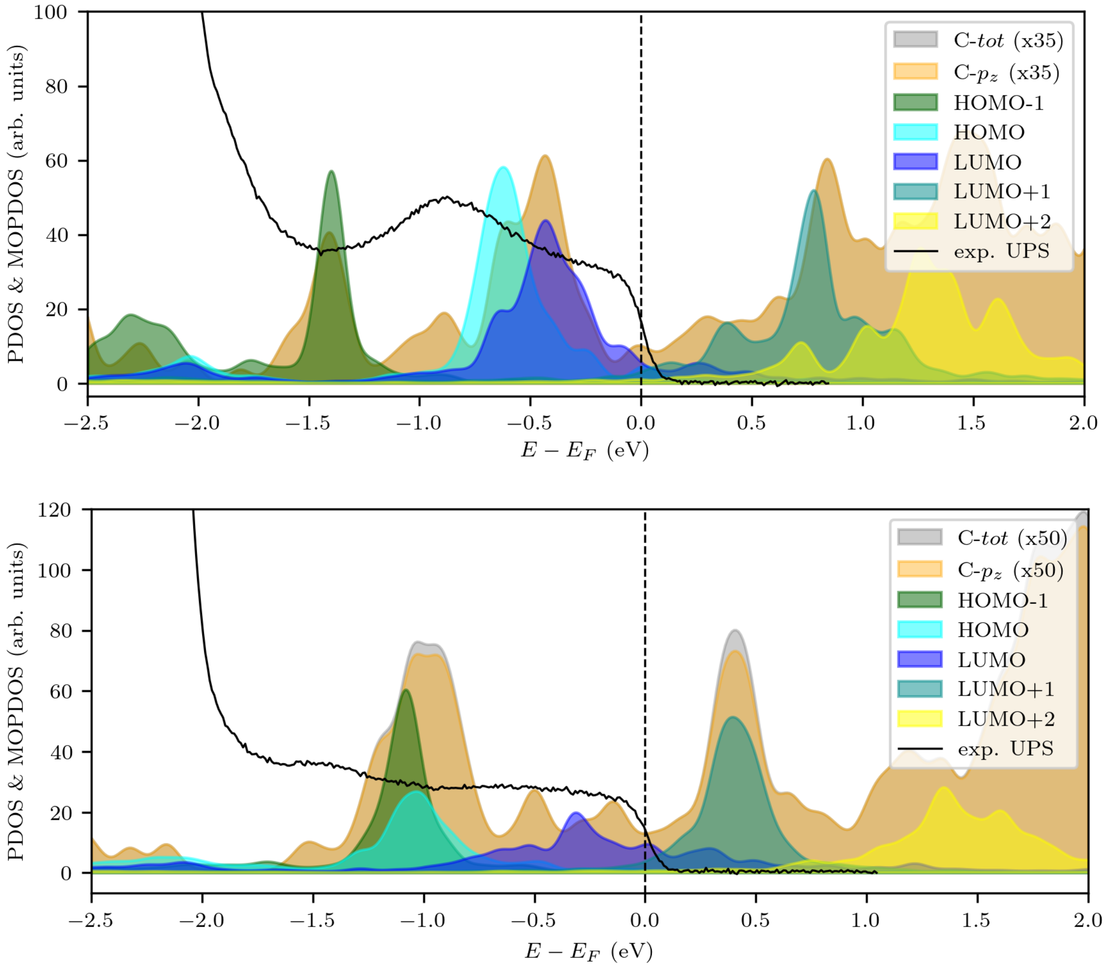

Figure 4.11: MOPDOS for HOMO-1 up to the LUMO+1 and PDOS for C-*tot* and C-p_z of peri4A (top) and bi4A (bottom) on Cu(111) calculated with GGA-PBE [22] compared to the experimental UPS data adapted with permission from Klein et al. [70].

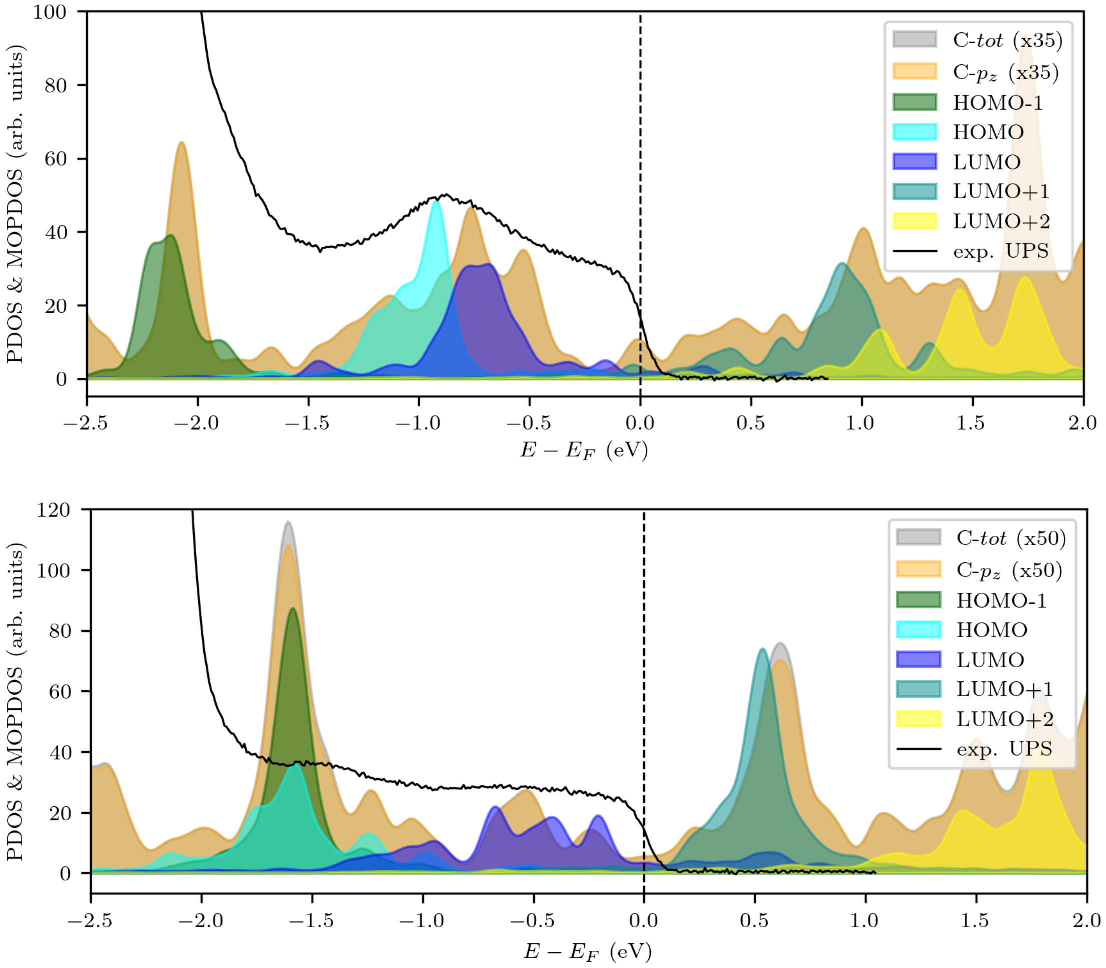

Figure 4.12: MOPDOS for HOMO-1 up to the LUMO+1 and PDOS for C-*tot* and C-p_z of peri4A (top) and bi4A (bottom) on Cu(111) calculated with HSE06 [11] compared to the experimental UPS data adapted with permission from Klein et al. [70].

5 Organic-metal interfaces in static electric fields

5.1 Motivation

In optoelectronics, charge transfer at organic-inorganic interfaces can be driven by strong external electric fields where one oscillation half cycle of a strong low-frequency THz waveform can be approximated by a static electric field. These fields of around 0.1 V/Å will influence the charge rearrangements at the interface and, ultimately, displace the atoms in the molecule. These effects will strongly depend on the internal dipole of the molecule and the substrate-adsorbate interaction in equilibrium. Ideally, a resonant THz electric field induces a vibration of the molecule perpendicular to the substrate, thereby, not only the charge transfer is enhanced or reduced due to the polarization but also due to the smaller or larger adsorption distance.

In this chapter, first the frequency required to induce a collective molecular vibration perpendicular to the substrate plane is investigated on the example of *para*-hexaphenyl (6P, $C_{36}H_{26}$), also known as *para*-sexiphenyl, on the Ag(110) and the Cu(110) substrate. These systems are interesting because of the LUMO position relative to the Fermi level. In 6P/Ag(110), the LUMO of 6P lies close to the Fermi edge [84] which makes it a suitable system for electric field-induced charge transfer into the molecule. In 6P/Cu(110), the LUMO is partially filled due to the stronger interaction with the copper substrate [85]. By step-wise displacing the molecule, already in its adsorption geometry, perpendicular towards and away from the substrate and calculating the energy for the system, the frequency can be determined. These calculations were performed using different vdW-correction schemes to test their performance on the adsorption distance and to choose the most suitable for all further calculations in this chapter since this affects the charge transfer at the interface. Subsequently, to analyze the influence of a static electric field on the interfaces, the two previously mentioned systems and also the molecule perylene-3,4,9,10-tetracarboxylic dianhydride (PTCDA, $C_{24}H_8O_6$) on Ag(110) are used. We consider field strengths between -0.3 V/Å and 0.3 V/Å which are realizable in optical experiments [86].

This third system was chosen since PTCDA has polar groups within the molecule due to the oxygen atoms. First, the effects of the electric field onto the positions of the constituent atoms are analyzed to observe whether the considered field strengths are strong enough to result in a collective vibration of the molecule. Afterwards, the changes in the DOS projected onto the atomic and molecular orbitals of the interfaces, in the geometry obtained after relaxation without field, are investigated to solely analyze the electronic polarization due to the field. Hereby, a Bader charge analysis was performed

[80–83] to quantify the charge transfer for each considered field. Lastly, the charge density difference due to the electric field and the charge rearrangements due to adsorption and field are visualized.

5.2 Comparison of vdW-correction schemes

For the simulation of the interface, we set up a supercell with 5 substrate layers and a vacuum gap of around 22 Å and 23 Å for 6P on Cu(110) and Ag(110), respectively. We chose the experimental lattice constants of 4.08 Å for bulk Ag and 3.61 Å for bulk Cu. 6P orients on Cu(110) along the $[1\bar{1}0]$ parallel to the close-packed rows, as reported in [87], and on Ag(110) along the [001] direction perpendicular to the close-packed rows [84]. The corresponding surface unit cell vectors b_1 and b_2 are 7.3 Å, 28.5 Å with an enclosing angle α of 82.7° for 6P on Cu(110) (see Fig. 5.1, left panel) and 28.7 Å and 8.7 Å with an enclosing angle of 84.2° for 6P on Ag(110) (see Fig. 5.1, right panel). The adsorption geometry of the molecule on the two substrates will be further discussed in the subsequent Section 5.3.

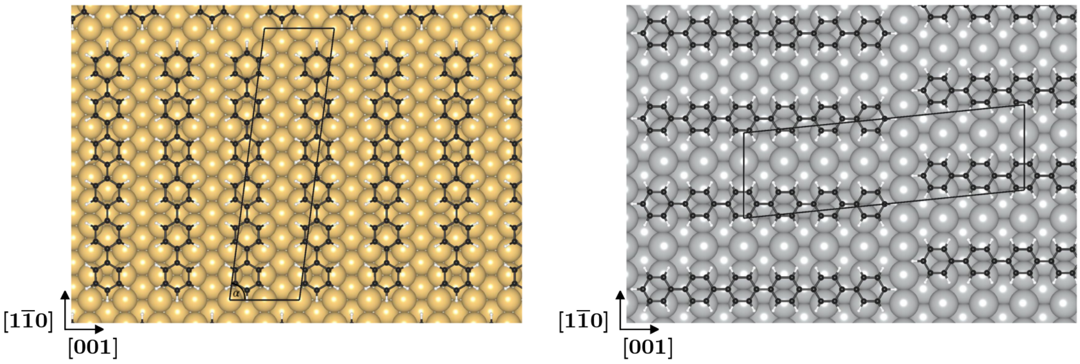

Figure 5.1: Surface unit cell of 6P/Cu(110) (left) and 6P/Ag(110) (right).

We assume that by driving the system with a strong external electric field in z-direction, it will induce a collective vibrational motion perpendicular to the substrate plane. To quantify the frequency needed to induce such a vibration, standard vdW-corrected DFT calculations were performed where the molecule is translated out of its equilibrium position in z-direction in a range of $[-0.5, 0.5]$ Å in 0.05 Å steps. For each step, an SCF-cycle was performed to calculate the total energy while keeping the geometry fixed. The resulting energies relative to the equilibrium energy, denoted by ΔE, were then plotted as a function of the displacement Δz. Fitting the data in the vicinity of the minimum by a parabolic function $E(x) = ax^2+bx+c$, where x is the displacement Δz, allows to determine the curvature which is directly proportional to the frequency f according to

$$f = \frac{1}{2\pi}\sqrt{\frac{1}{m}\frac{d^2E}{dx^2}}, \tag{5.1}$$

where m is the mass of the molecule. From this, we can estimate the frequency needed to excite the molecule in this specific vibrational state.

The calculations for 6P on Cu(110) and Ag(110) were performed using the GGA-PBE functional and five different vdW-correction methods for comparison. The used methods are the DFT-D3(zero) [47], DFT-D3(BJ) [49], the Tkatchenko-Scheffler (TS) method [50] and finally the two nonlocal vdW density functionals vdW-DF [55] and optB86b-vdW [56], introduced in Section 2.4.4. A $2 \times 6 \times 1$ Γ-centered k-grid for 6P/Ag(110) and $6 \times 2 \times 1$ k-grid for 6P/Cu(110), a first-order Methfessel-Paxton smearing of 0.15 eV [65] and 400 eV plane wave cut-off were used. The geometry relaxations were performed using damped molecular dynamics, as explained in Section 2.4.3. The geometries were optimized until the forces were below 0.01 eV/Å, for 6P/Cu(110), and 0.005 eV/Å, for 6P/Ag(110), since a displacement from the equilibrium position of the molecule actually gave lower energies than the energy obtained after the geometry relaxation. Even more precise geometry optimizations had to be done for the calculations with the nonlocal vdW density functionals vdW-DF for both systems. Here, the optimizations were terminated when the forces were below 0.002 eV/Å.

The adsorption distances d_A of the constituent atom types A of 6P for the different vdW-correction schemes are listed in Table 5.1. The vdW-DF scheme gives comparably large adsorption distances for both systems since it significantly underbinds as already found in earlier studies for various systems [88–92]. As a consequence of the large adsorption distance, little energy will be needed to induce a collective vibration of the molecule perpendicular to the substrate. When comparing the distances of 6P on Ag(110) with experimental results obtained for the functional group of PTCDA on Ag(110) ($d_\mathrm{funct} = 2.45$ Å) in [93] or pentacene on Ag(111) ($d = 2.43$ Å) and Cu(111) ($d = 3.9$ Å, low coverage and $d = 4.1$ Å, high coverage) in [94], they are in good agreement with the results obtained with the optB86b-vdW and the TS scheme, therefore, we can assume that these also give reasonable results for 6P on Cu(110).

Table 5.1 Adsorption distances d_A of the different atom types A of 6P/Cu(110) and 6P/Ag(110) in the equilibrium structure for the different vdW-correction schemes, namely DFT-D3(zero) [47], DFT-D3(BJ) [49], TS [50], vdW-DF [55] and optB86b-vdW [56]. The adsorption distance is given as the average value with its standard deviation.

	6P/Cu(110)		6P/Ag(110)	
	d_C (Å)	d_H (Å)	d_C (Å)	d_H (Å)
DFT-D3(zero)	2.38 ± 0.06	2.47 ± 0.05	2.86 ± 0.02	2.77 ± 0.03
DFT-D3(BJ)	2.32 ± 0.08	2.44 ± 0.06	2.74 ± 0.02	2.73 ± 0.02
TS	2.20 ± 0.10	2.38 ± 0.08	2.71 ± 0.03	2.71 ± 0.04
vdW-DF	3.34 ± 0.04	3.34 ± 0.04	3.27 ± 0.03	3.26 ± 0.03
optB86b-vdW	2.22 ± 0.09	2.40 ± 0.07	2.69 ± 0.04	2.70 ± 0.05

The following graphs show the resulting energies plotted as a function of the displacement Δz in the vicinity of the energy minimum for 6P on Cu(110) and Ag(110) with the fitted curve (solid line) (Fig. 5.2) for the different vdW corrections.

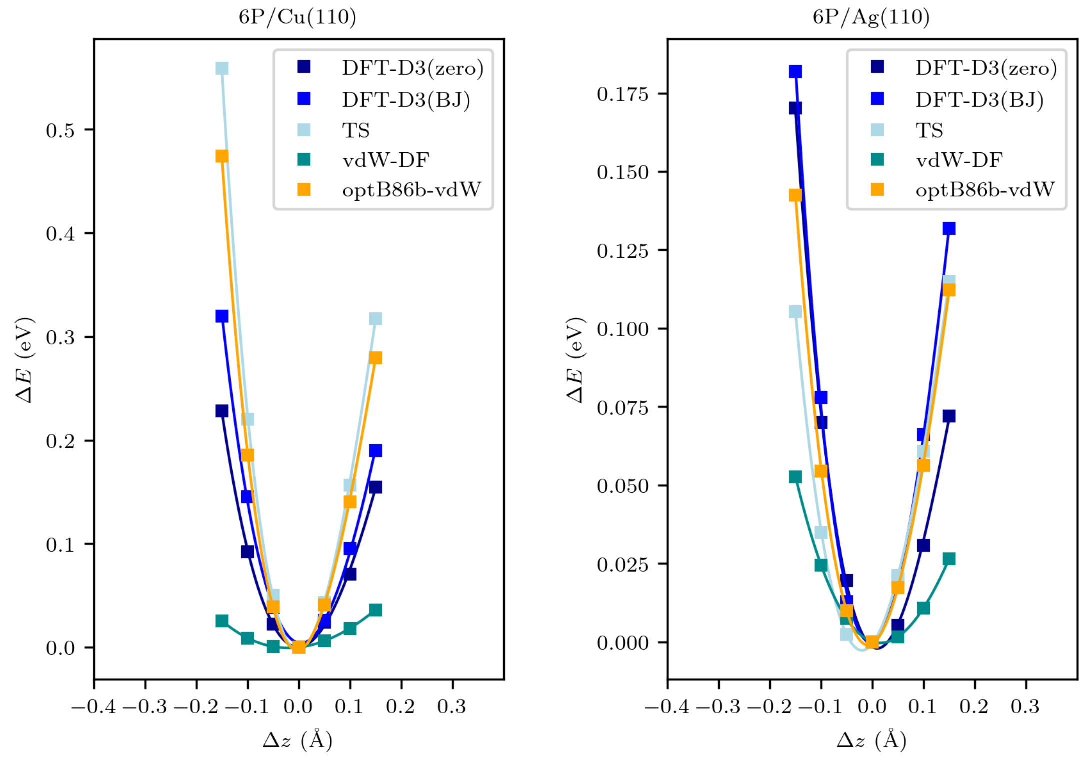

Figure 5.2: Energies with respect to the minimum energy of 6P/Cu(110) (left) and 6P/Ag(110) (right), denoted as $\Delta E = E - E_0$, as a function of displacement $\Delta z = z - z_0$ relative to the equilibrium position z_0 for the different vdW-correction schemes, namely DFT-D3(zero) [47], DFT-D3(BJ) [49], TS [50], vdW-DF [55] and optB86b-vdW [56]. The parabolic fit of the data is plotted as solid line.

Table 5.2 Frequency f (Eq. 5.1) needed to induce a vibrational motion of 6P perpendicular to the Cu(110) and Ag(110) substrate plane for the different vdW-correction schemes, namely DFT-D3(zero) [47], DFT-D3(BJ) [49], TS [50], vdW-DF [55] and optB86b-vdW [56].

	DFT-D3(zero)	DFT-D3(BJ)	TS	vdW-DF	optB86b-vdW
f (THz) (6P/Cu(110))	3.0	3.4	4.6	1.2	4.3
f (THz) (6P/Ag(110))	2.3	2.8	2.4	1.3	2.5

The vdW-DF gives considerably lower frequencies for both systems compared to the other vdW corrections (Tab. 5.2) as a result of the large adsorption distances (see Table 5.1). For 6P on Ag(110), the obtained frequencies are very similar which could stem from the weaker interaction of the molecule with the silver substrate due to the larger adsorption distance. Hence, the vdW interactions at the interface are weaker and they are well captured by all of the dispersion correction schemes (excluding vdW-DF). For 6P on Cu(110), the adsorption distance is smaller and the adsorbate-substrate interaction therefore stronger which leads to higher required frequencies to induce such a vibrational motion of the molecule and large deviations across the different vdW correction schemes. As the TS and optB86b-vdW results for the adsorption distances compare favorably with experiment [93], we assume a similar behavior for the frequencies yielding values of about 2.4 to 2.5 THz for 6P/Ag(110) and almost twice the value, 4.3 to 4.6 THz, for 6P/Cu(110), respectively. Even though we assume that the substrate and the molecule are rigid, therefore neglecting the intra-molecular motion, to obtain these frequencies, there will probably be an eigenmode that corresponds to a similar motion, as observed in a different study on NTCDA/Ag(111) [95].

5.3 Electronic structure

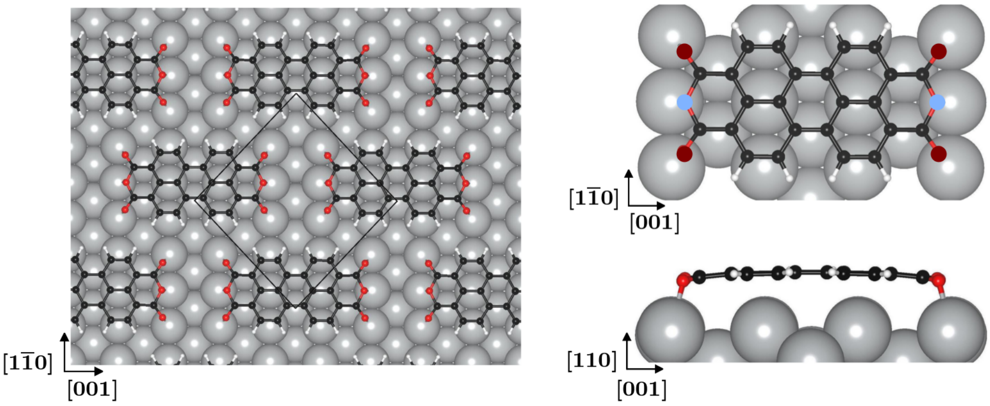

Figure 5.3: Surface unit cell and adsorption structure of the brickwall phase of PTCDA/Ag(110). In the upper right panel, the carboxylic oxygen atoms O_{carb} are colored in dark red and the anhydride oxygen atoms O_{anhyd} in light blue.

To analyze the effects of the static electric field on the structure and the charge rearrangements at the interface, we not only examine 6P on Cu(110) and Ag(110) but also PTCDA on Ag(110). Due to PTCDA's polar groups, namely the four carboxylic O_{carb} and two anhydride oxygen atoms O_{anhyd} (see Fig. 5.3, upper right panel), we expect a larger distortion of the molecule already upon adsorption and induced by the electric field. For the structure of PTCDA/Ag(110), the brickwall phase was chosen with one molecule inside the supercell oriented along the [001] direction as reported in Reference [96]. This phase of PTCDA/Ag(110) has already been observed experimentally and theoretically confirmed [96–99]. The substrate was simulated by five layers, with an Ag bulk lattice constant of 4.08 Å, and the vacuum gap of the supercell is around 22 Å.

The corresponding surface unit cell vectors were 12.1 Å and 12.1 Å with an enclosing angle of 86.6°. Calculations were performed using a $3 \times 3 \times 1$ k-grid and the structure was optimized using damped molecular dynamics until the forces were below 0.01 eV/Å. To account for the vdW-interactions the nonlocal optB86b-vdW-correction scheme was chosen for all further calculations and comparisons since it gave reasonable results for 6P/Cu(110) and 6P/Ag(110).

5.3.1 Equilibrium structures

First, the adsorption of the molecules in equilibrium, that is with no applied electric field, is analyzed. The smallest adsorption distance exhibits 6P on Cu(110) (see Tab. 5.3) due to the stronger substrate-adsorbate bonding. Consequently, the 6P molecule is significantly more distorted on the copper substrate with its hydrogen atoms pointing slightly upwards (see Fig. 5.4, top panel). In contrast, on Ag(110) the molecule adsorbs in a flat configuration (Fig. 5.4, bottom panel) due to the larger adsorption distance (see Tab. 5.3). PTCDA adsorbs with its oxygen atoms pointing towards the substrate, here, the O_{carb} atoms are slightly more bent towards the substrate. The calculated adsorption distances are getting close to the experimental values from normal incidence x-ray standing waves (NIXSW) experiments, reported in Reference [93]. Table 5.3 contains the adsorption energies, according to Equation 4.2, and average adsorption distances of the constituent atoms. Note that here and in all further calculations, the geometries were optimized using damped molecular dynamics until the forces were below 0.01 eV/Å hence the slight difference in the adsorption distances of 6P/Ag(110) in Table 5.1 and Table 5.3. These differences will not affect the obtained results in this study.

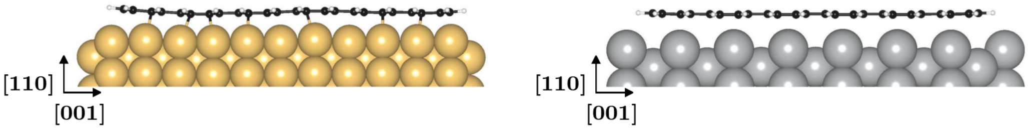

Figure 5.4: Side view of 6P/Cu(110) (left) and 6P/Ag(110) (right).

Table 5.3 Adsorption energies E_{ads} and $\tilde{E}_{\mathrm{ads}}$ and distances d_{A} of the different atom types A of 6P/Cu(110), 6P/Ag(110) and PTCDA/Ag(110). The theoretical adsorption distance is given as the average value with its standard deviation. Additionally, the adsorption distances for PTCDA/Ag(110) obtained from NIXSW experiments [93] are also listed.

	6P/Cu(110)	6P/Ag(110)	PTCDA/Ag(110)	exp.: PTCDA/Ag(110) [93]
E_{ads} (eV)	5.12	4.40	3.92	-
$\tilde{E}_{\mathrm{ads}}$ (eV)	7.06	4.58	4.54	-
d_{C} (Å)	2.22 ± 0.09	2.71 ± 0.03	2.61 ± 0.10	2.56±0.01
d_{H} (Å)	2.40 ± 0.07	2.72 ± 0.04	2.68 ± 0.09	-
$d_{\mathrm{O_{anhyd}}}$ (Å)	-	-	2.39 ± 0.08	2.38 ± 0.03
$d_{\mathrm{O_{carb}}}$ (Å)	-	-	2.32 ± 0.08	2.30 ± 0.04

The metal work function ϕ_0 and the work function of the full system ϕ of the three observed systems are listed in Table 5.4 together with the work function change $\Delta\phi$ and its contributions. The adsorption of 6P on Cu(110) and Ag(110) leads to a work function reduction of 1.15 eV and 0.83 eV, respectively, due to the large contribution of the Pauli pushback to the bond dipole $\Delta\phi_{\mathrm{bond}}$ at the interface. 6P/Cu(110) exhibits a larger reduction due to the strong molecular dipole $\Delta\phi_{\mathrm{bend}}$ induced by distortion of the molecule upon adsorption but a smaller bond dipole $\Delta\phi_{\mathrm{bond}}$ that can be attributed to the smaller adsorption distance promoting charge transfer into the molecule. By performing a Bader charge analysis [80–83], a charge transfer of 1.55 e into the molecule was calculated for 6P/Cu(110) and only 0.14 e for 6P/Ag(110). In contrast to these two systems, the adsorption of PTCDA on Ag(110) results in almost no work function change. Since PTCDA is a strong acceptor, the Pauli pushback is compensated almost entirely by the charge transfer of 1.30 e into the molecule, leading to a positive bond dipole $\Delta\phi_{\mathrm{bond}}$. Due to the downward bending of the oxygen atoms upon adsorption, the molecule shows an intrinsic dipole of similar magnitude to the one of 6P on Cu(110). Even a work function increase has been observed theoretically, as reported in Reference [96]. Note that the difference in the metal work function, compared to the 4.05 eV for Ag(110) calculated with DFT-D3(zero) reported in Reference [96], stems from the nonlocal optB86b-vdW-correction scheme that gives work functions 0.2-0.3 eV higher compared to experimental values (for example, $\Phi_0(\mathrm{Cu}(110)) = 4.56$ eV and $\Phi_0(\mathrm{Ag}(110)) = 4.10$ eV [100]). This has already been observed for another nonlocal vdW-correction, the vdW-DF-cx [100].

Table 5.4 Work functions and contributions to the work function change of 6P/Cu(110), 6P/Ag(110) and PTCDA/Ag(110). ϕ_0: Work function of the substrate, determined at the bottom of the slab, ϕ: Work function of the adsorbed molecule system, $\Delta\phi_{\text{bond}}$: Bond dipole, the change in the work function due to the charge rearrangement upon adsorption, $\Delta\phi_{\text{bend}}$: Molecular dipole, potential difference below and above the molecule in the adsorption geometry without substrate, $\Delta\phi_{\text{surf}}$: Surface dipole change, the potential difference below and above the substrate layers in the final geometry.

	6P/Cu(110)	6P/Ag(110)	PTCDA/Ag(110)
ϕ_0 (eV)	4.72	4.45	4.51
ϕ (eV)	3.57	3.62	4.46
$\Delta\phi = \phi - \phi_0$ (eV)	-1.15	-0.83	-0.05
$\Delta\phi_{\text{bond}}$ (eV)	-0.68	-0.77	0.36
$\Delta\phi_{\text{bend}}$ (eV)	-0.40	-0.02	-0.36
$\Delta\phi_{\text{surf}}$ (eV)	-0.05	-0.00	-0.03

The plane-averaged charge rearrangements $\Delta\rho$, according to Equation 4.4, and the change in the electrostatic potential ΔV in the systems, are plotted in Figure 5.5. Here, the step of the electrostatic potential ΔV across the molecule represents the bond dipole $\Delta\phi_{\text{bond}}$. For 6P/Cu(110), on the one hand, we see that electrons are depleted close to the metal surface and pushed back far into the bulk due to Pauli pushback. On the other hand, electrons accumulate right below and, to a small contribution also above the molecule at the π-lobes which corresponds to charge transfer into the LUMO. In 6P/Ag(110) there is only little charge transfer into the molecule, hence most of the contribution to the bond dipole comes from Pauli pushback. For that reason, charge accumulates between the molecule and the substrate since charge is also pushed in the regions that are not covered by the molecule and at the topmost substrate layer. Electrons are depleted right above and below the molecule corresponding to a depletion of electrons from the π-lobes. There is no charge transfer from or into the σ-lobes since the charge rearrangements are almost zero at the plane of the molecule. For PTCDA on Ag(110), the situation is similar to 6P on Cu(110) where there is charge transfer, but the Pauli pushback effect in this system is much weaker due to the larger adsorption distance of PTCDA. The Pauli pushback effect shows in the depletion of electrons at the interface and accumulation at the topmost Ag-layer. Furthermore, electrons are depleted from the σ-lobes and accumulate at the π-lobes of the molecule due to charge transfer into the LUMO.

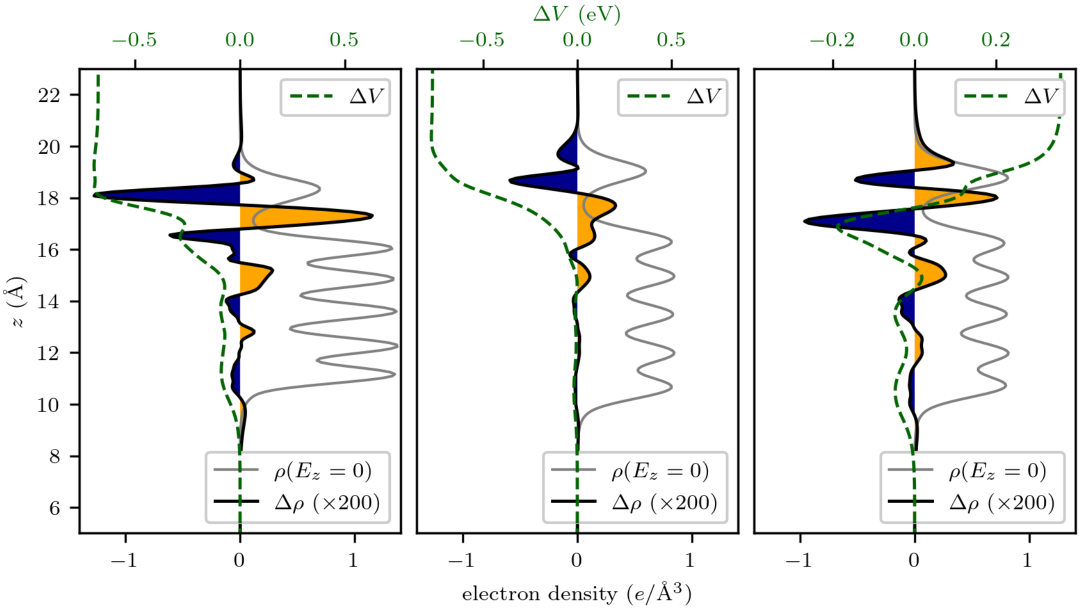

Figure 5.5: Charge rearrangements of 6P/Cu(110), 6P/Ag(110) and PTCDA/Ag(110) (from left to right) in equilibrium. The black line denotes the plane-averaged charge density $\Delta\rho\,(\times 200)$, the grey line the charge density ρ of the full system, the dotted green line the change in the electrostatic potential ΔV and the colored areas indicate electron depletion (darkblue) and accumulation (orange).

5.3.2 Geometric structure under static electric fields

Using the VASP code, it is possible to apply static electric fields in a direction perpendicular to the substrate plane. Note that, when applying a field in VASP, the electrons move in the direction of the field. So a positive (negative) static electric field in z-direction moves electrons in the positive (negative) z-direction contrary to the physical description of an electric field. For the analysis in this thesis, we will use the description of VASP.

First, we considered static electric fields with field strengths between -0.3 V/Å and 0.3 V/Å in z-direction and performed geometry relaxations to analyze how large the displacement of the molecule due to the field is. The changes of the average adsorption distance of the different atom types A in the molecule with respect to the equilibrium adsorption distance, denoted as $\Delta d_\mathrm{A} = d_\mathrm{A} - d_{\mathrm{A},0}$, is plotted in Figure 5.6 and listed in Table 5.5 for 6P/Cu(110), 6P/Ag(110) and PTCDA/Ag(110) (see Table 5.3 for the equilibrium adsorption distances). Other than originally expected, not all atoms in the molecule are collectively displaced in one direction but the more electronegative atoms, carbon and oxygen, are displaced in the field direction since these accumulate electrons. The average vertical shifts of the carbon atoms, Δd_C, and oxygen atoms, Δd_O, (Tab. 5.5) are larger for a negative applied electric field due to the reduced surface dipole and smaller for a positive applied electric field because of the bonding between the molecule and the substrate. In contrast, the hydrogen atoms are displaced in the opposite direction by the electric field due to their low electronegativity and partially positive charge (Fig. 5.6, upper panels). The reason for the larger displacements in PTCDA (Fig. 5.6, lower panel) are the oxygen atoms that are more electronegative compared to carbon which leads to a stronger polarization within the molecule. The displacement of the carboxylic oxygens is stronger, compared to the anhydride oxygens, since there is more charge on these atoms due to the LUMO filling. The reason for the hydrogen atoms also being displaced towards the surface in the case of a negative field could be the larger displacement of the carbon and oxygen atoms so that the hydrogen atoms are displaced with them, as originally expected.

Table 5.5 Average deviation Δd_A (pm) from the equilibrium adsorption distance (Tab. 5.3) of the atom types A in 6P/Cu(110), 6P/Ag(110) and PTCDA/Ag(110) due to the electric field E_z (V/Å). The adsorption distance is defined as the distance to the topmost substrate layer.

	E_z	-0.3	-0.2	-0.1	0.1	0.2	0.3
6P/Cu(110)	Δd_C	-0.42	-0.33	-0.14	-0.05	0.03	0.20
	Δd_H	0.32	0.18	0.04	-0.16	-0.28	-0.58
6P/Ag(110)	Δd_C	-1.68	-1.17	-0.55	0.00	0.17	0.39
	Δd_H	0.06	-0.05	-0.09	-0.35	-0.69	-0.97
PTCDA/Ag(110)	Δd_C	-2.00	-1.68	-0.86	-0.10	0.05	0.24
	Δd_H	-0.68	-0.80	-0.55	-0.34	-0.61	-0.88
	$\Delta d_{\mathrm{O}_\mathrm{carb}}$	-3.25	-2.39	-1.09	0.26	0.99	1.69
	$\Delta d_{\mathrm{O}_\mathrm{anhyd}}$	-2.84	-2.14	-0.95	-0.06	0.28	0.73

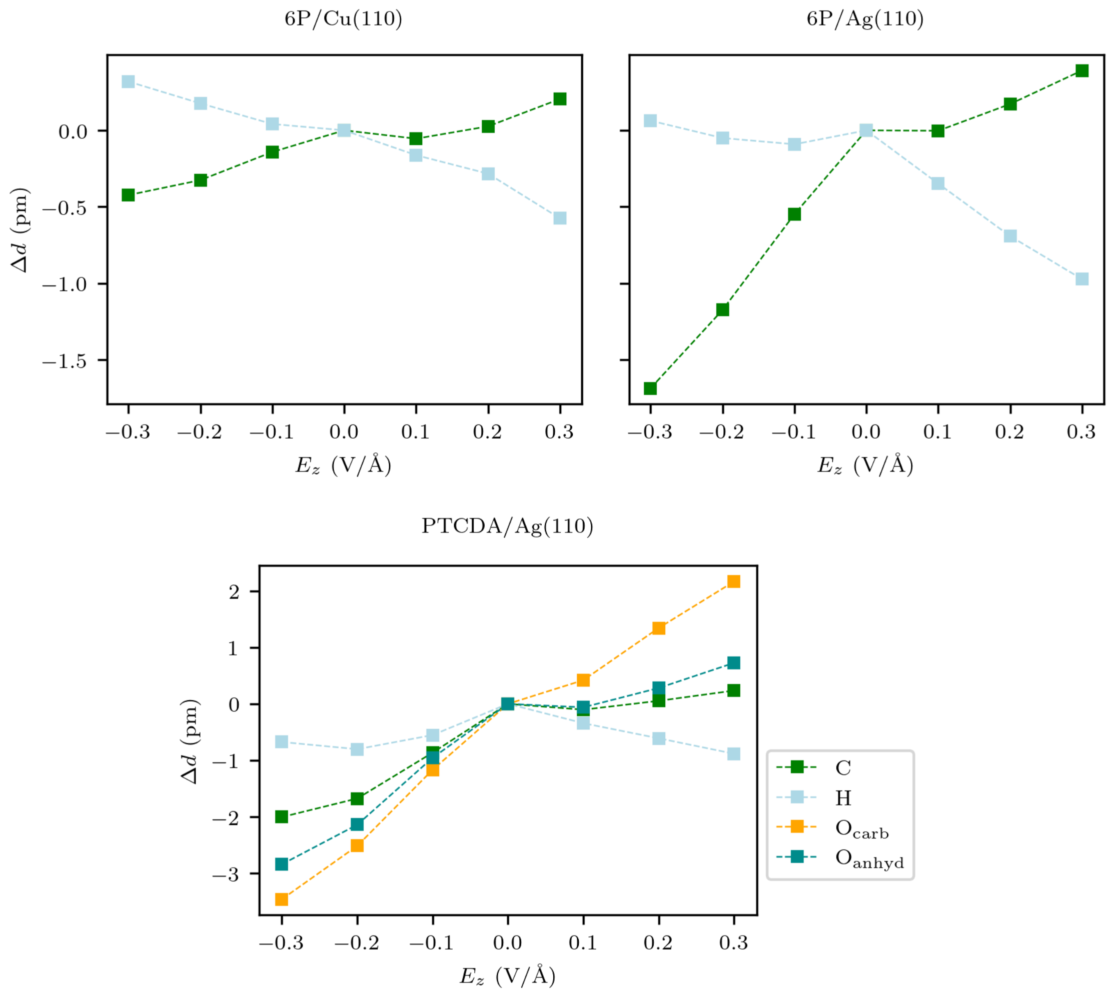

Figure 5.6: Average deviation Δd from the equilibrium adsorption distance of the atoms in 6P/Cu(110), 6P/Ag(110) and PTCDA/Ag(110) due to the electric field E_z. The adsorption distance is defined as the distance to the topmost substrate layer. The hydrogen is marked in light blue, carbon in green, carboxylic oxygen in orange and anhydride oxygen in dark cyan.

5.3.3 Electronic structure under static electric fields

In this section, we investigate how external static electric fields affect the electronic structure of organic-metal interfaces on the three considered systems, 6P/Cu(1110), 6P/Ag(110) and PTCDA/Ag(110). In order to separate geometrical effects from purely electronic ones, we performed two types of calculations. First, we analyzed the changes in the electronic structure taking into account the geometrical changes discussed in the previous section, but switching off the electric field. The resulting PDOS is depicted in Figure 5.7 and shows little variations due to the changes in the geometry. Therefore, we can conclude that the geometrical changes alone have no noticeable effect on the charge rearrangements in the systems and cannot induce charge transfer into the molecule at the considered field strengths. However, experimentally, there will probably be larger geometrical changes due to the thermal motion of the molecules at room temperature.

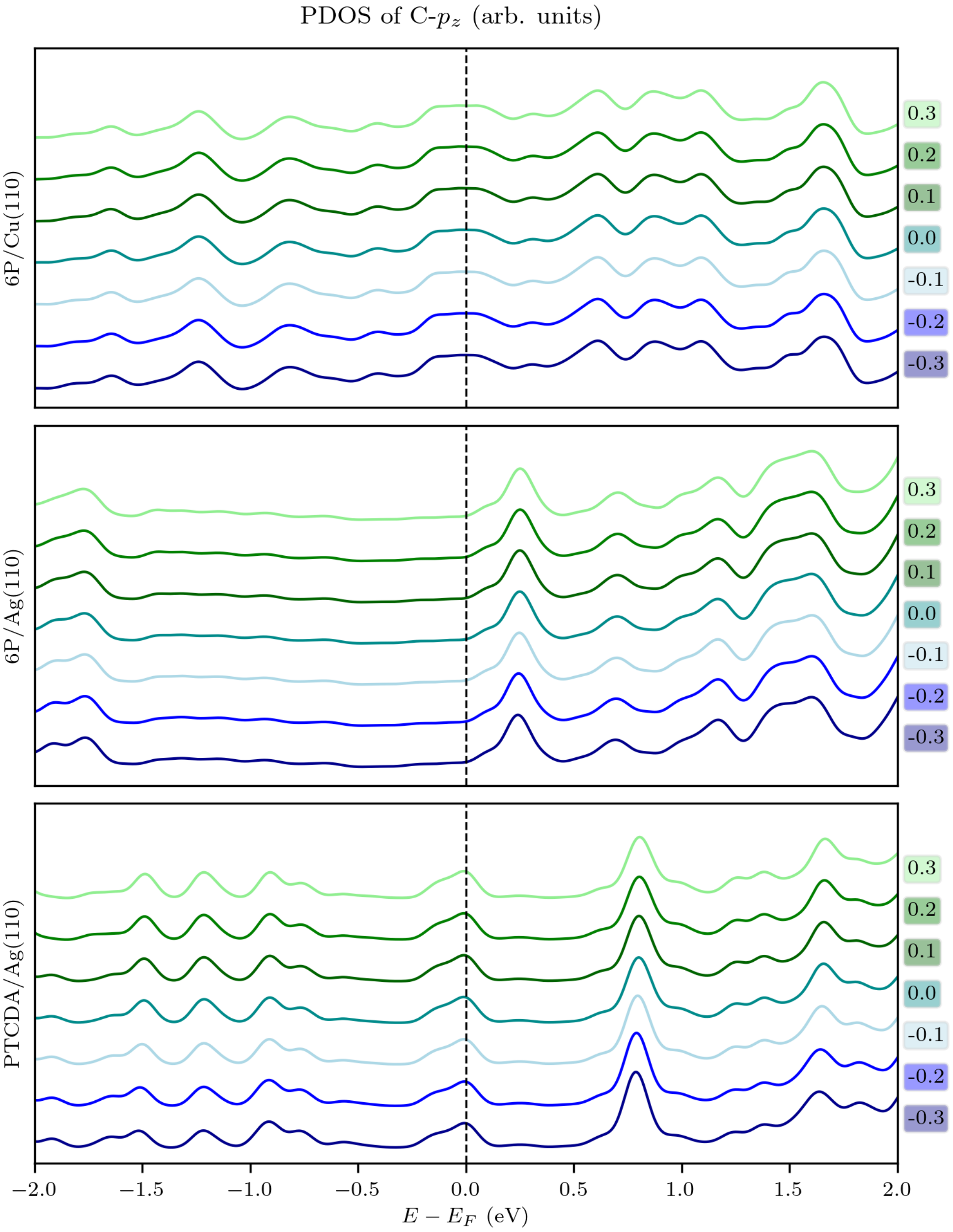

Figure 5.7: Geometrical effect on the DOS projected on the C-p_z atomic orbitals for 6P/Cu(110), 6P/Ag(110) and PTCDA/Ag(110) (from top to bottom). Here, the geometries are taken from structural optimizations with the applied electric field E_z, but the PDOS is evaluated for $E_z = 0$ V/Å. The value of E_z (V/Å) for the structural optimizations is noted outside the plots.

In the second type of analysis, the optimized structures in equilibrium ($E_z = 0$ V/Å) were fixed and solely the effect of the electric field on the electronic structure was studied, which can be explained as follows. When applying a positive static electric field in z-direction (perpendicular to the substrate plane), electrons will be pulled from the metal towards the molecule, thereby increasing the surface dipole. Implicitly, the applied positive field is counteracting the Pauli pushback and therefore inducing or amplifying charge transfer from the substrate into the molecule depending on the equilibrium situation without field. When applying a negative static electric field in z-direction, the surface dipole is decreased due to the electrons moving towards the substrate therefore the charge transfer into the molecule is reduced or charge transfer into the substrate is induced, depending on the system's equilibrium situation. Regarding the three different systems studied in this chapter, in equilibrium, the LUMO lies almost completely below (PTCDA/Ag(110)), mainly at the Fermi edge (6P/Cu(110)) or slightly above (6P/Ag(110)). In all systems, the PDOS for C-p_z clearly changes when varying the field strength, despite the geometries being held fixed at the zero-field structures (see Fig. 5.8). The PDOS considerably "shifts" to lower energies with increasing electric field. This shift is hardly noticeable for 6P/Cu(110) due to the strong substrate-adsorbate interaction and the consequent hybridization. Nevertheless, the LUMO, located at the Fermi level, does get filled continuously with increasing field. This can be further quantified by performing a Bader charge analysis [80–83] (see Tab. 5.6 and Fig. 5.9). Note that the LUMO of 6P on Cu(110) extends far below the Fermi level (around 1 eV) which is better visible in the MOPDOS at the top panel of Figure 5.10. For 6P/Ag(110), the calculated changes in the PDOS are very pronounced for field strengths above 0.1 V/Å where an additional peak appears below the Fermi edge. This peak could stem from strong hybridization with the metal substrate at the corresponding applied electric field. Furthermore, with decreasing electric field, the peak position of the LUMO moves towards higher energies. As the LUMO is almost fully occupied for PTCDA/Ag(110), the LUMO shifts even further below the Fermi level. Note that, as for 6P/Cu(110), the LUMO of PTCDA spreads over 1 eV when looking at the MOPDOS at the bottom panel of Figure 5.10.

In Figure 5.9, we plot the charge transfer from the substrate into the molecule, as obtained from the Bader charge analysis. The steepness of the slope indicates how easily the electrons move into the LUMO of the molecule (positive field) and back into the metal (negative field). For 6P on Cu(110), electrons are the most easily transferred into the LUMO and back because of the LUMO position with respect to the Fermi level (see Fig. 5.10). For 6P on Ag(110), charge is even transferred into the metal when applying a negative electric field with a field strength greater than -0.1 V/Å.

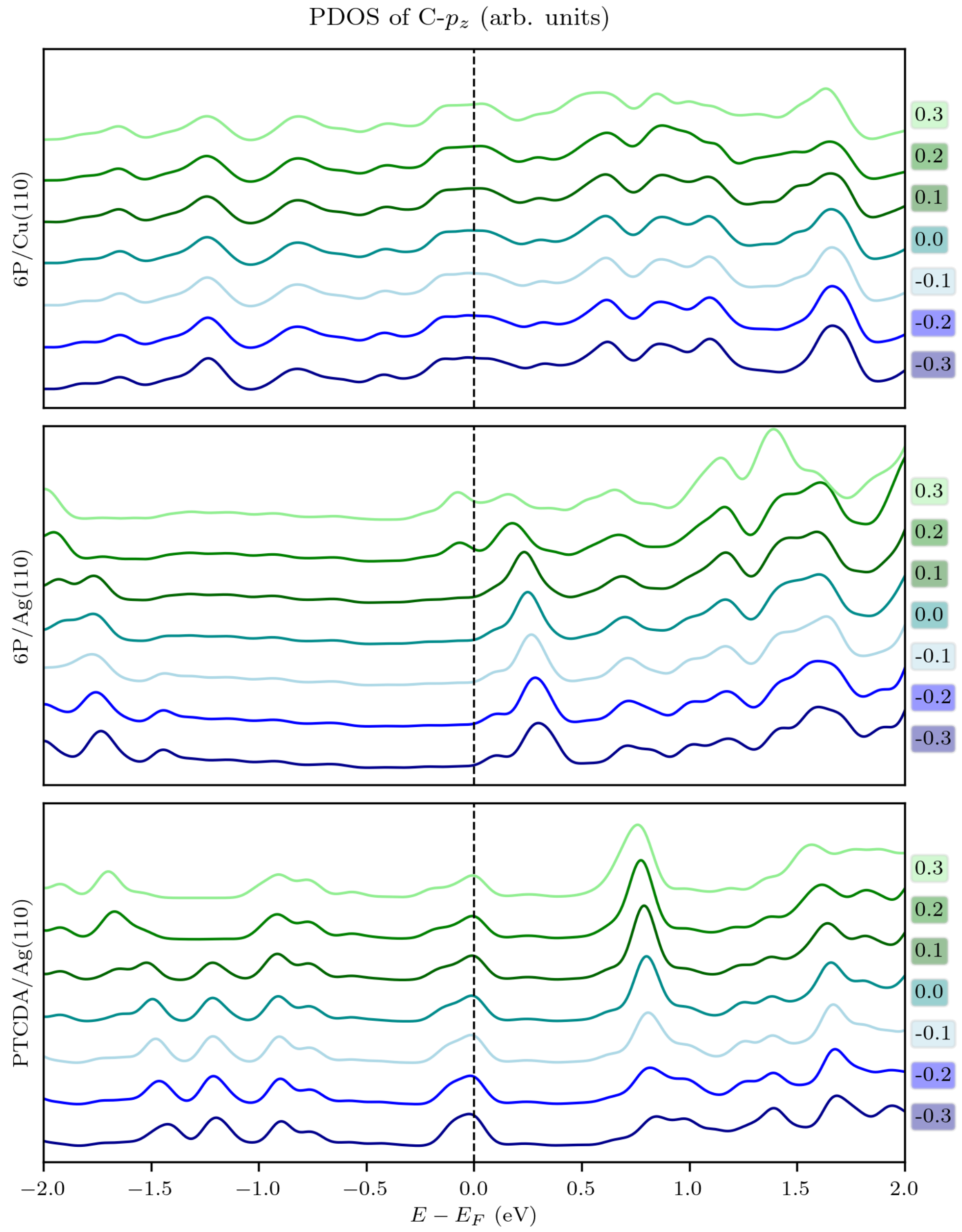

Figure 5.8: Electronic effect of the electric field E_z on the DOS projected on the C-p_z atomic orbitals for 6P/Cu(110), 6P/Ag(110) and PTCDA/Ag(110) (from top to bottom). Here, the geometries are fixed to the optimized geometry in equilibrium ($E_z = 0$ V/Å). The value of the applied electric field E_z (V/Å) is noted outside the plots.

Table 5.6 Charge transfer from the substrate to the molecule in 6P/Cu(110), 6P/Ag(110) and PTCDA/Ag(110) for the considered electric fields E_z. The charge transfer is calculated by performing a Bader charge analysis [80–83].

	Charge transfer into the molecule (e)		
E_z (V/Å)	6P/Cu(110)	6P/Ag(110)	PTCDA/Ag(110)
-0.3	1.26	-0.09	1.13
-0.2	1.36	-0.01	1.19
-0.1	1.45	0.06	1.24
0.0	1.55	0.14	1.30
0.1	1.65	0.22	1.36
0.2	1.75	0.31	1.41
0.3	1.84	0.40	1.47

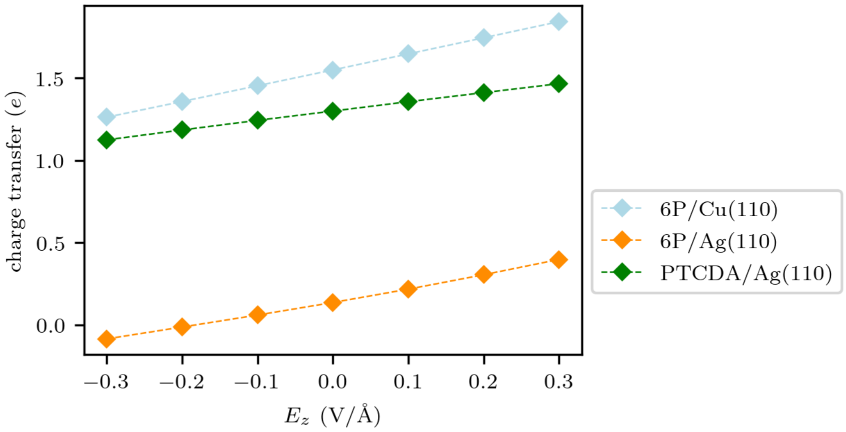

Figure 5.9: Charge transfer from the substrate to the molecule in 6P/Cu(110), 6P/Ag(110) and PTCDA/Ag(110) for the considered electric fields E_z. The charge transfer is calculated by performing a Bader charge analysis [80–83].

To get a clearer picture of the increased (decreased) charge transfer into the LUMO by applying a positive (negative) electric field, we further projected the DOS onto the molecular orbitals (see Fig. 5.10), by Equation 4.5 [24]. Here, the cyan and green vertical lines indicate the peak positions of the HOMO and LUMO in equilibrium ($E_z = 0.0$ V/Å), respectively. Several interesting aspects can be deducted from this analysis. First, due to the stronger interaction between 6P and the copper surface, the molecular orbitals are significantly more broadened (Fig. 5.10, top panel) compared to the molecular orbitals of 6P and PTCDA on silver. Additionally, the peak positions of the molecular orbitals do not change significantly which is also a result of the strong substrate-adsorbate coupling. However, the filling of the LUMO is significantly increased (decreased) in response to the positive (negative) electric field. This can, for instance, be seen for 6P/Cu(110) when looking at the smaller peak right below the Fermi energy and even the LUMO+1 is dragged partly below the Fermi level. For 6P on Ag(110), the substrate-adsorbate coupling is less strong, hence the peaks of the molecular orbitals shift to more negative energies with increasing electric field. The molecular orbitals of PTCDA on Ag(110) show a similar shift as the molecular orbitals of 6P on Ag(110). Here, the contributions of the LUMO shift to lower energies when looking at the original peak for no applied field (marked by the green vertical line) losing intensity with increasing positive field strength.

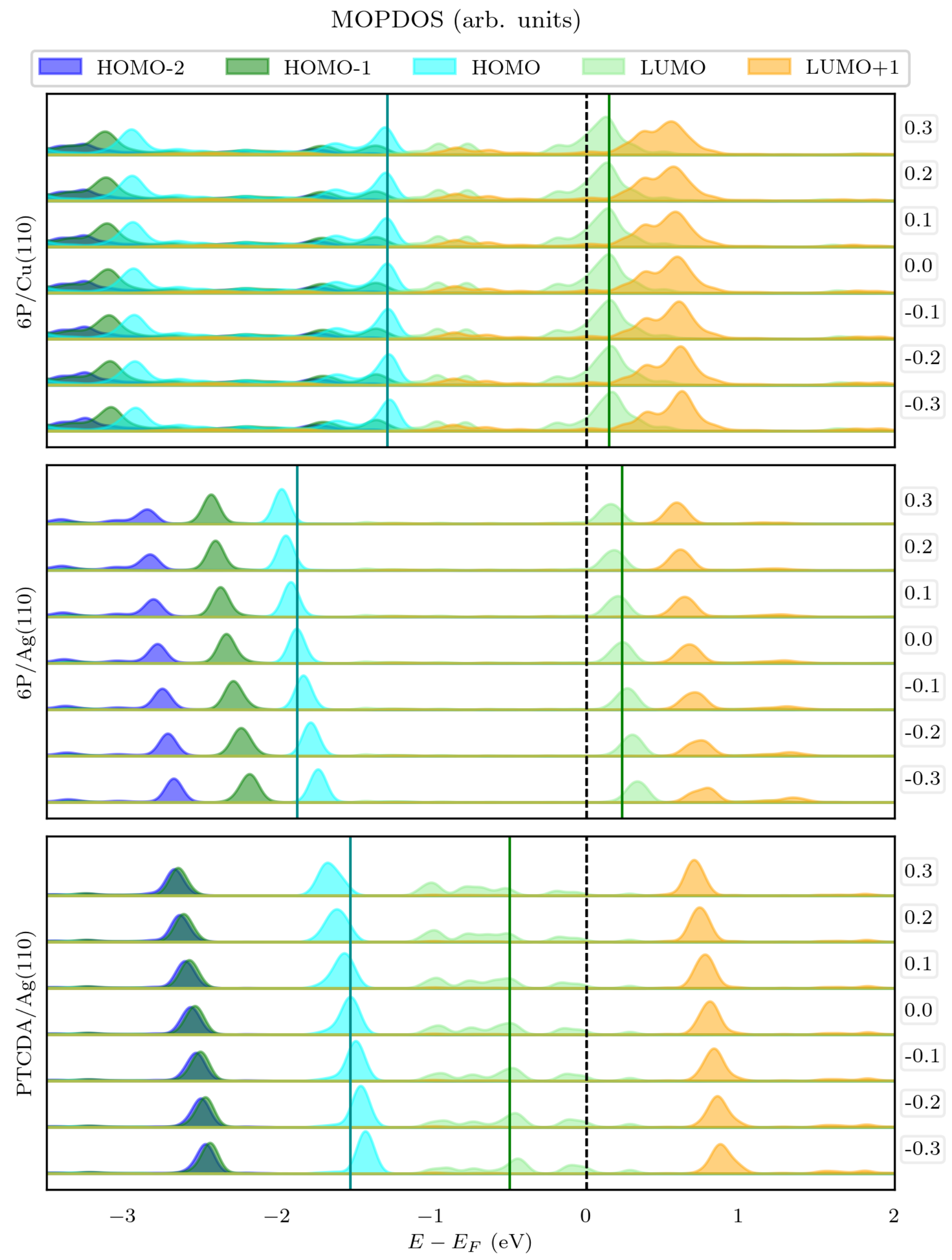

Figure 5.10: MOPDOS of 6P/Cu(110), 6P/Ag(110) and PTCDA/Ag(110) (top to bottom) in the equilibrium geometry for the considered external electric fields E_z. The cyan vertical line marks the peak of the HOMO and the green vertical line the peak of the LUMO in equilibrium ($E_z = 0.0$ V/Å). The value of the applied electric field E_z (V/Å) is noted outside the plots.

To further analyze the electronic structure, the plane-averaged induced charge density $\delta\rho(E_z)$ in response to the electric field is calculated according to following equation

$$\delta\rho(E_z) = \rho(E_z) - \rho(E_z = 0) \tag{5.2}$$

and plotted in Figure 5.11. The electric field induces a polarization and, therefore, most of the electrons are accumulated (depleted) above the adsorbate and depleted (accumulated) below the substrate for a positive (negative) applied electric field. In Figure 5.11, the largest charge density differences are exhibited for the largest absolute field strengths, here, the light green line for $E_z = 0.3$ V/Å and the dark blue line for $E_z = -0.3$ V/Å. Another behavior shown in all three systems is, on the one hand, the increased electron spill-out of the surface when applying a positive electric field, which then counteracts the pushback effect. On the other hand, electrons are depleted right above the metal surface when applying a negative electric field, therefore the pushback effect is amplified. For 6P/Cu(110), electrons clearly accumulate below and above the molecule at the π-lobes and deplete from the σ-lobes (plane of the molecule) when applying a positive electric field. This corresponds to an increased charge transfer into the LUMO. The opposite occurs for a negative electric field, where electrons deplete from the π-lobes and accumulate at the σ-lobes. The situation is similar for 6P/Ag(110) and PTCDA/Ag(110) due to increased (decreased) charge transfer into the LUMO when applying a positive (negative) electric field. However, the change in the electron density right above the surface is larger for these two systems due to the larger adsorption distances, compared to 6P on Cu(110).

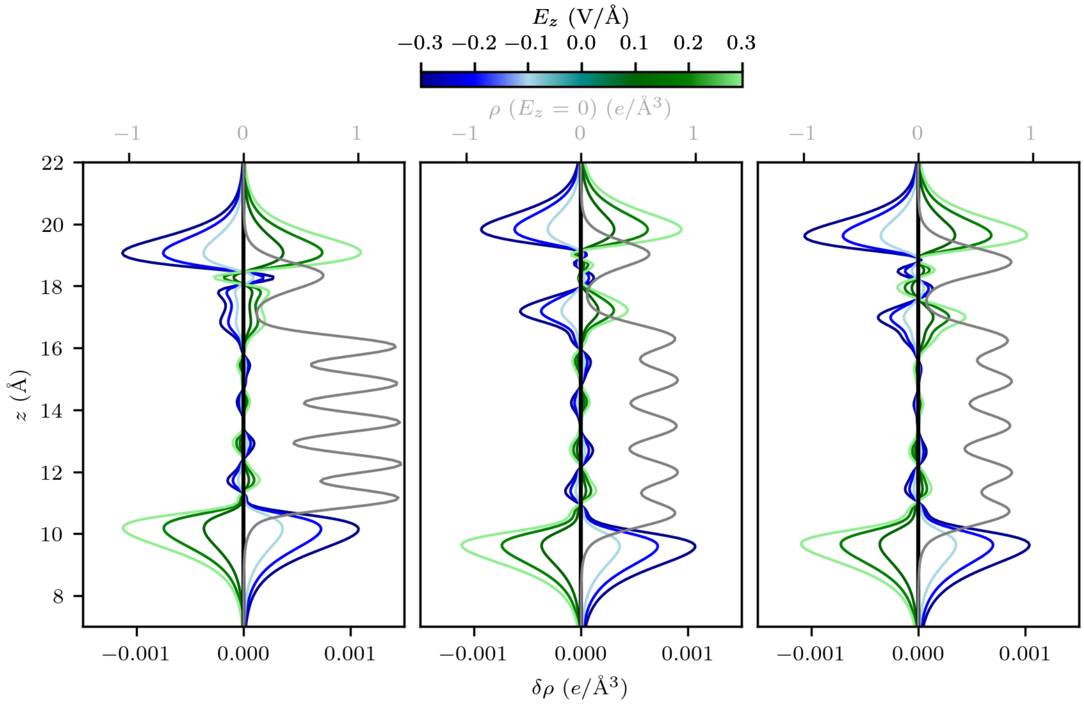

Figure 5.11: Induced charge density $\delta\rho(E_z)$ of 6P/Cu(110), 6P/Ag(110) and PTCDA/Ag(110) (left to right) in response to different external electric fields E_z. The grey line denotes the charge $\rho(z)$ of the full system in equilibrium ($E_z = 0.0$ V/Å).

Finally, we analyze the electric field induced charge rearrangements in yet another way. To this end, we compute the following quantity

$$\Delta\rho(E_z) = \rho(E_z) - (\rho_{\text{mol}}(E_z = 0) + \rho_{\text{sub}}(E_z = 0)) \,. \tag{5.3}$$

Thus, $\Delta\rho(E_z)$ describes the charge rearrangements due to adsorption and due to the electric field. To see that this expression gives the charge rearrangements due to adsorption and due to the electric field, the relation for the charge rearrangements (Eq. 4.4) $\rho_{\text{mol}}(E_z = 0) + \rho_{\text{sub}}(E_z = 0) = -\Delta\rho(E_z = 0) + \rho(E_z = 0)$ can be inserted into the equation and the expression then exactly gives the sum of the induced charge density $\delta\rho(E_z)$ and the charge rearrangements in equilibrium $\Delta\rho(E_z = 0)$. $\Delta\rho(E_z)$ is plotted in Figure 5.12 for the discussed systems to get an overall picture of the changes in the charge rearrangements upon adsorption due to the field. It's trivial that for $E_z = 0$ V/Å the curve is identical to the charge rearrangements in Figure 5.5 since there are no induced charges. Note that the induced charge density differences $\delta\rho(E_z)$ in Figure 5.11 are significantly smaller than the charge rearrangements $\Delta\rho(E_z)$. For that reason, the changes above the molecule, below the substrate and right at the interface are mainly visible.

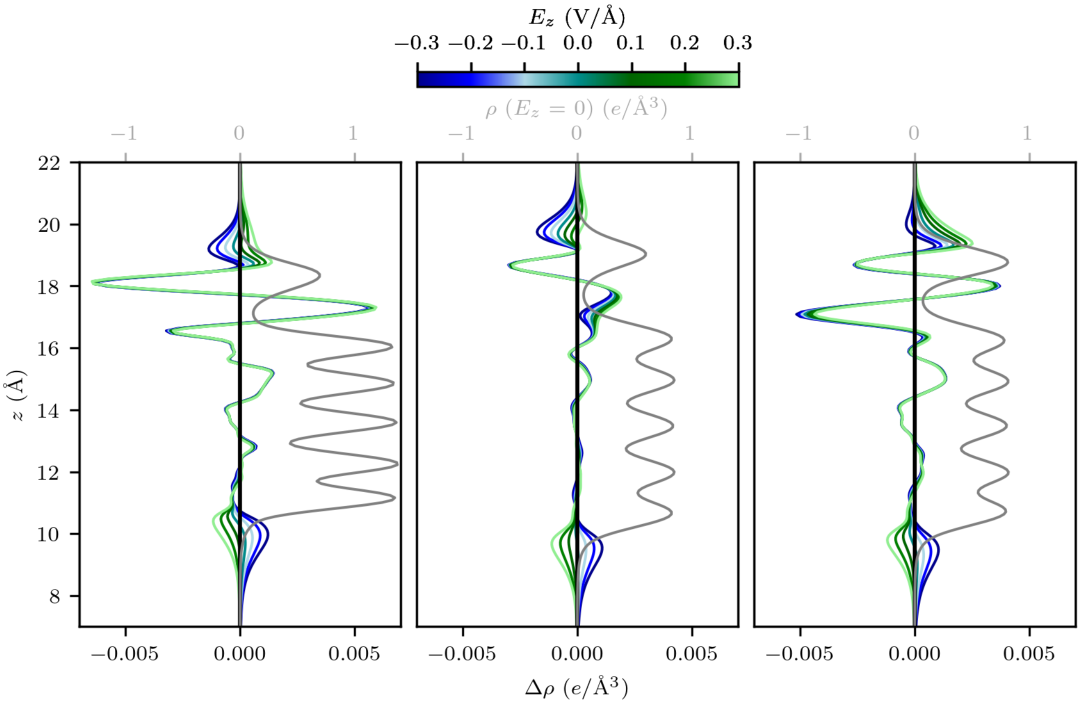

Figure 5.12: Charge rearrangement $\Delta\rho(E_z)$ of 6P/Cu(110), 6P/Ag(110) and PTCDA/Ag(110) (left to right) due to adsorption and due to different external electric fields E_z. The grey line denotes the charge $\rho(z)$ of the full system in equilibrium ($E_z = 0.0$ V/Å).

6 Conclusion

This chapter concludes the key findings of the three projects carried out in this thesis in relation to their research objectives and questions. Additionally, we discuss the limitations of our studies and propose potential future research.

The goal of the first project, discussed in Chapter 3, was to determine the optimal U_{eff} value of Dudarev's GGA+U approach [16] with respect to the computationally more expensive hybrid functionals, PBEh [12–14] and HSE06 [11], for the two transition metal complexes (TMC), transition metal phthalocyanine (TMPc) and porphine (TMP). Here, TM = Mn, Fe, Co, Ni, Cu and Zn cover a range of magnetic spin moments from S = 3/2, 1, 1/2, 0, 1/2 and 0, respectively. Since the PBEh and HSE06 calculations for each transition metal complex show the same orbital ordering and only differ in the HOMO-LUMO gap, the GGA+U calculations are only compared to HSE06. The comparison reveals that for the non-magnetic TMPcs and TMPs (TM = Zn, Ni) the description of the d-states improves with increasing U_{eff} and U_{eff} values around 6 eV to 7 eV would be the ideal choice. The TMC with a total spin moment S = 1/2 (TM = Co, Cu) show a similar behavior, but here, the TMPs' d-orbital energies fluctuate more with U_{eff}. For the other magnetic TMPcs and TMPs (TM = Fe, Mn) a value below 6 eV should be chosen. Here, it is difficult to make a definite choice based on the total spin moment due to larger fluctuations in the total and local magnetic moments for the GGA+U calculations. These are very sensitive to the initialization of the total magnetic moment and could be related to the number of unpaired electrons in the system. Additionally, it is important to note that the hybrid functional calculations have been performed as single-point computations, that is, relying on the geometry obtained from PBE-GGA which could slightly impact the orbital energies and magnetic moments of these calculations. In the context of future research, this study could be extended to analyzing the bond lengths between the transition metal and the directly bound N atoms since these influence the orbital and electronic degeneracies.

In the theoretical study done for the second project, we tested several surface unit cells for peritetracene (peri4A) on the Cu(111) surface to find the best match with the low-energy electron diffraction (LEED) data. We find that peri4A adsorbs in a flat configuration on the hollow-hcp site. Based on this most favorable adsorption geometry, STM images simulated within the Tersoff-Haman approximation [25] turn out to be in excellent agreement with experimental data. We have also studied the adsorption of the precursor molecule 1,1'-bitetracene (bi4A) on Cu(111) and find that it also adsorbs on the hollow-hcp site, but in contrast to peri4A, does not get fully planarized upon adsorption due to the repulsion of the inner hydrogen atoms. The electronic structure analysis in terms of the charge rearrangements reveals that the work functions are reduced by 0.72 eV for peri4A/Cu(111) and 0.82 eV for bi4A/Cu(111), respectively. On the other hand, the projection of the DOS onto the molecular orbitals (MOPDOS) [24] demonstrates that the LUMOs of both molecules get filled upon adsorption. Due to the overall reduction of the work function, we conclude that the effect of the Pauli pushback has to be significantly larger than the effect of the charge transfer into the molecule. When comparing experimental ultraviolet photoemission (UPS) data with our calculated MOPDOS spectra, as obtained at the PBE-GGA level, we notice significant shifts on the energy axis. We have therefore performed additional HSE06 hybrid functional calculations which have resulted in good agreement with the experimental data. As a part of ongoing research, angle-resolved photoemission spectroscopy (ARPES) experiments could be conducted and compared to simulated momentum maps to confirm the filling of the LUMO.

The goal of the third project was to analyze the electric field induced charge transfer at organic-metal interfaces under the presumption that the field excites the molecule in a vibrational state that periodically modulates the vertical molecule-substrate distance. In an initial step, the frequency needed for such a vertical vibrational excitation has been determined for 6P on Cu(110) and Ag(110) by translating the molecule in z-direction out of its equilibrium position. By comparing the different local and nonlocal van der Waals functionals in terms of the adsorption distances and frequencies, we observe that the vdW-DF [55] method gives considerably larger adsorption distances and, therefore, low frequencies since it significantly underbinds. Our findings show that the adsorption distances obtained with the optB86b-vdW [56] and TS [50] scheme give comparable results to experimental ones [93]. Therefore, we assume a similar behavior for the frequencies. Although in our approach we have assumed, that the molecule and substrate are rigid, it is plausible that our results for the frequencies align with one of the existing vibrational eigenmodes of the molecule. While this study provides valuable insights, it is important to acknowledge that we performed standard DFT calculations at 0 K. To also consider thermal motion of the molecules, molecular dynamics simulations could be performed as a future study.

For all further studies of the three organic-metal interfaces, 6P/Cu(110), 6P/Ag(110) and perylene-3,4,9,10-tetracarboxylic dianhydride (PTCDA) on Ag(110), under the influence of the electric fields, the optB86b-vdW functional has been utilized. The analysis of the geometrical changes, for the considered field strengths (Section 5.3.2), revealed that the atoms in the molecule do not show a concerted vertical motion in the field direction, but rather that the more electronegative carbon and oxygen atoms move in the direction of the field and the less electronegative hydrogen atoms move in the opposite direction. In PTCDA/Ag(110) this effect is more pronounced due to more polar oxygen atoms. Here, the carboxylic oxygen atoms are displaced the most since they are more electronegative due to the LUMO filling. This also leads to the hydrogen atoms being 'dragged' along with them, as originally expected. However, the overall displacements are very small and do not significantly affect the electronic structure. There are, however, noticeable changes in the electronic structure when exposing the interface to the electric fields, even without considering the minor structural changes discussed above. We observe that there is an apparent increase in charge transfer into the molecule when applying a positive electric field and a decrease when applying a negative electric field. Since the LUMO of 6P on Ag(110) is located right above the Fermi level, charge is even transferred into the metal for the negative electric fields with a field strength below -0.1 V/Å. This is also reflected in the PDOS and MOPDOS which show a continuous shift of the orbital energies when applying an electric field. The plane-averaged induced charge density in response to the electric field confirms this behavior since additional charge rearrangements are visible at the interface, as well as a clear polarization in all three systems.

Since it is difficult to fully understand all rearrangements at the interface, for future research, it would be advantageous to extend the study to systems with charge donation into the metal for comparison. Furthermore, since the electric field induced charge transfer is planned to be realized experimentally, a comparison of simulated momentum maps with ARPES experiments can be made. However, it is important to note that, since the charge transfer at these considered electric fields is small, there may be no significant changes in the momentum maps other than an intensity increase (decrease) with amplified (reduced) charge transfer.

Bibliography

[1] S. R. Forrest and M. E. Thompson, "Introduction: Organic Electronics and Optoelectronics", en, Chemical Reviews **107**, 923–925 (2007).

[2] M. Fahlman, S. Fabiano, V. Gueskine, D. Simon, M. Berggren, and X. Crispin, "Interfaces in organic electronics", en, Nature Reviews Materials **4**, 627–650 (2019).

[3] O. T. Hofmann, E. Zojer, L. Hörmann, A. Jeindl, and R. J. Maurer, "First-principles calculations of hybrid inorganic–organic interfaces: from state-of-the-art to best practice", en, Physical Chemistry Chemical Physics **23**, 8132–8180 (2021).

[4] E. Zojer, T. C. Taucher, and O. T. Hofmann, "The Impact of Dipolar Layers on the Electronic Properties of Organic/Inorganic Hybrid Interfaces", en, Advanced Materials Interfaces **6**, 1900581 (2019).

[5] G. Kresse and J. Furthmüller, "Efficiency of ab-initio total energy calculations for metals and semiconductors using a plane-wave basis set", en, Computational Materials Science **6**, 15–50 (1996).

[6] G. Kresse and J. Furthmüller, "Efficient iterative schemes for *ab initio* total-energy calculations using a plane-wave basis set", en, Physical Review B **54**, 11169–11186 (1996).

[7] G. Kresse and D. Joubert, "From ultrasoft pseudopotentials to the projector augmented-wave method", en, Physical Review B **59**, 1758–1775 (1999).

[8] K. Kalyanasundaram, "Applications of functionalized transition metal complexes in photonic and optoelectronic devices", Coordination Chemistry Reviews **177**, 347–414 (1998).

[9] W. Wulfhekel, T. Miyamachi, S. Schmaus, T. Yamada, A. Takacs, A. Bagrets, F. Evers, T. Balashov, M. Gruber, V. Davesne, M. Bowen, and E. Beaurepaire, "Spintronics with single molecules", in 2012 12th IEEE International Conference on Nanotechnology (IEEE-NANO) (Aug. 2012), pp. 1–5.

[10] R. Xu, F. Xuan, and S. Y. Quek, "Spin-Dependent Tunneling Barriers in CoPc/VSe_2 from Many-Body Interactions", en, The Journal of Physical Chemistry Letters **11**, 9358–9363 (2020).

[11] A. V. Krukau, O. A. Vydrov, A. F. Izmaylov, and G. E. Scuseria, "Influence of the exchange screening parameter on the performance of screened hybrid functionals", en, The Journal of Chemical Physics **125**, 224106 (2006).

[12] J. P. Perdew, M. Ernzerhof, and K. Burke, "Rationale for mixing exact exchange with density functional approximations", en, The Journal of Chemical Physics **105**, 9982–9985 (1996).

[13] M. Ernzerhof and G. E. Scuseria, “Assessment of the Perdew–Burke–Ernzerhof exchange-correlation functional”, en, The Journal of Chemical Physics **110**, 5029–5036 (1999).

[14] C. Adamo and V. Barone, “Toward reliable density functional methods without adjustable parameters: The PBE0 model”, en, The Journal of Chemical Physics **110**, 6158–6170 (1999).

[15] V. I. Anisimov, J. Zaanen, and O. K. Andersen, “Band theory and Mott insulators: Hubbard U instead of Stoner I”, en, Physical Review B **44**, 943–954 (1991).

[16] S. L. Dudarev, G. A. Botton, S. Y. Savrasov, C. J. Humphreys, and A. P. Sutton, “Electron-energy-loss spectra and the structural stability of nickel oxide: An LSDA+U study”, en, Physical Review B **57**, 1505–1509 (1998).

[17] I. E. Brumboiu, S. Haldar, J. Lüder, O. Eriksson, H. C. Herper, B. Brena, and B. Sanyal, “Influence of Electron Correlation on the Electronic Structure and Magnetism of Transition-Metal Phthalocyanines”, en, Journal of Chemical Theory and Computation **12**, 1772–1785 (2016).

[18] M. Fujita, K. Wakabayashi, K. Nakada, and K. Kusakabe, “Peculiar Localized State at Zigzag Graphite Edge”, en, Journal of the Physical Society of Japan **65**, 1920–1923 (1996).

[19] T. Enoki and K. Takai, “The edge state of nanographene and the magnetism of the edge-state spins”, en, Solid State Communications **149**, 1144–1150 (2009).

[20] M. R. Ajayakumar, Y. Fu, J. Ma, F. Hennersdorf, H. Komber, J. J. Weigand, A. Alfonsov, A. A. Popov, R. Berger, J. Liu, K. Müllen, and X. Feng, “Toward Full Zigzag-Edged Nanographenes: *peri* -Tetracene and Its Corresponding Circumanthracene”, en, Journal of the American Chemical Society **140**, 6240–6244 (2018).

[21] J. Neugebauer and M. Scheffler, “Adsorbate-substrate and adsorbate-adsorbate interactions of Na and K adlayers on Al(111)”, en, Physical Review B **46**, 16067–16080 (1992).

[22] J. P. Perdew, K. Burke, and M. Ernzerhof, “Generalized Gradient Approximation Made Simple”, en, Physical Review Letters **77**, 3865–3868 (1996).

[23] S. Grimme, J. Antony, S. Ehrlich, and H. Krieg, “A consistent and accurate *ab initio* parametrization of density functional dispersion correction (DFT-D) for the 94 elements H-Pu”, en, The Journal of Chemical Physics **132**, 154104 (2010).

[24] D. Lüftner, S. Weiß, X. Yang, P. Hurdax, V. Feyer, A. Gottwald, G. Koller, S. Soubatch, P. Puschnig, M. G. Ramsey, and F. S. Tautz, “Understanding the photoemission distribution of strongly interacting two-dimensional overlayers”, en, Physical Review B **96**, 125402 (2017).

[25] J. Tersoff and D. R. Hamann, “Theory of the scanning tunneling microscope”, en, Physical Review B **31**, 805–813 (1985).

[26] G. Heimel, L. Romaner, E. Zojer, and J.-L. Brédas, “A theoretical view on self-assembled monolayers in organic electronic devices”, in , Vol. 6999, edited by P. L. Heremans, M. Muccini, and E. A. Meulenkamp (Apr. 2008), p. 699919.

[27] M. Born and W. Heisenberg, “Zur quantentheorie der Molekeln”, Original Scientific Papers Wissenschaftliche Originalarbeiten, 216–246 (1985).

[28] W. Kohn, “Nobel Lecture: Electronic structure of matter—wave functions and density functionals”, en, Reviews of Modern Physics **71**, 1253–1266 (1999).

[29] C. C. J. Roothaan, “New Developments in Molecular Orbital Theory”, en, Reviews of Modern Physics **23**, 69–89 (1951).

[30] P. Hohenberg and W. Kohn, “Inhomogeneous Electron Gas”, en, Physical Review **136**, B864–B871 (1964).

[31] M. Levy, “Electron densities in search of Hamiltonians”, en, Physical Review A **26**, 1200–1208 (1982).

[32] J. F. Janak, “Proof that $\frac{\partial E}{\partial n_i} = \epsilon$ in density-functional theory”, en, Physical Review B **18**, 7165–7168 (1978).

[33] W. Kohn and L. J. Sham, “Self-Consistent Equations Including Exchange and Correlation Effects”, en, Physical Review **140**, A1133–A1138 (1965).

[34] K. Terakura, T. Oguchi, A. R. Williams, and J. Kübler, “Band theory of insulating transition-metal monoxides: Band-structure calculations”, en, Physical Review B **30**, 4734–4747 (1984).

[35] G. A. Sawatzky and J. W. Allen, “Magnitude and Origin of the Band Gap in NiO”, en, Physical Review Letters **53**, 2339–2342 (1984).

[36] J. Heyd, G. E. Scuseria, and M. Ernzerhof, “Hybrid functionals based on a screened Coulomb potential”, en, The Journal of Chemical Physics **118**, 8207–8215 (2003).

[37] H. Hellmann, “A New Approximation Method in the Problem of Many Electrons”, en, The Journal of Chemical Physics **3**, 61–61 (1935).

[38] W. E. Pickett, “Pseudopotential methods in condensed matter applications”, en, Computer Physics Reports **9**, 115–197 (1989).

[39] N. Troullier and J. L. Martins, “Efficient pseudopotentials for plane-wave calculations”, en, Physical Review B **43**, 1993–2006 (1991).

[40] D. Vanderbilt, “Soft self-consistent pseudopotentials in a generalized eigenvalue formalism”, en, Physical Review B **41**, 7892–7895 (1990).

[41] P. E. Blöchl, “Projector augmented-wave method”, en, Physical Review B **50**, 17953–17979 (1994).

[42] P. E. Blöchl, C. J. Först, and J. Schimpl, “Projector augmented wave method:ab initio molecular dynamics with full wave functions”, en, Bulletin of Materials Science **26**, 33–41 (2003).

[43] L. Bengtsson, “Dipole correction for surface supercell calculations”, en, Physical Review B **59**, 12301–12304 (1999).

[44] Y. Saad, *Iterative methods for sparse linear systems*, eng, 2. ed., [Nachdr.] (SIAM, Society for Industrial and Applied Mathematics, Philadelphia, PA, 2007).

[45] D. M. Wood and A. Zunger, “A new method for diagonalising large matrices”, Journal of Physics A: Mathematical and General **18**, 1343–1359 (1985).

[46] E. Verwüster, E. Wruss, E. Zojer, and O. T. Hofmann, “Exploring the driving forces behind the structural assembly of biphenylthiolates on Au(111)”, en, The Journal of Chemical Physics **147**, 024706 (2017).

[47] S. Grimme, “Semiempirical GGA-type density functional constructed with a long-range dispersion correction”, en, Journal of Computational Chemistry **27**, 1787–1799 (2006).

[48] S. Grimme, “Accurate description of van der Waals complexes by density functional theory including empirical corrections”, en, Journal of Computational Chemistry **25**, 1463–1473 (2004).

[49] S. Grimme, S. Ehrlich, and L. Goerigk, “Effect of the damping function in dispersion corrected density functional theory”, en, Journal of Computational Chemistry **32**, 1456–1465 (2011).

[50] A. Tkatchenko and M. Scheffler, “Accurate Molecular Van Der Waals Interactions from Ground-State Electron Density and Free-Atom Reference Data”, en, Physical Review Letters **102**, 073005 (2009).

[51] T. Bučko, S. Lebègue, J. Hafner, and J. G. Ángyán, “Improved Density Dependent Correction for the Description of London Dispersion Forces”, en, Journal of Chemical Theory and Computation **9**, 4293–4299 (2013).

[52] T. Bučko, S. Lebègue, J. G. Ángyán, and J. Hafner, “Extending the applicability of the Tkatchenko-Scheffler dispersion correction via iterative Hirshfeld partitioning”, en, The Journal of Chemical Physics **141**, 034114 (2014).

[53] P. Bultinck, C. Van Alsenoy, P. W. Ayers, and R. Carbó-Dorca, “Critical analysis and extension of the Hirshfeld atoms in molecules”, en, The Journal of Chemical Physics **126**, 144111 (2007).

[54] T. Gould, S. Lebègue, J. G. Ángyán, and T. Bučko, “A Fractionally Ionic Approach to Polarizability and van der Waals Many-Body Dispersion Calculations”, en, Journal of Chemical Theory and Computation **12**, 5920–5930 (2016).

[55] M. Dion, H. Rydberg, E. Schröder, D. C. Langreth, and B. I. Lundqvist, “Van der Waals Density Functional for General Geometries”, en, Physical Review Letters **92**, 246401 (2004).

[56] J. Klimeš, D. R. Bowler, and A. Michaelides, “Van der Waals density functionals applied to solids”, en, Physical Review B **83**, 195131 (2011).

[57] R. Taube, “New aspects of the chemistry of transition metal phthalocyanines”, Pure and Applied Chemistry **38**, 427–438 (1974).

[58] N. Marom and L. Kronik, “Density functional theory of transition metal phthalocyanines, I: electronic structure of NiPc and CoPc—self-interaction effects”, en, Applied Physics A **95**, 159–163 (2009).

[59]M. G. Betti, P. Gargiani, C. Mariani, S. Turchini, N. Zema, S. Fortuna, A. Calzolari, and S. Fabris, "Formation of Hybrid Electronic States in FePc Chains Mediated by the Au(110) Surface", en, The Journal of Physical Chemistry C **116**, 8657–8663 (2012).

[60]Y. Wang, X. Li, and J. Yang, "Electronic and magnetic properties of CoPc and FePc molecules on graphene: the substrate, defect, and hydrogen adsorption effects", en, Physical Chemistry Chemical Physics **21**, 5424–5434 (2019).

[61]J. M. Gottfried, "Surface chemistry of porphyrins and phthalocyanines", en, Surface Science Reports **70**, 259–379 (2015).

[62]M.-S. Liao and S. Scheiner, "Electronic structure and bonding in metal phthalocyanines, Metal=Fe, Co, Ni, Cu, Zn, Mg", en, The Journal of Chemical Physics **114**, 9780–9791 (2001).

[63]P. Gargiani, G. Rossi, R. Biagi, V. Corradini, M. Pedio, S. Fortuna, A. Calzolari, S. Fabris, J. C. Cezar, N. B. Brookes, and M. G. Betti, "Spin and orbital configuration of metal phthalocyanine chains assembled on the Au(110) surface", en, Physical Review B **87**, 165407 (2013).

[64]J. Bartolomé, C. Monton, and I. K. Schuller, "Magnetism of Metal Phthalocyanines", in *Molecular Magnets*, edited by J. Bartolomé, F. Luis, and J. F. Fernández, Series Title: NanoScience and Technology (Springer Berlin Heidelberg, Berlin, Heidelberg, 2014), pp. 221–245.

[65]M. Methfessel and A. T. Paxton, "High-precision sampling for Brillouin-zone integration in metals", en, Physical Review B **40**, 3616–3621 (1989).

[66]S. Myradalyyev, T. Limpanuparb, X. Wang, and H. Hirao, "Comparative computational analysis of binding energies between several divalent first-row transition metals (Cr^{2+}, Mn^{2+}, Fe^{2+}, Co^{2+}, Ni^{2+}, and Cu^{2+}) and ligands (porphine, corrin, and TMC)", en, Polyhedron **52**, 96–101 (2013).

[67]A. D. Becke, "Density-functional thermochemistry. III. The role of exact exchange", en, The Journal of Chemical Physics **98**, 5648–5652 (1993).

[68]P. J. Stephens, F. J. Devlin, C. F. Chabalowski, and M. J. Frisch, "Ab Initio Calculation of Vibrational Absorption and Circular Dichroism Spectra Using Density Functional Force Fields", en, The Journal of Physical Chemistry **98**, 11623–11627 (1994).

[69]W. J. Hehre, R. Ditchfield, and J. A. Pople, "Self—Consistent Molecular Orbital Methods. XII. Further Extensions of Gaussian—Type Basis Sets for Use in Molecular Orbital Studies of Organic Molecules", en, The Journal of Chemical Physics **56**, 2257–2261 (1972).

[70]M. Klein, J. B. Bauer, N. Kainbacher, M. S. Wagner, K. Greulich, P. Haizmann, E. Giangrisostomi, R. Ovsyannikov, P. Puschnig, T. Chassé, H. F. Bettinger, and H. Peisert, "*Peri*-tetracene and 1,1'-bitetracene: Zipping up structurally defined graphene nanoribbons", [Manuscript in preparation].

[71]J. Krüger, N. Pavliček, J. M. Alonso, D. Pérez, E. Guitián, T. Lehmann, G. Cuniberti, A. Gourdon, G. Meyer, L. Gross, F. Moresco, and D. Peña, “Tetracene Formation by On-Surface Reduction”, en, ACS Nano **10**, 4538–4542 (2016).

[72]H. J. Monkhorst and J. D. Pack, “Special points for Brillouin-zone integrations”, en, Physical Review B **13**, 5188–5192 (1976).

[73]H. Ishii, K. Sugiyama, E. Ito, and K. Seki, “Energy Level Alignment and Interfacial Electronic Structures at Organic/Metal and Organic/Organic Interfaces”, en, Advanced Materials **11**, 605–625 (1999).

[74]P. S. Bagus, V. Staemmler, and C. Wöll, “Exchangelike Effects for Closed-Shell Adsorbates: Interface Dipole and Work Function”, en, Physical Review Letters **89**, 096104 (2002).

[75]S. Kubatkin, A. Danilov, M. Hjort, J. Cornil, J.-L. Brédas, N. Stuhr-Hansen, P. Hedegård, and T. Bjørnholm, “Single-electron transistor of a single organic molecule with access to several redox states”, en, Nature **425**, 698–701 (2003).

[76]J. M. Garcia-Lastra, C. Rostgaard, A. Rubio, and K. S. Thygesen, “Polarization-induced renormalization of molecular levels at metallic and semiconducting surfaces”, en, Physical Review B **80**, 245427 (2009).

[77]F. Aryasetiawan and O. Gunnarsson, “The $\boldsymbol{GW}$ method”, Reports on Progress in Physics **61**, 237–312 (1998).

[78]G. Onida, L. Reining, and A. Rubio, “Electronic excitations: density-functional versus many-body Green’s-function approaches”, en, Reviews of Modern Physics **74**, 601–659 (2002).

[79]O. T. Hofmann, “Structure-to-Property Relationships in Metal/Organic Interfaces”, PhD thesis (Graz University of Technology, Oct. 2010).

[80]G. Henkelman, A. Arnaldsson, and H. Jónsson, “A fast and robust algorithm for Bader decomposition of charge density”, en, Computational Materials Science **36**, 354–360 (2006).

[81]E. Sanville, S. D. Kenny, R. Smith, and G. Henkelman, “Improved grid-based algorithm for Bader charge allocation”, en, Journal of Computational Chemistry **28**, 899–908 (2007).

[82]W. Tang, E. Sanville, and G. Henkelman, “A grid-based Bader analysis algorithm without lattice bias”, Journal of Physics: Condensed Matter **21**, 084204 (2009).

[83]M. Yu and D. R. Trinkle, “Accurate and efficient algorithm for Bader charge integration”, en, The Journal of Chemical Physics **134**, 064111 (2011).

[84]T. Ules, D. Lüftner, E. M. Reinisch, G. Koller, P. Puschnig, and M. G. Ramsey, “Continuous or discrete: Tuning the energy level alignment of organic layers with alkali dopants”, en, Physical Review B **94**, 205405 (2016).

[85]E. M. Reinisch, T. Ules, P. Puschnig, S. Berkebile, M. Ostler, T. Seyller, M. G. Ramsey, and G. Koller, “Development and character of gap states on alkali doping of molecular films”, New Journal of Physics **16**, 023011 (2014).

[86] I. R. Solá, J. González-Vázquez, R. De Nalda, and L. Bañares, “Strong field laser control of photochemistry”, en, Physical Chemistry Chemical Physics **17**, 13183–13200 (2015).

[87] S. Berkebile, T. Ules, P. Puschnig, L. Romaner, G. Koller, A. J. Fleming, K. Emtsev, T. Seyller, C. Ambrosch-Draxl, F. P. Netzer, and M. G. Ramsey, “A momentum space view of the surface chemical bond”, en, Physical Chemistry Chemical Physics **13**, 3604 (2011).

[88] A. Puzder, M. Dion, and D. C. Langreth, “Binding energies in benzene dimers: Nonlocal density functional calculations”, en, The Journal of Chemical Physics **124**, 164105 (2006).

[89] K. Toyoda, Y. Nakano, I. Hamada, K. Lee, S. Yanagisawa, and Y. Morikawa, “First-principles study of benzene on noble metal surfaces: Adsorption states and vacuum level shifts”, en, Surface Science **603**, 2912–2922 (2009).

[90] V. G. Ruiz, W. Liu, E. Zojer, M. Scheffler, and A. Tkatchenko, “Density-Functional Theory with Screened van der Waals Interactions for the Modeling of Hybrid Inorganic-Organic Systems”, en, Physical Review Letters **108**, 146103 (2012).

[91] J. Lüder, B. Sanyal, O. Eriksson, C. Puglia, and B. Brena, “Comparison of van der Waals corrected and sparse-matter density functionals for the metal-free phthalocyanine/gold interface”, en, Physical Review B **89**, 045416 (2014).

[92] L. Hörmann, A. Jeindl, and O. T. Hofmann, “Reproducibility of potential energy surfaces of organic/metal interfaces on the example of PTCDA on Ag(111)”, en, The Journal of Chemical Physics **153**, 104701 (2020).

[93] O. Bauer, G. Mercurio, M. Willenbockel, W. Reckien, C. Heinrich Schmitz, B. Fiedler, S. Soubatch, T. Bredow, F. S. Tautz, and M. Sokolowski, “Role of functional groups in surface bonding of planar π-conjugated molecules”, en, Physical Review B **86**, 235431 (2012).

[94] C. Bürker, “Adsorption geometry of π-conjugated organic molecules on metal surfaces studied with the X-ray standing wave technique”, PhD thesis (Eberhard Karls University of Tübingen, 2014).

[95] L. Eschmann, J. Neuendorf, and M. Rohlfing, “Graphene and NTCDA adsorbed on Ag(111): Temperature-dependent binding distance and phonon coupling to the interface state”, en, Physical Review B **104**, 245403 (2021).

[96] M. Willenbockel, D. Lüftner, B. Stadtmüller, G. Koller, C. Kumpf, S. Soubatch, P. Puschnig, M. G. Ramsey, and F. S. Tautz, “The interplay between interface structure, energy level alignment and chemical bonding strength at organic–metal interfaces”, en, Physical Chemistry Chemical Physics **17**, 1530–1548 (2015).

[97] C. Seidel, C. Awater, X. Liu, R. Ellerbrake, and H. Fuchs, “A combined STM, LEED and molecular modelling study of PTCDA grown on Ag(110)”, en, Surface Science **371**, 123–130 (1997).

[98]K. Glöckler, C. Seidel, A. Soukopp, M. Sokolowski, E. Umbach, M. Böhringer, R. Berndt, and W.-D. Schneider, “Highly ordered structures and submolecular scanning tunnelling microscopy contrast of PTCDA and DM-PBDCI monolayers on Ag(111) and Ag(110)”, en, Surface Science **405**, 1–20 (1998).

[99]M. Böhringer, W.-D. Schneider, K. Glöckler, E. Umbach, and R. Berndt, “Adsorption site determination of PTCDA on Ag(110) by manipulation of adatoms”, en, Surface Science **419**, L95–L99 (1998).

[100]P. Hyldgaard, Y. Jiao, and V. Shukla, “Screening nature of the van der Waals density functional method: a review and analysis of the many-body physics foundation”, Journal of Physics: Condensed Matter **32**, 393001 (2020).